NMR INVESTIGATIONS OF BLOOD COAGULATION: CONFORMATIONAL CHANGES OF MEMBRANE BILAYERS AND PROTEINS IN BLOOD COAGULATION

BY

JOHN MICHEAL BOETTCHER

DISSERTATION

Submitted in partial fulfillment of the requirements
for the degree of Doctor of Philosophy in Chemistry
in the Graduate College of the
University of Illinois at Urbana-Champaign, 2010

Urbana, Illinois

Doctoral Committee:

Associate Professor Chad M. Rienstra, Chair
Assistant Professor Julia M. George
Professor Martin Gruebele
Professor James H. Morrissey

ABSTRACT

A multitude of biological processes involve membranes and their associated membrane proteins. The interactions of these biological molecules lead to perturbations in their structure and dynamics. Understanding the variations in the constitution of these molecules as the result of functional interactions will provide insights into various biological processes. In this work, we employ solution and solid-state NMR to observe changes in dynamics and conformation of both membranes and membrane associated proteins upon interaction with other biological molecules. Initial studies focus on the interaction of neurological proteins alpha-synuclein and endosulfine-alpha. Using chemical shift perturbation mapping we detail interactions of membrane bound alpha-synuclein with cAMP-regulated phosphoproteins, ARPP-19 and endosulfine-alpha. Additionally, we report that endosulfine-alpha is an intrinsically unstructured protein that undergoes a conformational change upon binding to membranes and detail the effects of phosphorylation on these structures. Furthermore, using a combination of solution and solid-state NMR, we investigate important interactions involved in blood coagulation. Structural and dynamics data of Ca^{2+}-induced clusters of phosphatidylserine in membranes, important in blood clotting, is investigated using isotopically ^{13}C, ^{15}N-labeled phosphatidylserine in lipid bilayers. Finally, backbone resonances of the soluble, extracellular domain of tissue factor (absent the membrane binding transmembrane helix) are assigned in solution and nanocrystalline samples by solution and solid-state NMR respectively. The chemical shifts are then used to investigate changes in the extracellular domain of tissue factor when bound to the membrane by its native transmembrane helix.

This thesis is dedicated to Erika for all the love and support through the years

ACKNOWLEDGEMENTS

Throughout my thesis I have received support from friends, family and co-workers. I could not have completed this process if not for their unyielding encouragement. This acknowledgement section can never fully convey my full gratitude. Thank you all!

First I would like to express my appreciation for my advisor, Dr. Chad Rienstra. He is a wonderful teacher and his knowledge of science, specifically his extensive knowledge of biological NMR, will benefit me through the rest of my career. His consistent expectation for excellence in the science we produce has pushed me to become a far better scientist than I would have been in his absence.

I have shared my time in the lab with many wonderful people. Their support, from scientific collaborations to sharing stories of, "… one time in Buffalo…", has been appreciated and will never be forgotten. Thanks to those who were here and are now gone, Trent, Ben, Heather, Kathy, Ying and Alex. Especially, thanks to Dr. Donghua Zhou for making available to all of us his expertise (… so says the The Book of Donghua …). For all my current lab mates, Lindsey, Andy, Luisel, Gemma, Mike, Mary, Kristin, Ming, Anna and Deb, I am indebted to you for all the help and will treasure the time we have had together. I also would like to thank Ben LaHood, my undergraduate (gel-running) "grunt", without whom, the tissue factor project would have faltered. I hope these friendships I have formed here will last the rest of my life.

I have benefited from wonderful collaborations with exceptionally talented scientists. Dr. Julia George taught me about alpha-synuclein and dopaminergic neurons. Her expertise was enormously helpful and she was a joy to work with. Dr. James (Jim) Morrissey is a class act and he is the driving force behind the multi collaborative blood coagulation project. His extensive knowledge of the chemistry of blood clotting has been invaluable to my work. Jim's post-doc,

Dr. Rebecca Davis-Harrison has been my “partner in crime” in the blood coagulation project. From titrating Ca^{2+} into micelles in the NOYES NMR lab to taking the spectra of isotopically labeled PS in Nanodiscs, I appreciate her collaboration in developing the concept of labeled lipid samples into a reality.

Family support was invaluable to my success. My wife’s Aunt Theresa drove me to my first visit on campus over five years ago and her and her sisters made the transition to Illinois easier. In addition, the extended family in Springfield has made many weekends and holidays a relaxing retreat from the long hours in the lab. Thank you for taking me in as part of the family!

To Grandma Kennedy, you are a wonderful, loving person. Your extensive support throughout this process has been monumental. You were there for me when I first came here and was alone while Erika and the kids were still in Buffalo. You opened your home and your heart for which I will be eternally grateful. I love you Grandma!

My loving parent-in-laws have been overly generous with everything they have. Fran, I want to thank you for never holding back and treating me like one of your own children. My father-in-law, Bob, is the kind of person I would like to be. I admire and hope to one day achieve the success in life Bob and Fran have. Thank you for everything.

Without my parents none of this would be. My father is a caring loving man who taught me about focus and that has served me well. My mother taught me a love for math and science. Sadly, she has passed away prior to the completion of my thesis. Her spirit will forever be a part of all I do. She is sorely missed (love you Mom).

My three children have been a driving force, compelling my completion of this dissertation. Gabriella, Kennedy and Claire, I hope to be able to give to you all that has been given to me, and more.

Finally, to my wife, Erika, I owe everything. Your love, care and support can never be repaid. From the first day we met, you made me want to be a better man. You started this journey with me 5+ years ago. It has not been easy. As much as my parents shaped the man I am, you will forever be a part of the man I will become. All that I am and all that I do is for you. All my love…

TABLE OF CONTENTS

LIST OF FIGURES

LIST OF TABLES

CHAPTER 1

Introduction

1.1 Preface

Membranes and their associated proteins frequently function in an interdependent manor where conformational changes in proteins and/or the membrane bilayer instigate critical biological processes (*1*). Studies of these conformational changes are crucial for elucidating the underlying physical bases behind these important biological processes. Nuclear magnetic resonance spectroscopy (NMR) is a powerful tool used in the investigation of both chemical structures and dynamic chemical interactions, the essential components of biological systems and processes. Furthermore, NMR is uniquely suited to interrogate molecular systems in either membranous (solid-state NMR) or aqueous (solution NMR) environments, and to track protein conformational changes induced by its environment or cofactors without solving additional structures. This gives NMR a distinct advantage over X-ray crystallography, which requires single crystals for each protein conformation; the difficulties of crystallizing membrane proteins have been reviewed extensively due to the importance of numerous membrane proteins as drug targets (*2*).

This dissertation focuses on the application of NMR spectroscopy to discern the conformations of membranes and associated proteins in several systems. In chapters 3, 4 and 5, two peripheral membrane proteins involved in neurobiological processes, alpha-synuclein and endosulfine-alpha, are investigated. Chapters 6 through 8 focus on membrane-protein interactions involved in blood coagulation with emphasis on the protein-membrane interactions

of tissue factor (TF) and the structure and dynamics of Ca^{2+}-induced phosphatidylserine clusters in membranes.

1.2 Conformational Changes of Membranes-Protein Interactions

Eukaryotic cells separate the interior aqueous cytosol from the external environment by a thin double layer of lipids embedded with proteins called the plasma membrane (*1*). Inside the cell membranes segregate various organelles from the cytosol. Though, there are differences in the content and specific function of each membrane, they share many common characteristics (*1*). Each membrane is a bilayer of lipids held together by noncovalent interactions where the polar headgroup of the lipid interact with the aqueous environment while the hydrophobic tails of the lipids interact with each other forming the hydrophobic interior of the bilayer. The membrane bilayer is fluid and dynamic, yet it maintains a barrier to the passage of most water-soluble molecules. Associated with the membrane are proteins that serve various biological functions, from cell signaling to transport/channeling of ions, proteins and other small molecules across the membrane. Though membranes have been classically thought of as a chemically inert hydrophobic barrier and a platform for protein-protein interactions (*3*); a more modern understanding has evolved: membranes and proteins work concertedly to carry out biological processes (*1, 4*).

Two main classes of proteins are associated with membranes, integral membrane proteins and peripheral membrane proteins. Integral membrane proteins have a section of the protein inserted into the interior hydrophobic region of the lipid bilayer. Peripheral membrane proteins are associated with the surface of the membrane through noncovalent interactions or, in other cases, tethered to hydrophobic molecules that insert into the bilayer, anchoring the protein to the surface of the membrane. Interactions of these proteins with substrates, cofactors and the

membrane bilayer often cause slight changes in the protein structure that are essential for function (*1*). Understanding these conformational changes will be paramount to understanding the function of these proteins (*1*).

The membrane also plays a critical role in the biological function of the cell (*1, 4*), and; like proteins, the membrane function is dependent on the composition, dynamics and structure (*1, 4*). Cells maintain tight control on the amount and type of lipids present in the bilayer (*5, 6*). More specifically, scramblases and flipases, membrane proteins that facilitate lipid transport between bilayer leaflets, segregate certain lipid types to either the inner or outer leaflet (*5, 6*). This allows for temporal and spatial control over specific biological processes. For instance, many signaling mechanisms are triggered upon the appearance of phosphatidylserine on the external leaflet of the plasma membrane, a signal of cell injury that prompts apoptosis (*6*).

Membrane dynamics are often best understood as the phase behavior of the lamellar lipid bilayer, though, non-bilayer lipid phases certainly are important for various biological functions including, fusion, fission and pore formation (*7*). Lipid phases may be defined by the order parameter and lipid diffusion. The order parameter (S) describes the average orientation of the lipids in the bilayer as compared to a perpendicular line to the membrane surface. The parameter S can have values from 0 (no order) to 1 (rigid order). Lipid diffusion refers to the propensity of lipids to disperse laterally along the bilayer. The two parameters are not completely independent of one another. Molecules in a highly ordered state are most likely restricted in their motion and conversely molecules with rapid diffusion are anticipated to have little order, though both parameters are needed for a complete explanation of the system.

Lipid phases depend on several factors, including, temperature, lipid composition and protein interactions (*1, 4, 7*) and three lamellar lipid bilayer phases will be discussed here, the liquid

crystalline phase, solid gel phase and the liquid ordered phase. The liquid crystalline phase is characterized by a low overall order parameter and rapid lipid diffusion in the bilayer (*7*). This phase is often seen in bilayers at higher temperatures that contain lipids with unsaturated hydrocarbon chains (*7*). The opposite of the liquid crystalline phase is the solid gel phase, which maintains a high order parameter and slow lipid diffusion in the bilayer and is common in membranes consisting of lipids with saturated hydrocarbon chains (*7*). Finally, membranes can take on a liquid ordered phase (*7*), which is characterized with a high order parameter with rapid lipid diffusion. This is most easily seen in lipid rafts and clustering events where the lipids are associated with interactions with protein and/or ions in solution. This causes the specific lipids to have a high order in the headgroups but the acyl chains remain dynamic. Interestingly, several different phases can be observed in a continuous bilayer allowing for various biological processes to take place across the entire membrane (*1, 4, 7*). As with their protein counterparts, investigations of the structure and dynamics of membranes will give insights into their biological processes.

1.3 NMR as a Tool in Investigating Conformational Changes

1.3.1 Overview

NMR has evolved into a powerful method used to investigate the structural and dynamic properties of biological molecules. The first spectrum of a protein was recorded in 1957 (*8*) but it took 28 years to develop the techniques needed to solve the first NMR structure of the 57 residue bull seminal trypsin inhibitor (*9*). NMR is now routinely used to solve structures of much larger systems, including membrane proteins and protein complexes. In addition to solving full structures, NMR data can be used in a number of ways to collect atomically resolved information on the structure and dynamics of biological molecules.

NMR can provide numerous insights into the structure and dynamics of proteins and other biological molecules without the calculation of a full structure by using chemical shifts, relaxation data, dipolar and scalar couplings. These observables can be obtained in a variety of spectra and can result in a plethora of information on torsion angles, hydrogen bonding, inter and intra molecular distances. This dissertation uses both solution NMR and magic angle spinning (MAS) solid-state NMR (SSNMR) in the investigation of several biological systems. Conformation and dynamic changes in these systems due to various interactions will be explored by analyzing chemical shifts, dipolar couplings and relaxation properties.

1.3.2 Chemical Shifts

The resonance frequency of a nuclear spin is dependent upon its electronic surroundings, also referred to as the chemical environment of the atom. Specifically this refers to the electron density around the nucleus that "shields" it from the applied magnetic field. A mathematical expression of this is:

$$\omega = -\gamma(1-\sigma)B_o. \qquad (1)$$

Where, B_o is the strength of the applied magnetic field, γ is the gyromagnetic ratio of the atom, ω is observed frequency and σ is the shielding constant (*10*). The chemical environment is denoted by the value of σ. Atoms that are in different chemical environments will display different chemical shifts in the NMR spectra. Atoms lacking significant electron density (low shielding) will have high chemical shift values and atoms with a high degree of electron density will have low chemical shift values. The chemical environment of a given atom is effected by several different factors such as, the ionic strength of the solution, covalent bonds and on structural arrangement (torsional angles of bonds).

Chemical shifts of amino acids in proteins contain a surplus of information about backbone and side-chain dihedral angles, hydrogen bonding, orientation of aromatic rings, ionization states, oxidation states and salt bridges (*11*). The chemical shift of individual spin system can be used to identify the amino acid type and, in concert with multidimensional correlation spectra, can be used to assign the chemical shifts to a specific amino acid within the protein sequence (*10*). After the chemical shifts have been indentified to match a particular amino acid in the protein sequence then those values can be interpreted and yield site-specific conformational and chemically relevant information.

One such application is using the site-specific chemical shifts assignments of the protein to interpret the secondary structural elements (*12-14*). As stated previously, the chemical shifts are highly dependent on structure. The dihedral angles of the backbone atoms (Hα, H^N, N, Cα, Cβ, CO) determine the secondary structure in proteins. Chemical shifts of the backbone atoms are compared to the expected random coil chemical shift (chemical shift of the atom when the amino acid is in a dynamic unstructured state). Deviations from the random coil chemical shift are indicative of the secondary structure (*12-14*). Wishart and Sykes developed a tool known as the Chemical Shift index (*14*) that scores the chemical shifts based on their difference from the random coil value. Then, the output predicts the secondary structure as α-helical, β-strand or random coil. More recently an empirical program was developed to supply torsion angle values based on the chemical shift data; the most updated version is known as TALOS+ (*15*). Output from TALOS+ is based on a comparison of the chemical shifts with empirical data on proteins with known structures and chemical shifts (*15*). The values produced by TALOS+ are often used in structure calculations. Chemical shifts are therefore, a powerful tool in determining the structure of proteins.

Additionally, perturbations in chemical shifts can be use to investigate changes in the protein secondary structure upon interactions with other molecules. These interactions will lead to a change in the chemical environment, either through formation of new interactions (i.e. covalent, hydrogen bonds, salt bridges etc.), through conformational changes or both. Chemical shift perturbation mapping is used in solution NMR to map the interface of protein interactions (*16*). Basically, an unlabeled binding partner (either a small molecule, another protein, membranes etc.) is titrated into an isotopically labeled (at least ^{15}N labeling) protein and ^{1}H-^{15}N HSQC spectra are acquired for each titration step. The chemical shifts of the amides are monitored for changes from the ^{1}H-^{15}N HSQC spectra of the protein in the absence of the binding partner. If any changes in an amide resonance are noted, they are "mapped" as the concentration of the binding partner increases (*16*). These changes can then be attributed to specific residues in the protein sequence. This reveals, with atomic resolution, the areas of the protein involved in the interaction. A similar approach can be used with SSNMR as well. By comparing unbound and bound spectra, changes in the chemical shifts can be noted and an interface of the interaction can be mapped onto the protein structure and/or sequence.

1.3.3 Dipolar Couplings

Dipolar couplings arise when two dipoles are fixed in space relative to one another and to the relative magnetic field (*10*). In solution NMR dipolar interactions are normally not taken into consideration (except in special cases, such as Residual Dipolar Coupling measurements) because in most cases the tumbling of the molecule averages the dipolar couplings to zero. In static SSNMR the dipolar couplings are not averaged to zero and the magnitude of the coupling (D_{IS}) is dependent on orientation of the dipole vectors relative to the magnetic field (θ) and to the distance between the two spins (r_{IS}) (*10*),

$$D_{IS} = \frac{\hbar \gamma_I \gamma_S}{4\pi r_{IS}^3}[1 - 3\cos^2\theta]. \qquad (2)$$

Where γ_I is the gyromagnetic ratio of the I spin and γ_S, the gyromagnetic spin of the S spin. In MAS SSNMR the dipolar couplings are averaged to zero by spinning rapidly at the magic angle (54.7°), mimicking the tumbling in solution and making $[1\text{-}3\cos^2\theta] \approx 0$. The dipolar couplings can be "recoupled" in SSNMR through a series of designed pulse sequences (*17-19*). Since the dipolar interactions are proportional to $1/r_{IS}^3$, cross peaks in SSNMR spectra contain inherent distance information. This is taken advantage of and used to determine inter and intra molecular distances. Several specific pulse sequences that take advantage of homonuclear (DARR (*17, 18*)) and heteronuclear (TEDOR (*19*)) dipolar interactions and are used later on in the dissertation.

1.3.4 Dynamics

Biological molecules can undergo large fluctuations due to collision with solvent molecules, hinge-bending motions between secondary or tertiary structural elements and other relevant processes. The dynamics within a given biological molecule are linked to its interactions with the environment and other molecules. These molecular motions can cover a wide range of timescales. NMR has a unique capability to investigate a range of dynamic processes from the picosecond to the millisecond time scale (*10*) and therefore is perfect for investigating these important dynamical processes.

Dynamic measurements in NMR investigate the relaxation of the magnetization for a given atom. Two main relaxation rates focused on in the following NMR experiments are the longitudinal-relaxation and the transverse-relaxation (*10*). Longitudinal-relaxation, sometimes referred to as spin-lattice relaxation, (T_1) is described as the time it takes to return to the ground state after excitation (*10*). Transverse-relaxation, sometimes referred to as spin-spin relaxation, (T_2) is described as the time required for loss of the magnetization in the transverse dimension

(*10*). T_1 is dominated by interactions with the environment, while T_2 is dominated by interactions with neighboring atoms. Simple experiments can be used to determine T_1 and T_2 where the intensity of the signal is measured as a function of the relaxation delay (*10*). Measuring these relaxation parameters gives insight into how the molecule interacts with itself and within the environment. Changes to the dynamics upon interactions with other molecules are another way to probe the conformational changes and give atomically resolved insight into the system.

1.4 Systems Studied

1.4.1 Alpha-synuclein and Endosulfine-alpha

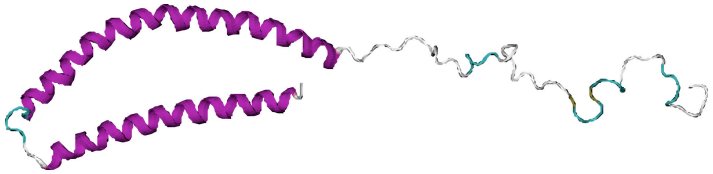

Figure 1.1 Structure of alpha-synuclein bound to micelles.

The structure of AS was solved by solution NMR was solved bound to micelles made of sodium dodecyl sulfate (PDB 1XQ8) (*20*).

Alpha-synuclein (AS) is an intrinsically unstructured protein in aqueous solution that is most notably associated with inherited and sporadic Parkinson's disease as the major fibril protein component of Lewy bodies (*21*). Lewy bodies are also seen in other neurological disorders including Alzheimer's disease, Down's syndrome and multiple system atrophy (*22*). In addition to identification of AS in Lewy bodies, studies showed AS as a putative synaptic vesicle protein (*23*) and as a gene regulated in zebra finch during the learning of songs (*24*) but the normal function of AS is not yet well understood.

The N-terminus of AS undergoes a conformational change in the presence of acidic phospholipid vesicles to a predominantly helical structure mediating membrane binding (*20, 25-27*) (Figure 1.1). The structure is maintained through interactions with lysine side-chains and

negatively charged headgroups of the lipids (*20*). This allows the remaining hydrophilic residues to face outward towards the cytosol. Residues exposed to the cytosol are highly conserved (*24*), suggesting the membrane association of AS plays an important biological functional. Identifying binding partners with membrane bound AS would help to understand the biological function of synuclein outside the formation of the β-sheet-rich fibrils found in various neurological diseases. Chapter 3 looks into neurological proteins that interact specifically with membrane bound AS and NMR conformational investigations focus on a family of cAMP-regulated phosphoproteins, ARPP-19, ARPP-16 and endosulfine-alpha.

Endosulfine-alpha (ENSA) was originally indentified as a protein involved in regulation of insulin secretion. Purified as an endogenous regulator for the ATP-sensitive potassium (K-ATP) channel (*28*), ENSA competes with the sulfonylurea glibenclamide for the sulfonylurea receptor (SUR) subunits, a binding site in the β cell membrane on K-ATP channels (*29*). ENSA was shown to inhibit potassium conductance in reconstituted K-ATP channels when applied to the intracellular side of the membrane (*30*). K-ATP channels are metabolic sensors for various cell types and play a central role in regulating insulin secretion (*31*). Inhibition of K^+ currents in K-ATP channels causes membrane depolarization and activation of voltage-gated Ca^{2+} channels, triggering insulin release. These same channels mediate glucose-stimulated insulin secretion, as they are inhibited and activated by metabolically produced ATP and MgADP. On that basis it was proposed that ENSA might be a natural regulator of insulin secretion and functional studies in Drosophila are consistent with such a role (*32*).

ENSA may also play a role in neurological regulatory processes. In brain tissue, K-ATP channel closure is associated with neurotransmitter release (*33*) and has been implicated in the differential vulnerability of midbrain dopamine neurons to neurodegeneration in Parkinson's

disease (*34*) leading to suggestions that sulfonylurea be considered as a candidate therapy for PD (*35*). Decreased expression of ENSA in the frontal cortex and cerebellum of Alzheimer's patients (*36*) and in Down's syndrome patients with Alzheimer's disease pathology (*37*) indicates that ENSA's expression varies significantly in several functional contexts. Other functional studies show ENSA mRNA is down regulated in rat hippocampus with long-term memory consolidation, but up-regulated with swimming-related stress (*38*). ENSA's aforementioned interaction with AS and, interactions with the membranes could play a key role in understanding its function in brain biochemistry.

The NMR investigations presented in chapter 4 provide the first structural information for ENSA. Intrinsically unstructured in aqueous solution, ENSA forms a four helical sections upon interaction with membranes that contain negatively charged headgroups. Phosphorylation is a common mechanism for regulation of protein interactions, and it is known that protein kinase A phosphorylates S109 of ENSA (*39*). The role of the phosphorylation on the membrane-bound structure of ENSA using the S109E mutant is evaluated in chapter 5 As well interactions between AS and ENSA on the membrane surface.

1.4.2 Blood Coagulation: Tissue Factor

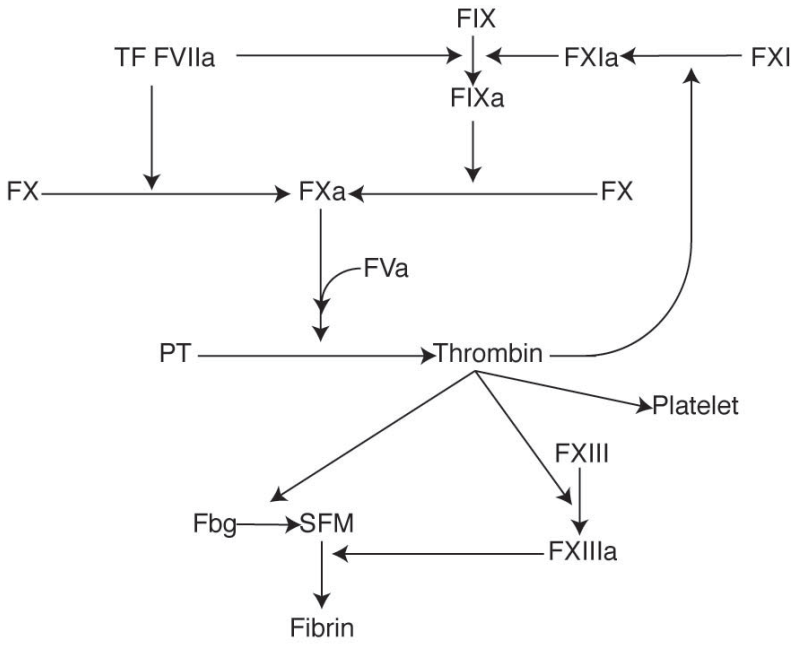

Figure 1.2 Blood-clotting cascade.

The extrinsic pathway to blood clotting initiates with the formation of the TF:FVIIa complex. TF:FVIIa activates FX and FIX and FIXa can also activate FX. FXa binds with activated FV forming the prothrombinase complex. From there thrombin is generated and the cascade continues to form a fibrin clot.

Thrombotic diseases are a major cause of disability and death in the United States and worldwide. Improved prevention, diagnosis, and treatment have been made possible due to insights into the biochemical mechanisms of blood coagulation. More research is needed in this area to help further the medical knowledge and lower the mortality and disability rates.

Almost every step in the blood-clotting cascade (Figure 1.2) involves the assembly of a serine protease with its cognate accessory protein on a suitable membrane surface. Clotting is initiated when activated plasma factor VII (FVIIa) binds to the integral membrane protein, tissue factor (TF), forming an enzymatic complex on the membrane surface (*40*). The TF:FVIIa complex binds and activates its substrates, both factor X (FX) and factor IX (FIX). Activated FIX can in turn, also produce activated FX (FXa). Then, FXa forms the prothrombinase complex

on the membrane surface with activated factor V. This in turn converts prothrombin to thrombin, which propagates the coagulation cycle and ultimately ends in the formation of a fibrin clot.

Composed of two fibronectin type III domains (extracellular domain), a cytoplasmic domain and a membrane spanning helix, (*41*) TF, the integral membrane protein involved in initiation of blood coagulation, is found on the surface of a variety of cells outside the vasculature (*42*). Factor VII (FVII) is a plasma serine protease and is the ligand for TF. A little less than 1% of FVII circulates in its active form (FVIIa) with the majority circulating in the zymogen form (*43*). FVII and FVIIa bind to TF with similar affinities (*44*) and once bound to TF, FVII is rapidly converted to FVIIa. The resulting enzymatic complex contains an essential regulatory subunit, TF and the catalytic subunit, FVIIa. It is well understood that TF induces conformational changes in the FVIIa active site, which dramatically increases activity (*45-47*). How TF dramatically enhances the enzymatic activity of FVIIa is not completely understood (*48*), although; membrane-anchoring of TF is absolutely required for full procoagulant activity (*49*).

Allosteric activation of FVIIa upon binding to TF can be broken down into three components, proper positioning of the protease domain with respect to substrates, formation of the substrate binding site and induced conformational changes in FVIIa active site (*50*). Crystal structures solved for the soluble extracellular domain of TF (sTF) (*51-53*) and of sTF in complex with FVIIa (*54, 55*) (Figure 1.3) along with several other studies (*56-60*) have given insights into these interactions. Binding to TF positions the protease domain ~80 Å from the surface of the membrane (*56, 57*) allowing for the activation of its substrates. Residues from both TF and FVIIa form the proposed substrate-binding site. Several studies have located key residues in TF involved in the substrate-binding site, specifically K165 and K166 (*58, 61-63*) (Figure 1.3). The most intriguing component to the allosteric activation is the conformational changes in FVIIa's

active site by distant contacts of TF with the heavy chain of FVIIa (contains the active site). Several studies (reviewed here: (*50*)) investigate this interaction yet questions still remain.

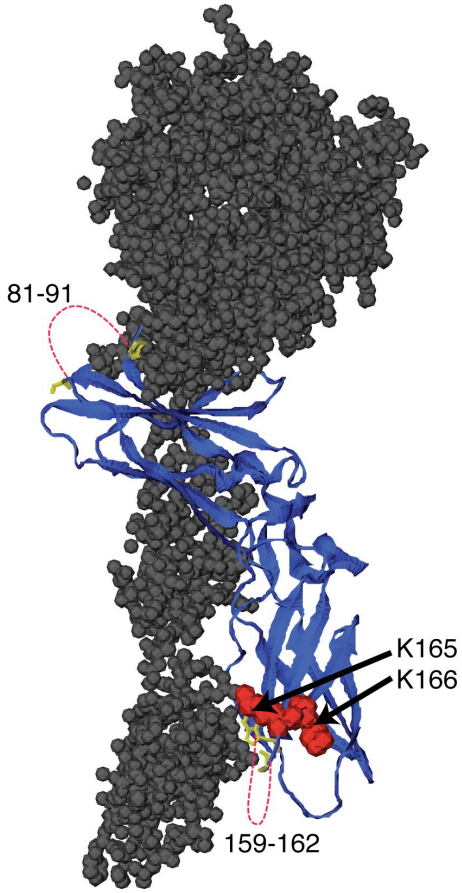

Figure 1.3 Crystal structure of sTF:FVIIa complex.

The sTF:FVIIa complex is shown (1DAN (*54*)) with FVIIa (gray, space-filling) behind sTF (blue, cartoon). Drawn in red, space-filling model on sTF are K165 and K166, residues involved in the binding of FX and FIX. The red dotted lines indicate residues that are missing in the crystal data.

Structural and atomically resolved dynamic information is not currently available for key residues in TF involved in the allosteric activation of FVIIa. TF Residue E91 is important for binding to FVIIa and for converting FIX to FIXa (*64*) and recent studies report dynamic changes in a loop containing E91, residues 79 to 92, upon binding to FVIIa (*65*). Though this dynamic data is important, it is low resolution and these interactions are missing in the crystal structures

of the sTF:FVIIa complex (*54, 55*) due to either lack of electron density or residues enzymatically removed prior to crystallization (Figure 1.3).

In addition, the substrate-binding site of the TF:FVIIa complex is located near the membrane surface and current complex structures lack any membrane interactions. Moreover, residues that are likely to interact with the membrane surface and effect the conformation of the substrate-binding site are missing in the sTF:FVIIa complex. Figure 1.4 demonstrates this and shows K166, known to be crucial in the binding of substrate (*58*), in different conformations in two sTF:FVIIa complex structures (*54, 55*). Chapters 8 and 9 focus on the assignment of chemical shifts of sTF and membrane bound TF (membTF) using both solution and solid-state NMR. Preliminary data on membrane bound TF reports on interactions between the membrane surface and several residues in the extracellular domain of TF.

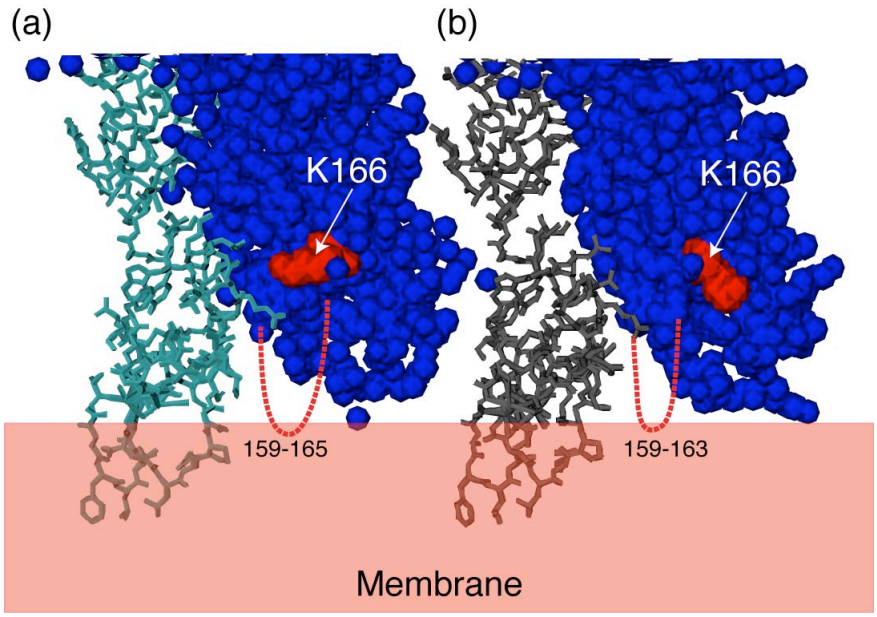

Figure 1.4 Substrate binding site of sTF:FVIIa complex.

The substrate binding domain of the sTF:FVIIa complex is shown for crystal structure (a) 2A2Q (*55*) and (b) 1DAN (*54*). The light chain of FVIIa (bonds) is shown and is behind the sTF molecule (space filling). The highly conserved K166 residue, that is important for binding substrate, is highlighted in red on sTF. The two crystal structures show two very different conformations. The dotted red lines indicated residues missing in the crystal structures. The proposed location of the membrane is shown (red box).

1.4.3 Blood Coagulation: Ca^{2+} induced clustering of Phosphatidylserine

There are many side effects and setbacks to using the available oral anticoagulant drugs (warfarin/coumadin) (*66*). In addition to their effect on proteins involved with blood clotting, coumadins also affect proteins involved in bone metabolism (*67, 68*). Other concerns include the narrow therapeutic range of Coumadin and Coumadin-like compounds and their unfortunate interactions with other drugs and the patient's diet (*66*). A better drug designed with higher precision and specificity to blood coagulation would benefit patients with thrombotic diseases.

Coumadins effect coagulation by preventing the proper formation of the membrane-binding domain of important blood clotting proteins. Several blood coagulation proteins (FVII, FIX, FX, prothrombin) share a common membrane-binding domain that is rich in γ-carboxylated glutamates (known as GLA domains). Coumadins are vitamin K antagonists and thus interfere with the cyclic interconversion of vitamin K and vitamin K epoxide (*66*). This cycling of vitamin K is essential for the γ-carboxylation of the glutamates in the GLA domain of coagulation factors (as well as several other GLA containing proteins involved in bone metabolism (*67, 68*)). Preventing these blood-clotting proteins from binding to membranes by hindering the production of functional GLA domains reduces their enzymatic activities many thousand-fold (*69, 70*). For example, FIX and FX are poorly activated by free FVIIa and experience a factor of 10^6 increase in activation when FVIIa is bound to TF in an appropriate phospholipid bilayer (*71-73*). The binding of the GLA domain to membrane surfaces is dependent on the presence of Ca^{2+} and anionic phospholipids, of which phosphatidylserine (PS) is preferred.

We hypothesize that, in addition to the GLA domains of the blood coagulation proteins, specific conformational changes in the membrane bilayer is also required for effective blood coagulation. Specifically, Ca^{2+}-induced PS clustering in membrane bilayers is a major factor

involved in blood clotting. Calcium induces the formation of PS clusters in membranes (*74*). The clustering of PS is thought to act as target regions that enhance blood coagulation as well as other biological activities such as, Ca^{2+}-triggered vesicle fusion (*75*) and protein kinase C signaling (*76*). Previous NMR studies have shown that Ca^{2+}-PS interactions in mixed bilayers produces two distinct conformations in PS headgroups (*77, 78*), Additionally, bulk membrane dynamic studies of Ca^{2+}-induced PS clusters show a broad and slightly elevated liquid crystal to solid gel phase transition (*79-81*). Although the formation of the Ca^{2+}-induced PS clusters generates changes in the structure and dynamics for both the entire membrane and individual PS molecules; most of the dynamics data focuses on bulk changes in the membrane bilayer and atomically resolved structures of PS headgroups exist only for individual PS molecules in dodecylphosphocholine micelles in the absence of Ca^{2+} (*82*). A more detailed molecular picture of the structure and dynamics of the individual PS molecules bound to calcium, as well as an atomic resolution structure of the Ca^{2+}-induced PS-cluster are needed to elucidate key blood coagulation processes. Chapter 6 focuses on investigating, with atomic specificity, PS conformations and the dynamic properties of Ca^{2+}-induced PS clusters.

1.5 Conclusion

Both membranes and their associated proteins play a critical role in biological processes and their functions depend on their structural and dynamic properties. As these biological molecules carry out their function by interacting with various other molecules, they undergo changes in dynamics and conformation. Studying these changes will help to better understand important biological processes, allowing for new insights into their role in physiology.

Using NMR throughout my investigations, I report on the conformational and dynamic changes of several important biological systems. The normal function of AS most certainly

involves the helical membrane bound form. In this thesis (Chapter 3) I describe interactions of several neurological proteins with membrane bound AS. This includes revealing atomic resolution changes on the structure of AS as it interacts with two cAMP-regulated phosphoproteins (ARPP-19 and ENSA). Chapter 4 shows for the first time, that ENSA is an intrinsically unstructured protein in aqueous solution that undergoes a conformational change upon binding to membranes. The effect phosphorylation of S109 has on ENSA in both membrane binding and interactions with AS are identified in chapter 6. Structural and conformational changes for both membranes and proteins involved in blood coagulation are investigated in chapters 6-8. Atomic resolved dynamics and structural information is detailed for Ca^{2+}-induced PS clustering important in blood coagulation (chapter 6). The last chapters' focus is on pertinent conformational changes of the extracellular domain of TF. The final chapter describes an interaction of a loop (160-163) in the extracellular domain of TF with the membrane surface that is directly next to critical residues (K165 and K166) involved in binding to FIX and FX. The details of this dissertation will assist in answering important questions about the neurological function of AS and ENSA, as well as giving insights into important details of blood coagulation.

1.6 References

1. Phillips, R., Ursell, T., Wiggins, P., and Sens, P. (2009) Emerging roles for lipids in shaping membrane-protein function. *Nature 459*, 379-385.
2. Lundstrom, K. (2006) Structural genomics. *Mol Biotechnol 34*, 205-212.
3. Singer, S. J., and Nicolson, G. L. (1972) Fluid Mosaic Model of Structure of Cell-Membranes. *Science 175*, 720-&.

4. Mouritsen, O. G., and Bloom, M. (1993) Models of Lipid-Protein Interactions in Membranes. *Annu. Rev. Biophys. Biomol. Struct. 22*, 145-171.

5. Lemmon, M. A. (2008) Membrane recognition by phospholipid-binding domains. *Nat. Rev. Mol. Cell Bio. 9*, 99-111.

6. Fadeel, B., and Xue, D. (2009) The ins and outs of phospholipid asymmetry in the plasma membrane: roles in health and disease. *Crit. Rev. Biochem. Mol. Biol. 44*, 264-277.

7. van Meer, G., Voelker, D. R., and Feigenson, G. W. (2008) Membrane lipids: where they are and how they behave. *Nat. Rev. Mol. Cell Bio. 9*, 112-124.

8. Saunders, M., Wishnia, A., and Kirkwood, J. G. (1957) The Nuclear Magnetic Resonance Spectrum of Ribonuclease. *J. Am. Chem. Soc. 79*, 3289-3290.

9. Williamson, M. P., Havel, T. F., and Wüthrich, K. (1985) Solution conformation of proteinase inhibitor IIA from bull seminal plasma by 1H NMR and distance geometry. *J. Mol. Biol. 182*, 295.

10. Cavanagh, J., Fairbrother, W. J., Palmer, A. G., Rance, M., and Skelton, N. J. (2007) *Protein NMR Spectroscopy:Principles and Practice* 2ed., Academic Press, San Diego, CA.

11. Szilagyi, L. (1995) Chemical-Shifts in Proteins Come of Age. *Prog. Nucl. Magn. Reson. Spectrosc. 27*, 325-443.

12. Wishart, D. S., Sykes, B. D., and Richards, F. M. (1991) Relationship Between Nuclear-Magnetic-Resonance Chemical-Shift and Protein Secondary Structure. *J. Mol. Biol. 222*, 311-333.

13. Wishart, D. S., and Sykes, B. D. (1994) Chemical-Shifts as a Tool for Structure Determination. *Methods in Enzymology, Nuclear Magnetic Resonance, Pt C 239*, 363-392.

14. Wishart, D. S., and Sykes, B. D. (1994) The 13C chemical-shift index: a simple method for the identification of protein secondary structure using 13C chemical-shift data. *J Biomol NMR 4*, 171-80.

15. Shen, Y., Delaglio, F., Cornilescu, G., and Bax, A. (2009) TALOS plus : a hybrid method for predicting protein backbone torsion angles from NMR chemical shifts. *J. Biomol. NMR 44*, 213-223.

16. Zuiderweg, E. R. P. (2002) Mapping protein-protein interactions in solution by NMR Spectroscopy. *Biochemistry 41*, 1-7.

17. Takegoshi, K., Nakamura, S., and Terao, T. (2001) 13C-1H dipolar-assisted rotational resonance in magic-angle spinning NMR. *Chem. Phys. Lett. 344*, 631-637.

18. Morcombe, C. R., Gaponenko, V., Byrd, R. A., and Zilm, K. W. (2004) Diluting abundant spins by isotope edited radio frequency field assisted diffusion. *J. Am. Chem. Soc. 126*, 7196-7197.

19. Hing, A., Vega, S., and Schaefer, J. (1992) Transferred-echo double-resonance NMR. *J. Magn. Reson. 96*, 205-209.

20. Ulmer, T. S., Bax, A., Cole, N. B., and Nussbaum, R. (2005) Structure and dynamics of micelle-bound human alpha-synuclein. *J. Biol. Chem. 280*, 9595-9603.

21. Spillantini, M. G., Crowther, R. A., Jakes, R., Cairns, N. J., Lantos, P. L., and Goedert, M. (1998) Filamentous alpha-synuclein inclusions link multiple system atrophy with Parkinson's disease and dementia with Lewy bodies. *Neuroscience Letters 251*, 205-208.

22. Galvin, J. E., Schuck, T. M., Lee, V. M. Y., and Trojanowski, J. Q. (2001) Differential expression and distribution of alpha-, beta-, and gamma-synuclein in the developing human substantia nigra. *Exp Neurol 168*, 347-355.

23. Maroteaux, L., Campanelli, J. T., and Scheller, R. H. (1988) Synuclein - a Neuron-Specific Protein Localized to the Nucleus and Presynaptic Nerve-Terminal. *J. Neurosci. 8*, 2804-2815.

24. George, J. M., Jin, H., Woods, W. S., and Clayton, D. F. (1995) Characterization of a novel protein regulated during the critical period for song learning in the zebra finch. *Neuron 15*, 361-72.

25. Davidson, W. S., Jonas, A., Clayton, D. F., and George, J. M. (1998) Stabilization of alpha-synuclein secondary structure upon binding to synthetic membranes. *J. Biol. Chem. 273*, 9443-9449.

26. Perrin, R. J., Woods, W. S., Clayton, D. F., and George, J. M. (2000) Interaction of human alpha-synuclein and Parkinson's disease variants with phospholipids - Structural analysis using site- directed mutagenesis. *J. Biol. Chem. 275*, 34393-34398.

27. Eliezer, D., Kutluay, E., Bussell, R., and Browne, G. (2001) Conformational properties of alpha-synuclein in its free and lipid-associated states. *J. Mol. Biol. 307*, 1061-1073.

28. Virsolvy-Vergine, A., Leray, H., Kuroki, S., Lupo, B., Dufour, M., and Bataille, D. (1992) Endosulfine, an endogenous peptidic ligand for the sulfonylurea receptor: purification and partial characterization from ovine brain. Proc. Natl. Acad. Sci. U. S. A. 89, 6629-6633.

29. Bryan, J., Vila-Carriles, W. H., Zhao, G. L., Babenko, A. P., and Aguilar-Bryan, L. (2004) Toward linking structure with function in ATP-sensitive K^+ channels. *Diabetes 53*, S104-S112.

30. Heron, L., Virsolvy, A., Peyrollier, K., Gribble, F. M., Le Cam, A., Aschcroft, F. M., and Bataille, D. (1998) Human alpha endosulfine, a possible regulator of sulphonylurea-sensitive K-ATP channel. *Proc. Natl. Acad. Sci. U.S.A. 95*, 8387-8391.

31. Nichols, C. G. (2006) K-ATP channels as molecular sensors of cellular metabolism. *Nature 440*, 470-476.

32. Drummond-Barbosa, D., and Spradling, A. C. (2004) Alpha-endosulfine, a potential regulator of insulin secretion, is required for adult tissue growth control in Drosophila. *Dev. Biol. 266*, 310-321.

33. Lee, K., Brownhill, V., and Richardson, P. J. (1997) Antidiabetic sulphonylureas stimulate acetylcholine release from striatal cholinergic interneurones through inhibition of K-ATP channel activity. *J. Neurochem. 69*, 1774-1776.

34. Liss, B., Haeckel, O., Wildmann, J., Miki, T., Seino, S., and Roeper, J. (2005) K-ATP channels promote the differential degeneration of dopaminergic midbrain neurons. *Nat. Neurosci. 8*, 1742-1751.

35. Deutch, A. Y., and Winder, D. G. (2006) A channel to neurodegeneration. *Nat. Med. 12*, 17-18.

36. Kim, S. H., and Lubec, G. (2001) Brain alpha-endosulfine is manifold decreased in brains from patients with Alzheimer's disease: a tentative marker and drug target? *Neurosci. Lett. 310*, 77-80.

37. Kim, S. H., and Lubec, G. (2001) Decreased alpha-endosulfine, an endogenous regulator of ATP-sensitive potassium channels, in brains from adult Down syndrome patients. *J. Neural Transm-Supp.*, 1-9.

38. Dou, J. T., Cui, C. H., Dufour, F., Alkon, D. L., and Zhao, W. Q. (2003) Gene expression of alpha-endosulfine in the rat brain: correlative changes with aging, learning and stress. *J. Neurochem. 87*, 1086-1100.

39. Heron, L., Virsolvy, A., Peyrollier, K., Gribble, F. M., Le Cam, A., Aschcroft, F. M., and Bataille, D. (1998) Human alpha endosulfine, a possible regulator of sulphonylurea-sensitive K-ATP channel. *Diabetologia 41*, A138-A138.

40. Morrissey, J. H. (2004) Tissue factor: A key molecule in hemostatic and nonhemostatic systems. *Int J Hematol 79*, 103-108.

41. Daubie, V., Pochet, R., Houard, S., and Philippart, P. (2007) Tissue factor: a mini-review. *J Tissue Eng Regen Med 1*, 161-9.

42. Drake, T. A., Morrissey, J. H., and Edgington, T. S. (1989) Selective Cellular Expression of Tissue Factor in Human-Tissues - Implications for Disorders of Hemostasis and Thrombosis. *Am J Pathol 134*, 1087-1097.

43. Morrissey, J. H., Macik, B. G., Neuenschwander, P. F., and Comp, P. C. (1993) Quantitation of Activated Factor-VII Levels in Plasma Using a Tissue Factor Mutant Selectively Deficient in Promoting Factor-VII Activation. *Blood 81*, 734-744.

44. Morrissey, J. H., and Mutch, N. J. (2006) Hemostasis and Thrombosis: Basic Principles and Clinical Practice, in *Hemostasis and Thrombosis: Basic Principles and Clinical Practice* (Colman, R. W., Marder, V. J., Clowes, A. W., George, J. N., and Goldhaber, S. Z., Eds.) pp 91-106, Lippincott Williams and Wilkins, Philadelphia.

45. Pedersen, A. H., Nordfang, O., Norris, F., Wiberg, F. C., Christensen, P. M., Moeller, K. B., Meidahlpedersen, J., Beck, T. C., Norris, K., Hedner, U., and Kisiel, W. (1990) Recombinant Human Extrinsic Pathway Inhibitor - Production, Isolation, and Characterization of Its Inhibitory Activity on Tissue Factor-Initiated Coagulation Reactions. *J. Biol. Chem. 265*, 16786-16793.

46. Ruf, W., Rehemtulla, A., and Edgington, T. S. (1991) Phospholipid-Independent and Phospholipid-Dependent Interactions Required for Tissue Factor Receptor and Cofactor Function. *J. Biol. Chem. 266*, 2158-2166.

47. Lawson, J. H., Butenas, S., and Mann, K. G. (1992) The Evaluation of Complex-Dependent Alterations in Human Factor-Viia. *J. Biol. Chem. 267*, 4834-4843.

48. Eigenbrot, C., and Kirchhofer, D. (2002) New insight into how tissue factor allosterically regulates Factor VIIa. *Trends Cardiovas Med 12*, 19-26.

49. Paborsky, L. R., Caras, I. W., Fisher, K. L., and Gorman, C. M. (1991) Lipid Association, but Not the Transmembrane Domain, Is Required for Tissue Factor Activity - Substitution of the Transmembrane Domain with a Phosphatidylinositol Anchor. *J. Biol. Chem. 266*, 21911-21916.

50. Eigenbrot, C. (2002) Structure, function, and activation of coagulation factor VII. *Curr Protein Pept Sc 3*, 287-299.

51. Harlos, K., Martin, D. M. A., Obrien, D. P., Jones, E. Y., Stuart, D. I., Polikarpov, I., Miller, A., Tuddenham, E. G. D., and Boys, C. W. G. (1994) Crystal-structure of the extracellular region of human tissue factor (Vol 370, Pg 662, 1994). *Nature 371*, 720-720.

52. Muller, Y. A., Ultsch, M. H., and deVos, A. M. (1996) The crystal structure of the extracellular domain of human tissue factor refined to 1.7 angstrom resolution. *J. Mol. Biol. 256*, 144-159.

53. Huang, M. D., Syed, R., Stura, E. A., Stone, M. J., Stefanko, R. S., Ruf, W., Edgington, T. S., and Wilson, I. A. (1998) The mechanism of an inhibitory antibody on TF-initiated blood coagulation revealed by the crystal structures of human tissue factor, Fab5G9 and TF center dot 5G9 complex. *J. Mol. Biol. 275*, 873-894.

54. Banner, D. W., DArcy, A., Chene, C., Winkler, F. K., Guha, A., Konigsberg, W. H., Nemerson, Y., and Kirchhofer, D. (1996) The crystal structure of the complex of blood coagulation factor VIIa with soluble tissue factor. *Nature 380*, 41-46.

55. Bajaj, S. P., Schmidt, A. E., Agah, S., Bajaj, M. S., and Padmanabhan, K. (2006) High resolution structures of p-aminobenzamidine- and benzamidine-VIIa soluble tissue factor - Unpredicted conformation of the 192-193 peptide bond and mapping of Ca^{2+}, Mg^{2+}, Na^{+}, and Zn^{2+} sites in factor VIIa. *J. Biol. Chem. 281*, 24873-24888.

56. McCallum, C. D., Hapak, R. C., Neuenschwander, P. F., Morrissey, J. H., and Johnson, A. E. (1996) The location of the active site of blood coagulation factor VIIa above the membrane surface and its reorientation upon association with tissue factor - A fluorescence energy transfer study. *J. Biol. Chem. 271*, 28168-28175.

57. McCallum, C. D., Su, B. X., Neuenschwander, P. F., Morrissey, J. H., and Johnson, A. E. (1997) Tissue factor positions and maintains the factor VIIa active site far above the membrane surface even in the absence of the factor VIIa Gla domain - A fluorescence resonance energy transfer study. *J. Biol. Chem. 272*, 30160-30166.

58. Huang, Q. L., Neuenschwander, P. F., Rezaie, A. R., and Morrissey, J. H. (1996) Substrate recognition by tissue factor-factor VIIa - Evidence for interaction of residues Lys(165) and Lys(166) of tissue factor with the 4-carboxyglutamate-rich domain of factor X. *J. Biol. Chem. 271*, 21752-21757.

59. Kirchhofer, D., Lipari, M. T., Moran, P., Eigenbrot, C., and Kelley, R. F. (2000) The tissue factor region that interacts with substrates factor IX and factor X. *Biochemistry 39*, 7380-7387.

60. Ruf, W., Schullek, J. R., Stone, M. J., and Edgington, T. S. (1994) Mutational Mapping of Functional Residues in Tissue Factor - Identification of Factor-Vii Recognition Determinants in Both Structural Modules of the Predicted Cytokine Receptor Homology Domain. *Biochemistry 33*, 1565-1572.

61. Roy, S., Hass, P. E., Bourell, J. H., Henzel, W. J., and Vehar, G. A. (1991) Lysine Residues-165 and Residues-166 Are Essential for the Cofactor Function of Tissue Factor. *J. Biol. Chem. 266*, 22063-22066.

62. Carlsson, K., Freskgard, P. O., Persson, E., Carlsson, U., and Svensson, M. (2003) Probing the interface between factor Xa and tissue factor in the quaternary complex tissue factor-factor VIIa-factor Xa-tissue factor pathway inhibitor. *Eur. J. Biochem. 270*, 2576-2582.

63. Manithody, C., Yang, L. K., and Rezaie, A. R. (2007) Identification of a basic region on tissue factor that interacts with the first epidermal growth factor-like domain of factor X. *Biochemistry 46*, 3193-3199.

64. Kittur, F. S., Manithody, C., Morrissey, J. H., and Rezaie, A. R. (2004) The cofactor function of the N-terminal domain of tissue factor. *J. Biol. Chem. 279*, 39745-39749.

65. Minazzo, A. S., Darlington, R. C., and Ross, J. B. A. (2009) Loop Dynamics of the Extracellular Domain of Human Tissue Factor and Activation of Factor VIIa. *Biophys. J. 96*, 681-692.

66. Ansell, J., Hirsh, J., Poller, L., Bussey, H., Jacobson, A., and Hylek, E. (2004) The pharmacology and management of the vitamin K antagonists. *Chest 126*, 204S-233S.

67. Hauschka, P. V., Lian, J. B., Cole, D. E. C., and Gundberg, C. M. (1989) Osteocalcin and Matrix Gla Protein - Vitamin K-Dependent Proteins in Bone. *Physiol Rev 69*, 990-1047.

68. Price, P. A. (1988) Role of Vitamin-K-Dependent Proteins in Bone Metabolism. *Annu Rev Nutr 8*, 565-583.

69. Friedman, P. A., Rosenberg, R. D., Hauschka, P. V., and Fitzjames, A. (1977) Spectrum of Partially Carboxylated Prothrombins in Plasmas of Coumarin-Treated Patients. *Biochim. Biophys. Acta 494*, 271-276.

70. Malhotra, O. P., Nesheim, M. E., and Mann, K. G. (1985) The Kinetics of Activation of Normal and Gamma-Carboxyglutamic Acid-Deficient Prothrombins. *J. Biol. Chem. 260*, 279-287.

71. Neuenschwander, P. F., Branam, D. E., and Morrissey, J. H. (1993) Importance of Substrate Composition, pH and Other Variables on Tissue Factor Enhancement of Factor VIIa Activity. *Thromb Haemostasis 70*, 970-977.

72. Bom, V. J. J., and Bertina, R. M. (1990) The Contributions of Ca^{2+}, Phospholipids and Tissue-Factor Apoprotein to the Activation of Human Blood-Coagulation Factor-X by Activated Factor-VII. *Biochem. J 265*, 327-336.

73. Komiyama, Y., Pedersen, A. H., and Kisiel, W. (1990) Proteolytic Activation of Human Factor-IX and Factor-X by Recombinant Human Factor-VIIa - Effects of Calcium, Phospholipids, and Tissue Factor. *Biochemistry 29*, 9418-9425.

74. Haverstick, D. M., and Glaser, M. (1987) Visualization of Ca^{2+}-Induced Phospholipid Domains. *Proc. Natl. Acad. Sci. USA 84*, 4475-4479.

75. Fernandez-Chacon, R., Shin, O. H., Konigstorfer, A., Matos, M. F., Meyer, A. C., Garcia, J., Gerber, S. H., Rizo, J., Sudhof, T. C., and Rosenmund, C. (2002) Structure/function analysis of Ca^{2+} binding to the C(2)A domain of synaptotagmin 1. *J. Neurosci. 22*, 8438-8446.

76. Yang, L., and Glaser, M. (1996) Formation of membrane domains during the activation of protein kinase C. *Biochemistry 35*, 13966-13974.

77. Roux, M., and Bloom, M. (1990) Ca^{2+}, Mg^{2+}, Li+, Na^{+}, and K^{+} Distributions in the Headgroup Region of Binary Membranes of Phosphatidylcholine and Phosphatidylserine as Seen by Deuterium NMR. *Biochemistry 29*, 7077-7089.

78. Roux, M., and Bloom, M. (1991) Calcium-Binding by Phosphatidylserine Headgroups - Deuterium NMR-Study. *Biophys. J. 60*, 38-44.

79. Jacobson, K., and Papahadjopoulos, D. (1975) Phase-Transitions and Phase Separations in Phospholipid Membranes Induced by Changes in Temperature, Ph, and Concentration of Bivalent-Cations. *Biochemistry 14*, 152-161.

80. Silvius, J. R., and Gagne, J. (1984) Calcium-Induced Fusion and Lateral Phase Separations in Phosphatidylcholine-Phosphatidylserine Vesicles - Correlation by Calorimetric and Fusion Measurements. *Biochemistry 23*, 3241-3247.

81. Sinn, C. G., Antonietti, M., and Dimova, R. (2006) Binding of calcium to phosphatidylcholine-phosphatidylserine membranes. *Colloids Surf., A 282*, 410-419.

82. Sanson, A., Monck, M. A., and Neumann, J. M. (1995) 2D 1H-NMR Conformational Study of Phosphatidylserine Diluted in Perdeuterated Dodecylphosphocholine Micelles - Evidence for a pH-Induced Conformational Transition. *Biochemistry 34*, 5938-5944.

CHAPTER 2

Experimental Methods and Materials

2.1 Introduction

Acquisition of NMR spectra on proteins and other biological macromolecules requires the preparation of isotopically labeled samples. This includes not only developing expression systems that produce milligram quantities of sample, but also preparing the sample for the NMR tube or rotor. The NMR preparation needs to be stable for extended periods of time and to maintain a biologically relevant state. This chapter will address materials and methods used throughout this document that otherwise would not be addressed in the experimental sections of the individual chapters.

2.2 Protein Preparation and Purification

Protein expression and purification protocols for the proteins studied in this thesis are documented in the subsequent chapters and will not be repeated here. This chapter is dedicated to subtleties in the stability and storage of the protein systems after purified products are produced. This will contain data about wild type endosulfine-α (ENSA), S109E ENSA phosphorylation mutant (S109E), and soluble tissue factor (sTF). Also included will be the preparation of the crystal trays for the production of sTF nanocrystals used for SSNMR.

2.2.1 Wild Type Endosulfine-α

ENSA samples prepared for solution NMR studies were unstable at high concentrations. Samples of ENSA prepared in 50 mM phosphate buffer, pH 7.5 with protein concentrations of 7-13.5 mg/ml (0.5 to 1 mM) allowed for 6-10 days of data collection before visible white aggregates were observed. The ENSA aggregates could be detected in the ^{1}H-^{15}N HSQC NMR

spectra (Figure 1). Broadening of the linewidths and the appearance of new resonances in the spectra (Figure 1b) typified the formation of the ENSA aggregate. Aggregation was faster (~5-7 days) in samples containing lipid mimetics (i.e. SDS, lyso-PG, DPC), the bound form of ENSA (see chapter 4).

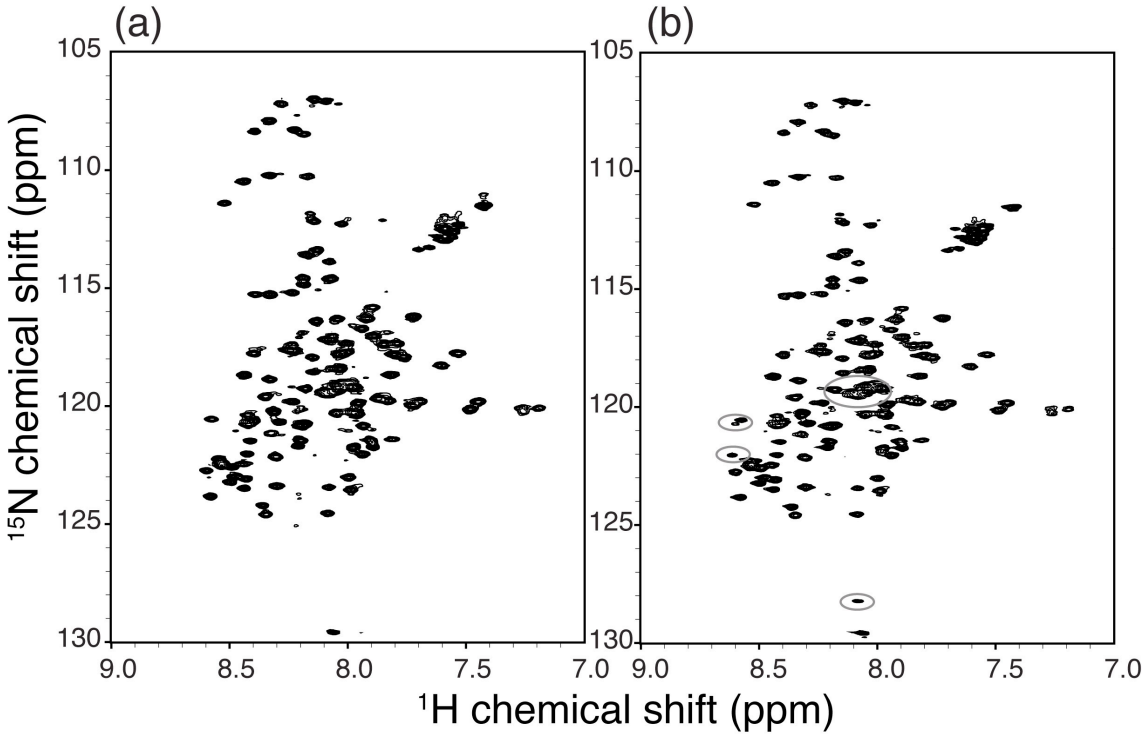

Figure 2.1 ^{15}N-^{1}H 2D HSQC NMR spectra of ENSA; stability tests.

ENSA bound to SDS micelles at 25 ºC. (a) Spectrum taken the first day of sample preparation. (b) Spectrum of the same sample taken after 7 days of data collection. Circled are new resonances that appear in the spectrum after the formation of ENSA aggregates. All the spectra were acquired with 4 scans per row, 512 rows, processed with sine bell apodization and zero filled in each dimension.

Through variation of protein concentration and sample buffer it was determined ENSA aggregation is faster in sample preps with low ionic strength and high ENSA concentrations (>5 mg/ml). ENSA is more stable in low concentrations in buffers with high ionic strength. Therefore, ENSA samples were stored at 4°C in the hydrophobic interaction column (HIC) elution fractions, which contain high levels of ammonium sulfate. ENSA was stored in several HIC fractions keeping the concentration of ENSA low (<2 mg/ml, generally lower than 1

mg/ml). ENSA was stored in this condition for 1-2 months with no appreciable loss to aggregation.

If further NMR studies are carried out on ENSA, changes in the NMR sample preparation could be investigated to produce samples with longer lifetimes. Changes in the pH or the ionic strength of the NMR sample buffers could lead to samples with extended lifetimes. Though, considerations need to be given to the biological relevance and the effect changes in pH and/or ionic strength might have on interactions with membranes and other proteins (i.e. α-synuclein).

2.2.2 S109E: sample preparation for NMR studies

S109E, the phosphorylated mutant of ENSA, produced NMR samples that were stable for extended period of times. Protein kinase A (PKA) can phosphorylate S109 of ENSA (*1*). The S109E sample mimics the phosphorylated state of ENSA. Solution S109E NMR samples were prepared identically to the wild type ENSA samples and had lifetimes of >6 months. Further discussion of the specific effects of phosphorylation on ENSA membrane binding and interactions with other proteins will be discussed in chapter 5.

2.3 Tissue Factor

2.3.1 Soluble Tissue Factor: Propensity to form oligomers

Preliminary evidence points to the formation of oligomers in high concentration sTF samples. One example of the propensity of sTF to form oligomers is from a publication on an sTF crystal structure where Huang *et al*. reported that one of the first sTF crystals were grown by accident in a NMR tube with ~80 mg/ml sTF concentration (*2*). The samples were grown in two days in an NMR tube containing 3.5 mM (~80 mg/ml) sTF at 5° C in a 20 mM phosphate buffer, pH 7.5 (*2*). In Figure 2.2, a sizing column run with ~20 mg of sTF shows three resolved sTF peaks. A sizing gel was run on a fraction of each peak and confirmed that the fractions collected

were sTF. The first peak at 71 ml was pure monomer. The peak at 61 ml contained an sTF-dimer and the peak at 42 ml contained an sTF-trimer. Sizing runs done with less than 10 mg of sTF eluted only monomer sTF at ~71 ml. Since formation of the larger sTF oligomers is a function of the sTF concentration, sTF protein sizing columns were subsequently run with less than 10 mg of sTF and stored at lower concentrations (<5 mg/ml).

Figure 2.2 Sizing column and Gel of high concentrated sTF.

High-resolution gel filtration chromatography (HiPrep 16/160 Sephacryl S-200, GE Biosciences) of 20 mg of sTF was run at 4 °C, with a flow rate of 0.5 ml/minute. STF eluted over a 15 ml volume (29 minutes) in three resolved peaks. Monomer sTF started to elute at approximately 66 ml (132 minutes). The sTF-trimer eluted at 42 ml (84 minutes) and the sTF-dimer at 61 ml (102 minutes).

2.3.2 Soluble Tissue Factor: Solution NMR sample preparation

Various sample conditions were tested for preparation of solution sTF NMR samples to slow the formation of sTF dimers and trimers and extend sample lifetimes. Original sTF solution NMR samples were prepared at ~1mM (~26 mg/ml) concentrations in a 50 mM phosphate buffer

at pH 7.5 and had short lifetimes (~4-5 days). The samples did not aggregate but, as previously mentioned, form larger oligomers. This can be seen in the NMR spectra as a loss of signal to noise as a function of time (Figure 2.3). The loss of signal to noise is due to the broadening of the resonances attributed to the slower correlation time of the larger oligomers. Sample buffers were tested with varying pH levels and ionic strengths. Specifically, phosphate buffers with pH values varying from 4.5 to 8.5 were tested with and without 0-100 mM NaCl. Sample lifetime was increased to ~10 days by preparing the sTF sample buffer with 50 mM phosphate, pH 6.5 and 50 mM NaCl.

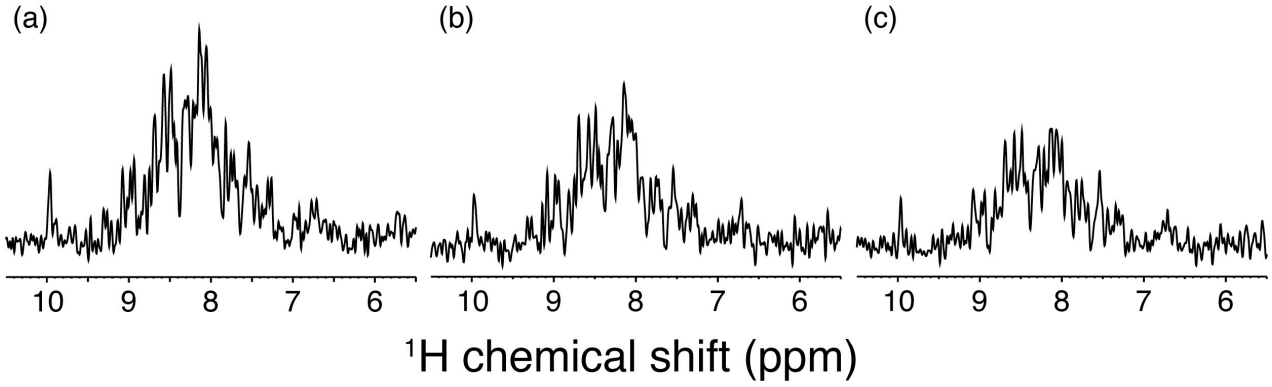

Figure 2.3 Amide proton spectra of sTF.

Loss of signal to noise over time can be seen in the ^{1}H spectra of the sTF amide protons over several days. The spectra show the ^{1}H spectra of the sTF amide protons at (a) time 0, (b) two days and (c) six days. All the spectra were acquired with 8 scans, 512 rows? processed with sine bell apodization and zero filled.

2.3.3 Soluble Tissue Factor: Solid State NMR sample preparation

Investigating varying levels of sTF concentration, PEG3350 and Li_2SO_4 produced a nanocrystalline preparation for SSNMR sTF samples. The choices of precipitants used in the nanocrystalline preps were based on the preparation of single crystals in rabbit sTF (*3*). Microcrystalline sTF is prepared in a solution containing ~1 mM sTF and 15% PEG3350. However, various other conditions produced microcrystals as well (Figure 2.4). The current preparation was chosen to maximize sTF content in the pellet and minimize salt content.

Li_2SO_4 → / ↓PEG	conc. of sTF (mg/ml) ↓	200 μM	150 μM	100 μM	50 μM	25 μM	0 μM
10%	12	clear	QC	MC	QC	phase	QC
	6	clear	clear	MC	QC	phase	MC
	3	clear	clear	MC	MC	clear	MC
20%	12	phase	phase	MC	phase	MC	MC
	6	prec	MC	MC	phase	prec	MC
	3	prec	MC	MC	MC	prec	MC
30%	12	prec	prec	prec	prec	prec/MC	prec/MC
	6	prec	prec	prec	prec	prec/MC	prec/MC
	3	prec	prec	prec	prec	prec/MC	FC
40%	12	prec	prec	prec	prec	prec/MC	prec/MC
	6	MC	prec	prec	prec	prec/MC	prec/MC
	3	MC	prec	prec	prec	prec/MC	prec/MC

Figure 2.4 Crystal Tray sTF.

Varying amounts of Li_2SO_4 and PEG 3350 were used to test precipitation conditions at varying sTF concentrations. In each cell, three droplets of sTF at 3, 6 and 12 mg/ml were tested. Li_2SO_4 started at 200 μM and was decreased in the cells from left to right and PEG increased from 10% (w/v) to 40 % in the cells from top to bottom. The tray was monitored over several weeks and observations were made as to the presence of as microcrystals (MC), precipitation (prec), quasi-crystals (QC), phase separated (phase), clear liquid (clear) or a mix of precipitate and microcrystals (prec/MC).

2.4 References

1. Heron, L., Virsolvy, A., Peyrollier, K., Gribble, F. M., Le Cam, A., Aschcroft, F. M., and Bataille, D. (1998) Human alpha endosulfine, a possible regulator of sulphonylurea-sensitive K-ATP channel. *Diabetologia 41*, A138-A138.

2. Huang, M. D., Syed, R., Stura, E. A., Stone, M. J., Stefanko, R. S., Ruf, W., Edgington, T. S., and Wilson, I. A. (1998) The mechanism of an inhibitory antibody on TF-initiated blood coagulation revealed by the crystal structures of human tissue factor, Fab5G9 and TF center dot 5G9 complex. *J. Mol. Biol. 275*, 873-894.

3. Muller, Y. A., Kelley, R. F., and De Vos, A. M. (1998) Hinge bending within the cytokine receptor superfamily revealed by the 2.4 angstrom crystal structure of the extracellular domain of rabbit tissue factor. *Protein Sci*. *7*, 1106-1115.

CHAPTER 3

Conformation-Specific Binding of Alpha-Synuclein to Novel Protein Partners Detected by Phage Display and NMR Spectroscopy

3.1 Notes and Acknowledgements

This chapter was adapted from Wendy S. Woods, John M. Boettcher, Donghua H. Zhou, Kathryn D. Kloepper, Kevin L. Hartman, Daniel T. Ladror, Zhi Qi, Chad M. Rienstra, and Julia M. George, *J. Biol. Chem.* 2007, *282*, 34555-34567. This work was supported by grants from the Branfman Family Foundation (to JMG), the National Institute on Aging (NIA R01 AG13762, to JMG), the American Parkinson Disease Association (to CMR) and Research Corporation Cottrell Scholars Award (to CMR).

3.2 Abstract

Alpha-synuclein (AS) is an intrinsically unstructured protein in aqueous solution but is capable of forming β-sheet-rich fibrils that accumulate as intracytoplasmic inclusions in Parkinson's disease and certain other neurological disorders. However, AS binding to phospholipid membranes leads to a distinct change in protein conformation, stabilizing an extended amphipathic α-helical domain reminiscent of the exchangeable apolipoproteins. To better understand the significance of this conformational change, we devised a novel bacteriophage display screen to identify protein binding partners of helical AS and have identified 20 proteins with roles in diverse cellular processes related to membrane trafficking, ion channel modulation, redox metabolism, and gene regulation. To verify that the screen identifies proteins with specificity for helical AS, we further characterized one of these candidates,

endosulfine alpha (ENSA), a small cAMP-regulated phosphoprotein implicated in the regulation of insulin secretion, but also expressed abundantly in brain. We used solution NMR to probe the interaction between ENSA and AS on the surface of sodium dodecyl sulfate (SDS) micelles. Chemical shift perturbation mapping experiments indicate that ENSA interacts specifically with residues in the N-terminal helical domain of AS in the presence of SDS but not in aqueous buffer lacking SDS. The ENSA-related protein ARPP-19 (cAMP-regulated phosphoprotein 19) also displays specific interactions with helical AS. These results confirm that the helical N-terminus of AS can mediate specific interactions with other proteins, and suggest that membrane binding may regulate the physiological activity of AS *in vivo*.

3.3 Introduction

Alpha-synuclein (AS) is an abundant constituent of healthy brain tissue, but its normal function is not well understood. In recent years, AS has gained notice due to its association with both inherited and sporadic Parkinson's disease (PD). Mutations in the AS protein sequence are associated with PD (1-3), as are gene duplication events leading to increased expression of the protein (4, 5). AS is also the major fibrillar protein component of Lewy bodies (6), which are associated with both sporadic and inherited PD, as well as Alzheimer's disease, Down's syndrome, and multiple system atrophy (reviewed in (7)). AS was originally identified in three different contexts: as a putative synaptic vesicle protein (8), as a component of protein aggregates in Alzheimer brain tissue (9), and as a gene regulated in the zebra finch song control circuit during the critical period for song learning (10). More recent evidence suggests a role in modulating neurotransmission (11, 12).

AS displays remarkable structural plasticity. While the protein is intrinsically unstructured in aqueous solution, it can adopt multiple distinct stable conformations depending upon its

environment. Upon prolonged incubation in aqueous solution, the protein forms amyloid fibrils rich in β-sheet secondary structure, reminiscent of the pathological fibrils found in Lewy bodies. However, in the presence of acidic phospholipid vesicles, the N-terminus of AS folds into an amphipathic helical conformation that mediates membrane binding (13-15). The hydrophilic face of this helix, which is presumably exposed to the neuronal cytosol (16), is highly conserved at the level of individual amino acids (10), suggesting that interactions with other binding partners have constrained its evolution.

Conventional methods for identifying protein binding partners in solution (e.g., immunoprecipitation, yeast two-hybrid screening) are unsuitable for study of interactions that depend on the helical conformation of AS. Under intracellular conditions, AS appears to be in dynamic equilibrium between membrane and cytosol, and there is thus no practical way to enrich for a particular conformation *in vivo*. We therefore developed a novel *in vitro* approach utilizing bacteriophage display to screen for proteins that bind selectively to AS in its lipid-associated helical conformation. Applying this method, we identified 20 human brain proteins that interact specifically with phospholipid-bound AS. One of these proteins, endosulfine alpha (ENSA), was chosen for further investigation because its small size (13 kDa) is compatible with solution NMR. To characterize the interaction between ENSA and AS in detail, we employed chemical shift perturbation mapping experiments that demonstrate a highly selective interaction between ENSA and specific residues in the N-terminal helical domain of AS. This observation was extended by demonstration of a similar interaction between AS and cAMP-regulated phosphoprotein 19 (ARPP-19), a protein highly related to ENSA that is also enriched in brain.

3.4 Experimental Procedures

3.4.1 Phage Display

N-terminally his-tagged human alpha-synuclein (AS) protein was expressed in *E. coli* via the vector pET28a (Novagen), and purified on Ni-NTA (Qiagen) according to manufacturer's directions. Phospholipid vesicles (3:1 POPC/POPA) were prepared according to published protocols (14, 17); our previous studies indicate that stabilization of the AS helical domain requires acidic phospholipids, and that helix content is specifically maximized by the inclusion of phosphatidic acid (13, 14). 75 μg his-AS was incubated with 1.5 mg vesicles, and protein/vesicle complexes were isolated on a Superose 6 size exclusion column (GE Biosciences). Protein/vesicle complexes were incubated with T7 bacteriophage displaying cDNA from human brain (Novagen T7 Select). 1 X 10^7 pfu were incubated with 5 μg vesicle-bound AS for 1 hour at RT. Ni-NTA agarose beads (Qiagen) were added and the mixture was incubated end-over-end for 2 hours at 4ºC. The suspension was poured into a column and the beads were washed with 20 mM imidazole to remove unbound phage, followed by phospholipid vesicles (protein-free) to elute phage with specificity for POPC/POPA vesicles. Finally, bacteriophage that bound to membrane-bound AS were eluted by addition of purified AS/vesicle complexes. The eluates were pooled and amplified in *E. coli*, then subjected to 3 more cycles of biopanning. After the final round, the eluates were applied to an affinity column prepared with his-tagged AS alone, and the flow-through was collected, to select for phage that did not bind to unstructured (lipid-free) AS. Individual bacteriophage clones were amplified and subjected to sequencing to identify the human brain protein sequences displayed by each.

3.4.2 Recombinant protein expression

Human endosulfine alpha (ENSA) was cloned from the full-length phage clone into the vector pDEST17 (Invitrogen), which encodes the N-terminal his-tagged linker MSYYHHHHHHLESTSLYKKA GSAAAPFT. The ARPP-19 cDNA (Origene) was also cloned into pDEST17. Recombinant protein expression was induced with 0.2% arabinose at 30ºC for 3-4 hours (ENSA) and 5 hours (ARPP-19) and purified on Ni-NTA agarose (Qiagen) according to manufacturer's directions.

An untagged ENSA construct was made in the vector pET21 (Novagen). Protein was expressed by induction with 1mM IPTG at 30ºC, followed by alkaline lysis, boiling, and precipitation with 60% ammonium sulfate. Precipitates were purified by hydrophobic interaction chromatography on a HiPrep 16/10 Butyl Fast Flow Sepharose column (GE Biosciences), and eluted with decreasing salt. ENSA-containing fractions were pooled and concentrated, then subjected to high-resolution gel filtration chromatography (HiPrep 16/160 Sephacryl S-200, GE Biosciences). Purity of recombinant ENSA, his-tagged ENSA, and his-tagged ARPP-19 proteins were confirmed by Coomassie staining. All proteins were shown to be immunoreactive with a chicken polyclonal antibody raised against full-length human ENSA (Abcam ab14297) (Figure 7.1). In addition, predicted molecular weights of recombinant proteins were verified by mass spectroscopy (data not shown).

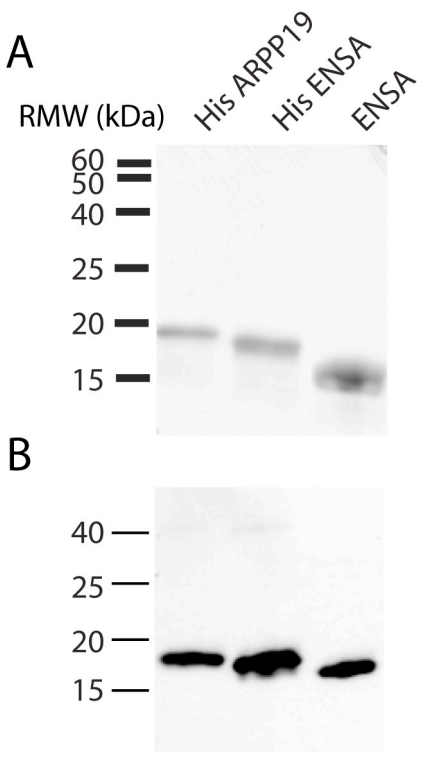

Figure 3.1 Characterization of purified recombinant ENSA and ARPP-19 proteins.

Purified proteins (his-tagged ARPP-19, his-tagged ENSA, and untagged ENSA) were separated by SDS-PAGE, followed by (A) Coomassie staining for total protein or (B) immunoblot with a chicken polyclonal antibody raised against full-length human ENSA. As expected from the similarity of these sequences, the antibody cross-reacts with ARPP-19. (Figure supplied by Wendy Woods and Dr. Julia George.)

Full-length, untagged AS protein was produced for NMR experiments according to published procedures (18). For isotopically labeled protein, cultures were grown in M9 minimal media supplemented with 2 g [^{13}C]-glucose, 1 g [^{15}N]-ammonium chloride, 10 mg biotin, 10 mg thiamine and 10 mL [^{13}C, ^{15}N]-Bioexpress (Cambridge Isotopes Laboratories, Inc., Andover, MA). The final steps of the purification (size-exclusion chromatography and filtration (0.2 μm)) were performed immediately prior to NMR experiments, in order to avoid the presence of oligomeric species of AS.

3.4.3 NMR spectroscopy

Solution NMR spectra were acquired at the VOICE NMR Facility on a Varian INOVA 600 MHz spectrometer equipped with a 5 mm, triple resonance (^{1}H-^{13}C-^{15}N) triaxial gradient probe, using VNMRJ version 2.1B with the BioPack suite of pulse programs released in early 2006. 2D ^{1}H-^{15}N HSQC spectra were measured typically for two hours per spectrum, digitizing 512 complex points in the indirect ^{15}N dimension (t_{1max} = 232 ms). Further details specific to each spectrum are provided in the figure captions. Spectra were processed with NMRPipe (19) and analyzed in Sparky (20), using the previously established assignments of ^{15}N and ^{1}H chemical shifts of AS in the free (21) and micelle-bound states (15, 22). The free state consisted of 0.2 to 0.5 mM ^{15}N-labeled-AS in 50 mM phosphate buffer, pH 7.4, 10% D_2O, and 0.1% DSS as an internal chemical shift reference. The micelle-bound state of AS was prepared by addition of sodium dodecyl sulfate (SDS) directly to the NMR tube, achieving a final concentration of at least 28 mM, i.e., a 140:1 molar ratio of SDS to AS, with the concentration of SDS significantly above its critical micelle concentration. The critical micelle concentration in 50 mM phosphate buffer at 25 °C was determined to be ~2 mM using isothermal titration calorimetry (ITC) (data not shown). In all NMR experiments, the ^{15}N-AS sample was examined in the unfolded state to confirm sample integrity; subsequently, SDS was added to prepare the micelle-bound state, and natural abundance partner proteins were titrated immediately thereafter. Control spectra of AS were highly reproducible and showed no evidence of aggregation, such as peak broadening, changes in chemical shifts as a function of time, or signal intensity losses.

3.4.4 Partner protein titrations

For each partner protein, two series of titration experiments were performed. First, free ^{15}N-AS was prepared as described above and the control HSQC spectrum acquired. To this 0.2 mM

AS solution (400 μL), ~40 μL aliquots of natural abundance partner protein (0.2 mM) were added. HSQC spectra were acquired at each step, up to the point at which AS and the partner protein had equal concentrations. Second, a fresh sample of ^{15}N-AS was prepared in the micelle-bound state, the control HSQC spectrum acquired, and titrations of the same partner protein (without additional SDS) performed over a range of AS to partner protein ratios of 1:0 to 1:1. In a subset of the experiments, the order of addition was changed by first mixing the AS and partner protein in their free states and then adding an excess of SDS, and yet another case the partner protein (ENSA) was first bound to excess SDS before addition to the AS-SDS solution. These procedures all resulted in HSQC spectra corresponding to the final step of the partner protein titration, which were identical to within the limit of statistical significance (~0.01 ppm). The chemical shift perturbation integrating both changes in ^{1}H and ^{15}N chemical shifts was defined as $\delta = ([0.1\ \delta_N]^2 + \delta_H^2)^{1/2}$, considering that the ^{15}N shift covers a range ~10 times that of ^{1}H.

3.5 Results

3.5.1 Binding partners of helical alpha-synuclein by phage display.

Vesicle-bound AS was used to pan a human brain bacteriophage display library as described in Experimental Procedures. After 3-5 rounds of selection, individual clones from the pool were amplified, and their inserts were determined by sequencing with primers flanking the insertion site in the gene encoding coat protein 10B. 338 bacteriophage clones were sequenced, of which 38 yielded readable in-frame sequences of identified human brain proteins. These 38 sequences represented 20 unique proteins, seven of which were isolated more than once and 13 that were single isolates.

In Table 1, the candidates are sorted based upon the functional data available in the literature. Seven of these proteins have been reported previously to interact physically or functionally with

AS under various conditions. These proteins include alpha-tubulin, the sequence isolated with the greatest frequency overall (6/38 bacteriophage clones). Our laboratory

Table 3.1. Interactions with synuclein.

Candidate human brain proteins that interact with helical alpha-synuclein, as identified by bacteriophage display. (Table supplied by Wendy Woods and Dr. Julia George.)

Protein (synonyms)	Uniprot accession #	Function(s)	# Isolates	Prior report of AS interaction
Cytoskeleton/vesicle trafficking				
α-Tubulin	P68363	microbutule subunit	6	(23, 24)
Septin 4 (Sept 4, cdc-rel2)	O43236	cytoskeletal component	2	(26)
Kinesin light chain 1S (KLC1S)	Q07866-8	microtubule motor	3	(27)
Dynein heavy chain 1 (DHC1)	Q14204	microtubule motor	2	(27)
Synapsin 1a	P17600	actin binding, regulates presynaptic vesicle pools	1	
Ectodermal neural cortex 1 (ENC-1NRP/B)	O14682	actin binding, regulates neuronal process formation	4	
Ion channel modulation				
Endosulfine-α (ENSA)	043768	modulates K-ATP channels, L-type Ca^{++} channels	1	
Sorcin (SORCN)	P30626	modulates K-ATP channels, L-type Ca^{++} channels	1	
Annexin A6	P08133	modulates L-type Ca^{++} channels	1	
Redox metabolism				
R-β-hydroxybutyrate dehydrogenase, type 2 cytosolic (BDH2)	Q9BUT1	converts R-β-hydroxybutyrate to acetoacetate	1	
Multifunctional enzyme 2 (MFE2)	P51659	fatty acid beta-oxidation, also reduces estradiol to estrone	1	
Cytochrome C oxidase, subunit 1 (COX1)	Q6RRI3	mitochondrial electron transport	1	(28)
Peroxiredoxin 1 (PRDX1)	Q06830	peroxidase, chaperone	1	
Transcriptional complexes				
Proline-, glutamic acid-, and leucine-rich protein 1 (PELP1, MNAR)	Q8IZL8	co-activator of estrogen receptor alpha, transcriptional co-repressor	1	
SAP30 binding protein (SAP30BP,HCNGP, HTRP)	Q9UHR5	transcriptional co-repressor, possible component of histone deacetylase complex	1	
FK506 binding protein 52 (FKBP52)	Q02790	chaperone, component of steroid receptor complexes	4	(29)
Heat shock cognate 70 (Hsc70, HspA8)	Q96IS6	chaperone, component of steroid receptor complexes, clathrin-uncoating ATPase	4	
Other				
Prefoldin 2 (PFDN2)	Q9UHV9	folding chaperone	1	
Ubiquitin specific protease 47 (USP47)	Q96K76	ubiquitin specific protease	1	
G protein-coupled receptor kinase 2 (GRK2)	P25098	G protein-coupled receptor desensitization	1	(31, 74)

has previously reported that AS binds monomers of alpha- and beta-tubulin (23), and it was recently reported that AS binds monomeric tubulin and stimulates microtubule polymerization (24). Like alpha-tubulin, septin 4 (also known as CDCrel-2) is a filament-forming G protein thought to function as a scaffolding protein for membrane/cytoskeleton interactions (reviewed in (25)); septin 4 was shown to bind AS when the two proteins are co-expressed in cultured cells, and to co-associate with AS in Lewy bodies (26). Kinesin light chain 1S and dynein heavy chain I are components of microtobule motors critical for vesicular and organellar trafficking in neurons and other cells. Our identification of these proteins confirms a previous report by Utton *et al*. that AS interacts with complexes containing either dynein or kinesin-1 in neurons (27). As previously reported by Elkon *et al*. (28), we find that AS binds to cytochrome C oxidase, the mitochondrial complex IV enzyme. FK506 binding proteins, members of the immunophilin protein family, were recently reported to stimulate fibril formation by alpha-synuclein (29); one of these family members, FKBP52, was recovered in our screen. Of the remaining proteins in Table I, only G protein-coupled receptor kinase 2 (GRK2) has been reported to interact with AS in prior studies. GRK2 phosphorylates AS at serine 129, a modification that enhances AS inclusion formation in cell culture (30) and in a Drosophila model of PD (31).

The sizes of the cDNA inserts in the bacteriophage library vary, but generally encode no more than 200 amino acids of the corresponding human brain proteins. This means that in many cases a protein domain sufficient for interaction with AS can be inferred from the sequence of the phage insert. These preliminary "AS-binding domains" are mapped in Figure 2, along with known functional domains when available.

For our present purpose, of greatest interest are the 13 interacting proteins identified for the first time in this screen. These may represent interactions that depend specifically on assumption

of a lipid-dependent helical structure. Each of these interactions is worthy of specific study; here we focus on detailed characterization of the interaction with endosulfine alpha (ENSA), the smallest protein in the set. ENSA was originally described as an endogenous ligand for the sulfonylurea receptor SUR1 (32), a subunit of the ATP-sensitive K+ channel. ENSA is abundant in the brain, where its expression is downregulated in Alzheimer's disease (33) and Down's syndrome (34).

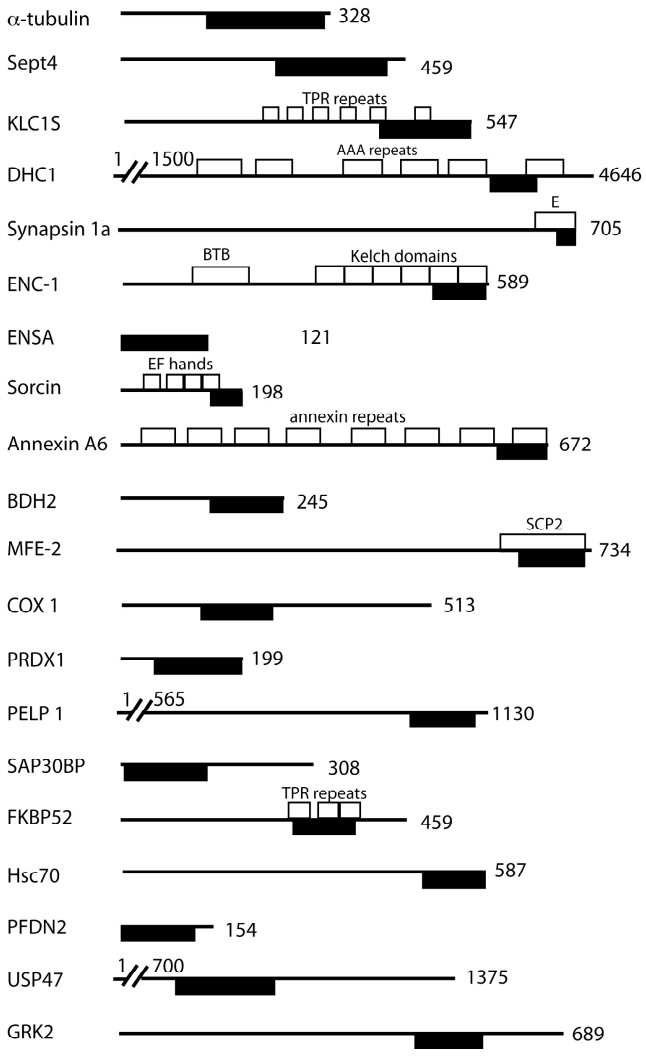

Figure 3.2 Alignment of phage-displayed sequences with full-length human proteins.

Sequences of bacteriophage inserts (solid rectangles) are aligned with the corresponding full-length human sequences (black lines). Known functional domains in the full-length proteins are also depicted

for comparison (open rectangles). Sequence lengths are drawn to scale, except as indicated by broken lines. (Figure supplied by Wendy Woods and Dr. Julia George.)

3.5.2 NMR characterization of AS-ENSA interactions.

NMR chemical shift perturbation mapping experiments were undertaken to determine the conformation dependence and structural specificity of the interactions between AS and ENSA. First, we tested for interactions between non-helical AS and ENSA. ^{15}N-AS was prepared in aqueous buffer at ~0.5 mM concentration. The ^{1}H-^{15}N HSQC spectrum was acquired and

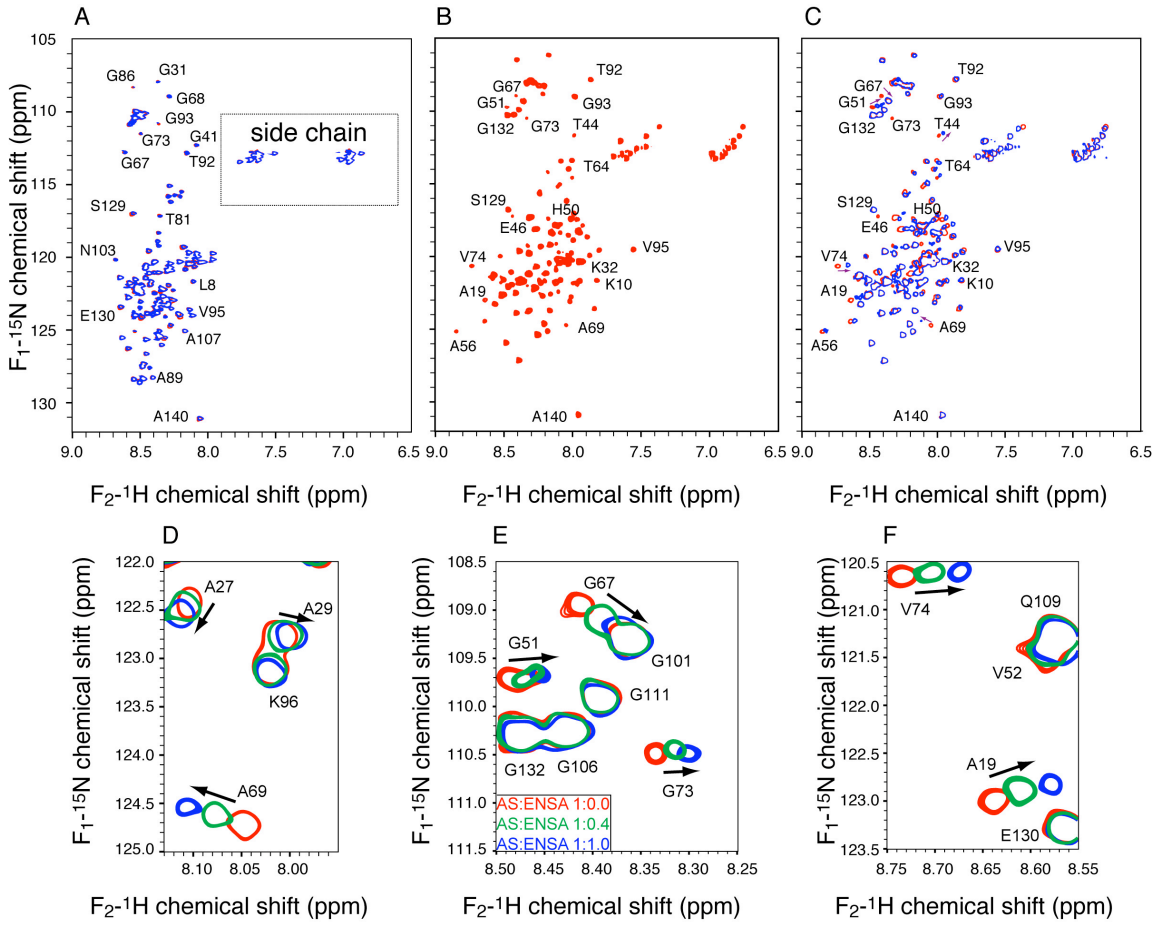

Figure 3.3 ^{15}N-HSQC NMR spectra of ENSA interacting with AS.

This interaction requires an anionic micelle. (A) Spectrum of 0.5 mM free AS (red) overlaid with the spectrum of the sample after addition of ENSA in a 1:1 molar ratio (blue). Both spectra were acquired at 10° C. (B) Spectrum of a 0.5 mM AS sample with excess SDS (83 mM). The spectrum was acquired at 25° C. (C) The same spectrum in (B) (red) overlaid with a spectrum of the sample with the addition of ENSA in a 1:1 molar ratio (blue). All spectra were acquired with 4 scans per row and 512 complex points

in the ^{15}N dimension, and processed with sine bell apodization and zero filling prior to Fourier transformation. (D-F) Expanded regions of the spectrum demonstrating chemical shift perturbations of specific residues upon titration of SDS-bound AS with ENSA. Ratios of AS to ENSA are 1:0 (red), 1:0.4, (green) and 1:1.0 (blue).

confirmed to be consistent with the unfolded state of AS as previously reported by Eliezer (15, 35) (Fig. 3A). Superimposed on the spectrum of pure ^{15}N-AS is the spectrum of ^{15}N-AS with an equimolar quantity of ENSA. The peak positions throughout the spectrum remain essentially unchanged, with the exception of a portion of the C-terminal domain of AS, where some changes on the order of 0.01 ppm were observed. Elsewhere, changes in the spectra were within the random error of the chemical shift measurements (δ ~0.01 ppm). Sources of uncertainty in the chemical shifts include slight changes in pH or buffer concentration; therefore all the protein solutions were prepared by dialysis against a common buffer solution to minimize such effects.

Next, we evaluated the interaction between ENSA and helical AS. A fresh ^{15}N-AS sample was prepared and SDS was added to create an excess number of detergent micelles, in the presence of which AS forms a stable, folded hairpin helical structure throughout the N-terminal ~100 residues (36). The stoichiometric excess of SDS, as previously determined by Eliezer (15) and utilized in studies by Chandra (22) and Ulmer (22, 36), was confirmed in our experiments by titrating SDS into a solution of free AS. We confirmed that the molar ratio of approximately 70:1 SDS:AS was required to ensure that all AS molecules were micelle-bound. Addition of SDS beyond the 70:1 molar ratio causes only small changes, and in the range studied here for protein-protein interactions, from ~100:1 to 200:1 SDS:AS ratio, there are no chemical shift perturbations of significance (>0.01 ppm; see Figure 4). All of the subsequent titrations involving helical AS were carried out in molar ratios ≥ 140:1 SDS:AS, which is more than sufficient for complete binding of AS. Moreover, a ~50% or greater excess of unpopulated

micelles remains available in the solution for binding to the candidate protein. The spectrum of ^{15}N-AS on a micelle (Figure 3B) agrees well with published chemical shifts for ^{15}N and ^{1}H.

When ENSA was then added, systematic and highly reproducible changes in the spectra occurred. Fig. 3C illustrates the beginning and end points of the ENSA titration, where the chemical shift perturbation is most easily identified. The signals fall into three categories. First, many signals show substantial changes in chemical shift, i.e., the peak positions change by significantly more than the total peak line width. For example, A19, E20, T44, G51, A69, V71, and V74 are residues that show such unambiguous changes. Second, many other resonances show smaller shifts between 0.05 and 0.10 ppm δ_N; examples include K12, T14, A30, V49, A56, T81 and A89. Finally, dozens of peaks (such as A17, E13, Q24, G25 and T75) shift by less than 0.05 ppm in the ^{15}N dimension but still significantly more than the random error in the measurements.

Fig. 3D-F shows the chemical shift changes systematically as a function of ENSA concentration. The progression of peak positions from the initial to final state is continuous and approximately linear with the ENSA concentration. For example, the G67 (Fig. 3E) resonance moves down (downfield in ^{15}N) and to the right (upfield in ^{1}H) by more than 0.1 ppm δ_N. A69 (Fig. 3D) changes most significantly in the ^{1}H dimension. In other regions of the spectrum, several resonances such as A27, G73 and V74 (Fig. 3D, E, F) show a similar pattern. Other resonances move by smaller total amounts, but typically in a linear manner with concentration.

At no point in the titration of ENSA were multiple peaks observed for a given AS amide ^{1}H-^{15}N site. This is consistent with a fast chemical exchange process, in which there is an interconversion between (1) the micelle-bound state of AS and (2) the micelle-bound state of AS in complex with the micelle-bound state of ENSA. (Several biophysical methods, including

NMR (37), isothermal titration calorimetry (ITC), and circular dichroism (CD) spectroscopy (Boettcher et al., unpublished data) demonstrate strong binding of ENSA to SDS micelles, accompanied by a substantial change in secondary structure). If this process were slow (exchange rates of much less than 1,000 s^{-1}), each molecule would be either in state 1 or 2 during the course of the NMR acquisition, and two signals would be observed for each residue. Instead, characteristic of the fast exchange process (rates much greater than ~1,000 s^{-1}), the weighted average of the chemical shifts of the states 1 and 2 is observed. The exact peak position therefore depends upon the populations of states 1 and 2 (38, 39); the population of state 2 gradually increases throughout the titration, and therefore the peak gradually moves in this direction.

In Fig. 4 the chemical shift perturbations are plotted as a function of residue number. Fig. 4A illustrates the very small effects of adding ENSA to a solution of AS in the absence of

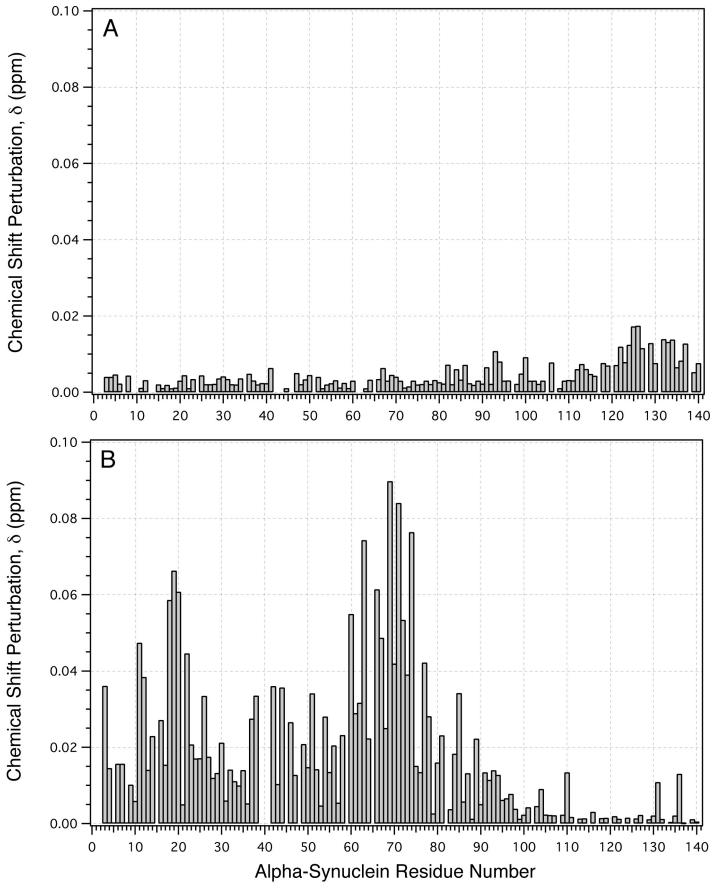

Figure 3.4 Chemical shift perturbations upon titration of AS with ENSA.

The perturbations ($\delta = ([0.1\delta_N]^2 + \delta_H^2)^{1/2}$) were calculated for well-resolved sites in the 2D HSQC spectra. (A) Perturbations of free AS by the addition of ENSA at 1:1 molar ratio. (B) Perturbations of SDS-bound AS by the addition of ENSA at 1:1 ratio

SDS. We interpret this as corresponding to no observable change in structure and minimal interaction between the unfolded proteins (primarily in the C-terminus of AS). Fig. 4B illustrates the corresponding shifts observed, for the end point of the titration, in the presence of SDS. In this case, large chemical shifts are observed in many positions throughout AS, including many prominent shifts throughout the N-terminal domain, which are not seen at all in the unfolded state. Analysis of ^{15}N T_2 relaxation (Table II) is consistent with a population of SDS-AS-ENSA ternary complex that is larger than the SDS-AS binary complex. The transverse relaxation times were measured from the ^{15}N linewidths of HSQC spectra on AS in three different states (free in

solution, bound to SDS micelles, and in the SDS-AS-ENSA complex), and the correlation time computed assuming an isotropic tumbling model under standard conditions (75).

Table 3.2. Results of the ^{15}N linewidth analysis.

For each state three different spectra were analyzed and the averages and standard deviations are reported. In all states C-terminal residues 90 to 140 are unbound and these residues were excluded from the analysis. T_2 is the transverse relaxation time constant, R_2 is equal to the inverse of T_2 and τ_c is the calculated correlation time.

Sample	T_2 (ms)	R_2 (s^{-1})	τ_c (ns)
Free AS	51.2±1.8	19.8±0.7	10.5±0.4
SDS-AS	35.7±1.0	28.0±0.8	15.2±0.4
SDS-AS-ENSA	32.5±0.7	30.8±0.7	16.8±0.4

3.5.3 Common AS-binding domain in ARPP family proteins.

ENSA is a member of the cAMP-regulated phosphoprotein family, which also includes cAMP-regulated phosphoproteins ARPP-16 and ARPP-19. ARPP-16/19 are differentially spliced products of the same gene, found at the chromosomal locus 15q21.2 in humans (Unigene Hs.512908, (40)), and are identical except for their extreme N-termini. ENSA is the product of a distinct gene at the locus 1q21(41), which also differs from ARPP-16/19 primarily at the N-terminus. A central domain of 66 amino acids is highly conserved among ENSA and ARPP-16/19 (Fig. 5), suggesting that these proteins might interact similarly with helical AS. To test this hypothesis, recombinant his-tagged ARPP-19 was prepared, and its interactions with AS were assessed by solution NMR.

Figure 3.5 Alignment of the amino acid sequence of ENSA with ARPP-16 and 19.

ARPP-16 and –19 are differentially spliced products of the same gene, and differ only at their N-termini. Boxed residues are identical among the sequences. The conserved PKA phosphorylation site is indicated (*). (Figure supplied by Wendy Woods and Dr. Julia George.)

The NMR data illustrate the qualitatively similar behavior of AS when titrated with ARPP-19 as when titrated with ENSA. AS shows no substantial changes in the spectra when AS and ARPP-19 are combined in free aqueous solution; the spectra of ^{15}N-AS, with and without a stoichiometric equivalent of ARPP-19 in the solution, are essentially identical within experimental error. No ^{15}N chemical shifts vary by more than 0.02 ppm. Figure 6 illustrates changes from the starting point of the SDS micelle-bound AS sample, as ARPP-19 is added. Throughout the ARPP-19 titration, many of the same features in the spectra of ^{15}N-labeled AS are observed as in the aforementioned ENSA titration experiments. Common observations include: (1) the chemical shift changes are systematically observed at many sites throughout the molecule;

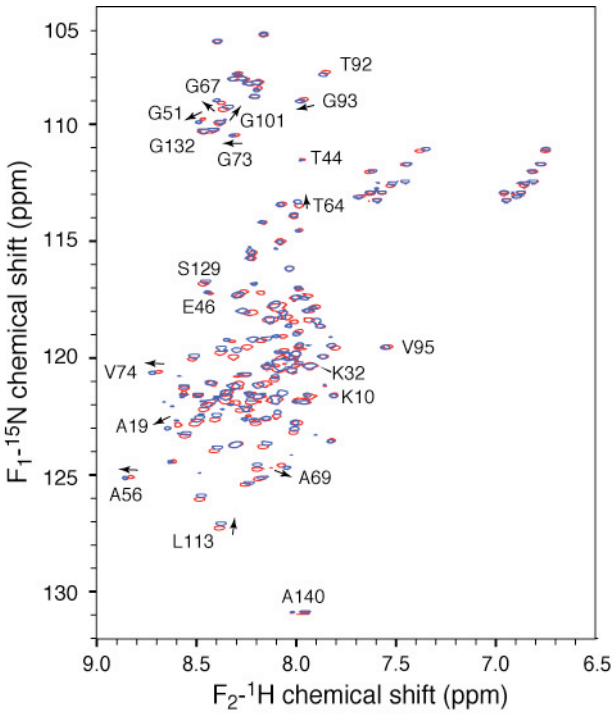

Figure 3.6 ^{15}N-HSQC NMR spectra of AS interacting with ARPP-19.

Spectrum of 0.5 mM ^{15}N-AS sample with excess SDS (83 mM) (red) is overlaid with the spectrum of the sample after the addition of ARPP-19 in a 1:1 molar ratio (blue). The spectra were acquired at 25° C, with 4 scans per row and 512 complex points in the ^{15}N dimension, and processed with sine bell apodization and a single zero fill.

(2) the changes are approximately linear with partner protein concentration; (3) at no time are multiple resonances observed for an individual AS residue. Plotting the chemical shift changes as a function of residue number (Fig. 7) illustrates significant shifts throughout AS in the presence of SDS. As with the plot of ENSA data in the same format (Fig. 4), a qualitatively similar pattern of changes is observed in the N-terminal domain. The major difference observed for the titration of SDS micelle-bound AS with ARPP-19 (which bears an N-terminal his-tag) as compared to ENSA (which is untagged) is the presence of chemical shift perturbations >0.02 ppm in the C-terminal 45 amino acids. Similar C-terminal perturbations were observed in control experiments when SDS-bound AS was titrated with his-tagged ENSA (data not shown),

suggesting that these perturbations result from a secondary electrostatic interaction between the basic his-tag and the acidic C-terminus of AS.

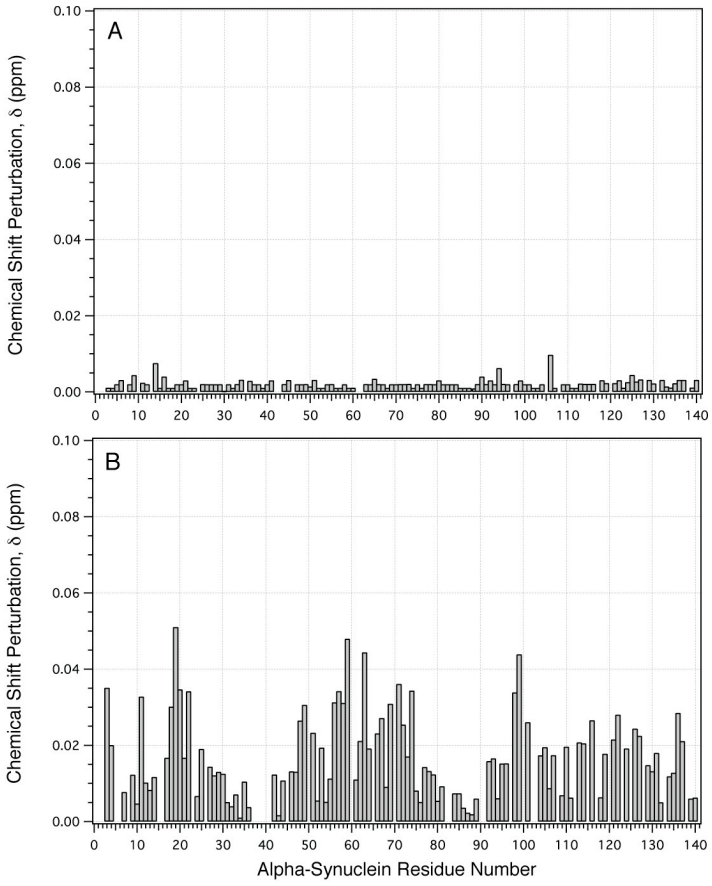

Figure 3.7 Chemical shift perturbations of AS upon titration with ARPP-19.

(A) Perturbations with the absence of SDS. (B) Perturbations in the presence of excess SDS. The perturbations were calculated ($\delta = ([0.1\delta_N]^2 + \delta_H^2)^{1/2}$) for well-resolved sites in the 2D HSQC spectra.

3.5.4 AS and ENSA do not simply compete for binding to micelles.

The final NMR titration experiments were performed starting with stoichiometric equivalents of ^{15}N-AS and natural abundance ENSA in aqueous buffer, titrating with increments of 35 equivalents of SDS per titration point (Fig. 8). The control spectrum (not shown) with no SDS reproduces the experiment shown in Fig. 3A. The first titration point, at a stoichiometry of 35:1:1 SDS:AS:ENSA, corresponds to one-half micelle for every two protein molecules. All

signals corresponding to backbone amide sites in the first ~95 residues of AS are suppressed below the limit of detection sensitivity, due either to the long global correlation times of the micelle occupied by several protein molecules or chemical exchange among multiple micelle-

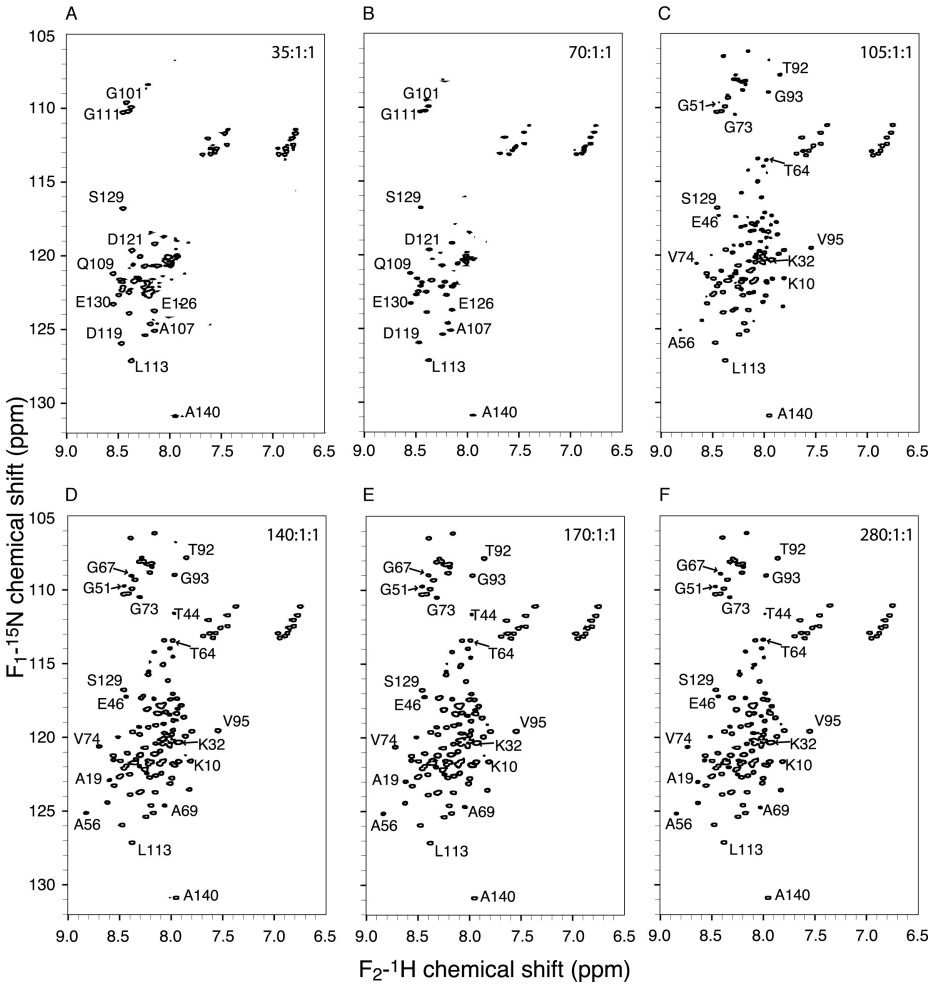

Figure 3.8 ^{15}N-HSQC NMR spectra of labeled AS in a 1:1 molar ratio with ENSA.

^{15}N-HSQC NMR spectra of labeled AS in a 1:1 molar ratio with unlabeled ENSA titrated with SDS. SDS:AS:ENSA ratio is (A) 35:1:1, (B) 70:1:1, (C) 105:1:1, (D) 140:1:1, (E) 170:1:1, (F) 280:1:1. All spectra were acquired at 25° C, with 4 scans per row and 1024 complex points in the ^{15}N dimension, processed with sine bell apodization, 3 Hz of Gaussian line broadening in the indirect dimension, a single zero-fill for both dimensions.

populated species. Only signals in the C-terminal domain of AS (including A107, Q109, G111, D119, S129 and A140), as well as the sidechain Asx and Glx signals, are observed under these conditions; these same signals are observed in solution NMR spectra of AS bound to small

unilamellar vesicles (15), owing to the flexibility of this domain (i.e., its rapid domain motion on the NMR timescale). The N-terminal residues bound to the micelle are, however, broadened beyond detection and only begin to be observed at the ratio of 70:1:1 SDS:AS:ENSA (Fig. 8B). At this point, with approximately one micelle for every two proteins, a small population of micelles with only one AS is observed; these signals begin to emerge with significant sensitivity as the number of micelles with one bound protein increases (i.e., at 1.5 micelles, or 105 molecules of SDS, for each AS-ENSA pair, Fig. 8C). Signals that arise over this range of the titration include many readily assigned to the N-terminal domain of AS, such as K10, A19, K32, E46, G51, T44, A56, G67 and V74. As the number of micelles approaches the number of proteins (Fig. 8D), the intensity of the AS N-terminal domain signals reaches a plateau, corresponding to an equilibrium population in the limit of excess SDS (Fig. 8D). Addition of further SDS (Figs. 8E and 8F) yields no further changes in peak positions or (beyond the dilution factor) peak intensity.

3.6 Discussion

3.6.1 Enrichment for conformation-dependent binding partners of alpha-synuclein

We conducted a screen for proteins that interact specifically with the helical conformation of AS, and identified 20 candidate proteins, including 7 proteins previously reported to interact physically or functionally with AS, and 13 novel partners. Using solution NMR, we performed a rigorous validation of the conformation-specific interaction of AS with one of these novel proteins, ENSA. Our results provide further insight into the potential physiological function of AS and support the hypothesis that AS is sensitive to local environments within the cell and may modulate its interactions with diverse protein partners according to these environments.

We applied a two-stage screening study to select for interactions that occur only in the presence of lipids. In the first phase, we selected for binding partners of membrane-bound alpha-synuclein, a complex including both the helical N-terminus and the relatively unstructured C-terminus. This was followed by a subtractive step to select against binding partners that bound to lipid-free synuclein. Thus our approach should have enriched for conformation-dependent binding partners, but might not have rigorously excluded proteins that interact with the C-terminus, depending on the efficacy of the subtractive step. Indeed, two of the proteins identified in this screen (α-tubulin and cytochrome C oxidase) have been previously reported to interact with lipid-free AS (23, 24, 28). To specifically validate the conformation-dependence of interactions we used solution NMR experiments, as discussed below.

Our results confirm previous reports that AS interacts with elements of the cytoskeleton, especially microtubules and their associated motor proteins (23, 24, 27). However, an interesting candidate emerged from this category: synapsin 1a, which to our knowledge has never been reported to bind AS. Synapsin and AS share intriguing similarities. Both associate reversibly with presynaptic vesicles, and are thought to influence the activity-dependent recruitment of a reserve pool of vesicles to the readily-releasable pool (12, 42). The specific sequence isolated from our bacteriophage screen corresponds to domain E of synapsin 1a (Figure 3.2), a region specifically implicated in this process (43, 44).

Four candidates in Table I participate in various transcriptional complexes. The name "synuclein" is derived from the early report of its localization to both synapses and nuclei (8), and several recent studies confirm its nuclear localization (45, 46), where it is found to interact with histones and to inhibit histone acetylation. Indeed, another synuclein protein family member, gamma-synuclein, has been reported to function as a chaperone for estrogen receptor-

alpha, stimulating ligand binding and activation of the receptor (47). While the conformation dependence of AS interactions with these partners remains to be determined, the potential association of AS with nuclear receptor complexes is intriguing.

Four additional candidates have functions related to redox metabolism. These AS/partner protein interactions may be of particular interest in AS pathology, as PD pathogenesis is strongly linked to mitochondrial dysfunction and oxidative stress. As previously reported by Elkon et al. (28), we find that AS binds to cytochrome C oxidase, the mitochondrial complex IV enzyme. We also observe a novel interaction with a newly identified type 2 cytosolic R-β-hydroxybutyrate dehydrogenase (BDH2). Its substrate R-β-hydroxybutyrate is beneficial in alleviating mitochondrial inhibition and oxidative stress in several animal models of PD (48-50), so intracellular regulation of its metabolism by AS is potentially very significant.

Three of the candidate proteins identified in this screen, sorcin(51), annexin A6(52), and endosulfine alpha(53), have been reported to directly modulate the activities of ion channels. These observations suggest a role for AS in modulation of neuronal excitability, interesting because AS has been reported to negatively regulate neurotransmission (11, 12). Endosulfine alpha (ENSA) was originally identified as an endogenous regulator of K-ATP channels (32), although this potential function remains controversial (54, 55). We chose ENSA as a specific focus for additional validation by chemical shift perturbation mapping experiments because 1) its relatively small size makes it especially amenable to study by solution NMR, and 2) it was previously reported to be downregulated in Alzheimer's disease (33), Down's Syndrome (34), and several models of learning and stress (56).

3.6.2 Structural analysis of AS-ENSA interaction.

NMR chemical shift perturbation mapping experiments were carried out both to demonstrate site-specific effects and to provide a structural context for data interpretation. AS in aqueous solution is unfolded, with only a small degree of secondary structure; in this state, only non-specific interactions between AS and the partner proteins are observed, involving residues in the acidic C-terminus of AS with ENSA, which has a net positive charge at pH 7.5. The amplitude of these effects is in most cases less than 0.003 ppm, with changes on the order of 0.01 ppm for only a few residues. With ARPP-19, even the C-terminus of AS shows only extremely small changes.

In contrast, the micelle-bound state of AS, which has a distinct helical hairpin fold as recently determined by Ulmer et al. (36), gives rise to a consistent and systematic pattern of chemical shift perturbations. These chemical shift patterns observed for ^{15}N-AS in the presence of ENSA are appreciated in the context of the 3D structure of AS (Fig. 9). The AS structure (PDB entry 1XQ8) as determined by Ulmer et al. (36) is illustrated with residues color-coded according to the magnitude of the chemical shift perturbation observed at the highest concentration of ENSA used here. Blue residues have less than 0.015 ppm shifts, which is likely of no significance. White and pink range from 0.015 ppm to ~0.035 ppm, significantly greater than the noise or uncertainty of peak positions. Darker red sites have greater than 0.035 ppm shifts, which are highly significant, an order of magnitude greater than the random measurement error. The ribbon diagram (Fig. 9A) is labeled with specific amino acid locations, and the van der Waals radii depiction (Fig. 9B) emphasizes the strong correlation of perturbed sites with 3D structure.

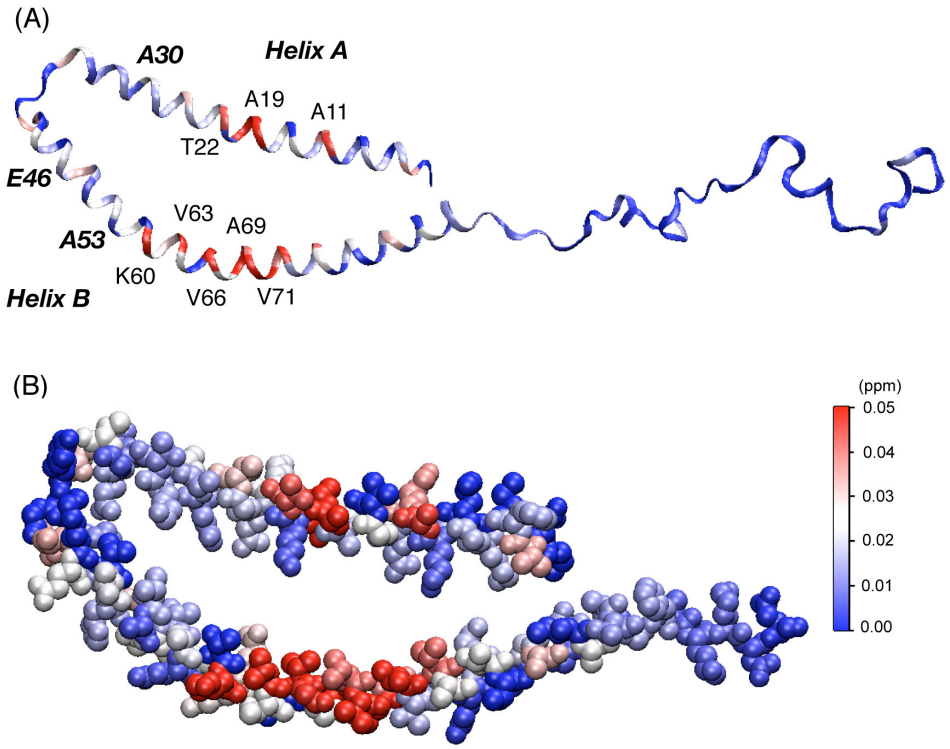

Figure 3.9 Chemical shift perturbation mapping of SDS micelle-bound AS.

Chemical shift perturbation mapping of SDS micelle-bound AS upon interaction with ENSA. (A) Ribbon diagram of SDS micelle-bound AS structure (PDB entry 1XQ8, Ulmer et al.) in ribbon format, with key positions in the sequence labeled by amino acid residue. Sites of PD-associated mutations are indicated in bold. (B) The same structure and point of view in van der Waals representation. The chemical shift perturbation was defined as $\delta = ([0.1\delta_N]^2 + \delta_H^2)^{1/2}$).

Using this structure, the pattern of chemical shift perturbations illustrates the regiospecific interaction. The C-terminal domain (far right unfolded region in Fig. 9A) of AS has no significant perturbations, but the N-terminal domain of SDS-bound AS has a number of prominent perturbations upon addition of ENSA. Residues V3, A11, K12, A19, E20, T22 and V26 all change by more than 0.03 ppm, more than 0.06 ppm in the case of A19 and E20 (as summarized in Fig. 7B), and additional changes of significance (>0.015 ppm) are observed throughout the subsequent two turns of the helix, with residues Q24, G25, A27, E28, A29 and A30, the latter being one of the early-onset PD mutation sites. These residues in the N-terminal helix (helix A) are close in 3D space to a second set of residues in helix B, starting at

approximately K58 (across from E28) and extending to V74 (across from A11). All resolved signals in this K58 to V74 stretch show changes of >0.02 ppm K60, V63, V66, A69, V71 and V74 change by more than 0.05 ppm, an order of magnitude greater than the threshold of significance. (Signals for residues T59 and N65 are not sufficiently well resolved to determine the perturbation values.) Both micelle-facing residues (V52, Q62, V77, T81) as well as solvent-exposed residues (E61, T72, A76), are perturbed significantly, indicating subtle but significant structural effects on both sides of the helix. The locations of these interactions both on helices A and B, close in the folded structure but distant in the primary sequence, imply that ENSA is likely to have a specific interaction with this domain of the folded AS molecule on the micelle.

A third region that is significantly perturbed includes the loop between helices, from V37 to G47, and the start of helix B. Residues in the loop demonstrating significant chemical shift perturbations include T44, E46, H50, V52, A53 and T54; among these are two of the early-onset mutation sites in AS, as labeled on Fig. 9. The other mutation site, A30P, is near the region of significant perturbations in helix A. Reorientation of this helix or substantial differences in the dynamics, as observed in recent studies (36, 57), may alter binding affinity with ENSA.

One trivial explanation for the observed perturbations is that they arise from competition for micelle surface area. For example, some AS signals with perturbed chemical shift were facing the micelle. This raised the question of whether AS and ENSA were competing for a common micelle, so that the chemical shift perturbations on the solvent-exposed surface of AS were an indirect consequence of this competition. Several lines of evidence rule out this possibility.

First, the chemical shift perturbations upon addition of ENSA to the SDS-bound AS sample are on average only a few percent of the chemical shift changes observed upon AS folding. Second, if ENSA were displacing AS from the micelle, the chemical shifts would move

systematically back in the direction of unfolded AS. This also is not the case; rather, chemical shifts are perturbed in directions that are not correlated to the free state of AS, but a third state (i.e., the molecular complex consisting of AS-SDS and ENSA-SDS). Third, a competition for the micelle would result primarily in changes of chemical shifts corresponding to those sites with the strongest interactions with the micelle, such as the Lys residues whose sidechains specifically coordinate with the phosphate headgroups, or the other aliphatic residues that have sidechains buried into the detergent. Although some micelle-facing residues are perturbed upon addition of ENSA to the SDS-bound AS sample, these are by no means the only residues demonstrating shifts, and indeed many of the largest shifts are observed for sites that face the aqueous environment. The observations in all three cases suggest a model of each protein (AS and ENSA) bound to its own micelle and interacting at the interface.

We tested this hypothesis directly by performing an additional series of experiments in which SDS was titrated into a solution of ^{15}N-AS and natural abundance ENSA in equimolar quantities (Fig. 8). These spectra show that in the limit of excess protein (e.g., SDS ratios of 35:1:1, 70:1:1 or 105:1:1, where there would be respectively 0.5, 1.0 or 1.5 micelles for every 2 protein molecules), high molecular weight complexes and/or species in intermediate chemical exchange are present. Signals from the N-terminal domain of AS are broadened beyond detection (as observed by Eliezer with small unilamellar vesicles (15)). As the number of micelles approaches and then exceeds the number of protein molecules, the signals from AS increase in intensity substantially. Once a sufficient excess of SDS is achieved, no further changes occur. For example, in Fig. 8C, signals corresponding to the micelle-bound states of E46, A56, T64, G73, V74, T92 and G93 appear, and these signals increase in strength as the SDS-to-protein ratio is further increased to 140:1:1 (Fig. 8D) and 170:1:1 (Fig. 8E). Only a few subtle changes are

observed between these two spectra, and addition of a further large excess of SDS (to a final ratio of 280:1:1, or 4.0 micelles per 2 protein molecules, Fig. 8F) causes no further changes.

This experiment demonstrated that the order of addition of reagents did not influence the result and the result does not depend on the precise amount of SDS once in sufficient excess. Based on this result, we performed all the partner protein titration experiments with sufficient excess of SDS (at least 170 molecules of SDS per AS molecule).

3.6.3 Functional significance of AS interactions with ENSA and ARPP-16/19.

The precise cellular functions of the cAMP-regulated phosphoproteins ENSA and ARPP-19 are still unclear. Despite their high degree of primary sequence similarity, these two proteins have been characterized independently and in quite varying contexts. ENSA was originally described as an endogenous ligand for the sulfonylurea receptor SUR1 (32), a subunit of the ATP-sensitive K^+ channel. ARPP-16 and -19, along with ARPP-21 and DARPP-32, were originally described as robust phosphorylation substrates for PKA in brain (58). It is speculated that ARPP-16 may be involved in dopamine signaling, as it is enriched in basal ganglia, phosphorylated as a result of D1 dopamine receptor activation, and dephosphorylated in response to D2 activation (59). Its precise cellular function has not been defined, however. Similar to ENSA, expression of ARPP-19 is downregulated in Down's syndrome and Alzheimer's disease; this is accompanied by a downregulation of PKA (60). While our data do not immediately reveal a specific function for AS, or for the interaction between AS and ARPP family members, it is suggestive of participation by these proteins in a protein signaling network associated with G protein-coupled receptors.

We have mapped the domain of AS interaction with ENSA to residues in the N-terminal helical domain of AS, a region that is structured only in the presence of membrane lipids or lipid

mimetics. We have determined the K_d of the AS-ENSA interaction to be ~61±12 μM in the presence of SDS micelles, based on analysis of the chemical shift changes as a function of ENSA concentration (61, 62). This value was determined by titrating SDS-bound ENSA into SDS-bound AS. No interaction is detectable between the proteins in aqueous solution.

Relatively few proteins have been shown to interact specifically with the N-terminal domain of AS; our search of the research literature revealed only calmodulin (63), hDAT (64), synphilin (65), Aβ peptide (66), and PLD1 (67). Interactions with Aβ and PLD1 were lipid-independent. Of the other 3 proteins, only calmodulin has been characterized with respect to affinity and lipid-dependence. Calmodulin binds AS with K_d ~ 1 μM, and binds either free or membrane-bound AS. Interestingly, calmodulin binding causes AS to dissociate from the membrane.

The affinity of the AS-ENSA interaction (~61μM) is typical for regulatory interactions among proteins in signaling networks. Like AS, ENSA and ARPP-19 are intrinsically unstructured proteins (IUP's) ((68) (37). One characteristic of such proteins is that they can achieve highly specific binding with partner proteins via low affinity interactions, which is advantageous in functional contexts requiring multiple interacting partners on a timescale of coordinated biological processes (69). Such specific yet reversible binding events are critical for the proper functioning of protein signaling networks, which has been proposed to account for the association of IUP's with such networks. For example, several low-affinity binding interactions have been identified in the endocytic pathway (70); many of these interactions have K_d values on the order of 5 to 500 μM (69, 71). We envision a similar complexity of the interactions of AS with multiple partner proteins in accomplishing its biological functions.

3.7 Conclusion.

We present an important proof-of-principle that the N-terminus of AS can function as a membrane-dependent scaffold for interactions with other proteins. It is well established that membrane binding by AS is mediated by a series of imperfect 11-mer repeats at its N-terminus, spanning ~100 of a total of 140 residues (14, 36). The domain encompassing residues 1-102 is 92% identical among birds and mammals. In the presence of phospholipid vesicles, these repeats fold into an amphipathic helix that lies parallel to the membrane surface. In the absence of lipid, the repeat-containing domain has no stable structure (13).

The molecular significance of the extended, structurally plastic helical domain has so far been a mystery. A similar structural mechanism mediates lipid interactions by the exchangeable apolipoproteins, but these proteins are not as well conserved at the primary sequence level as AS (72, 73). We show here that the helical N-terminus of AS is capable of mediating specific interactions with other proteins. Because this helical structure is itself membrane-dependent and readily reversible, any protein complexes assembled around it should also be transient and sensitive to changes in the local membrane environment (e.g. via action of phospholipases or phospholipid kinases).

We therefore propose that the unique, plastic structure of AS subserves its function as a lipid-dependent protein scaffold. One consequence of this structural plasticity is that AS may continually cycle through unfolded or partially folded states, which could explain its particular propensity to self-associate into oligomers or fibrils, as observed in Parkinson's disease. In this context, lipid-dependent protein interactions might stabilize the folded structure of AS, decreasing its *in vivo* oligomeric potential. In such a scenario, PD-associated point mutations in the N-terminal domain (A30P, A53T, E46K) might promote misfolding of AS by disrupting

interactions with partner proteins. Further analysis of this novel class of AS-interacting proteins is warranted to assess the potential for dynamic participation of AS in signaling complexes at the membrane surface.

3.8 References

1. Polymeropoulos, M. H., Lavedan, C., Leroy, E., Ide, S. E., Dehejia, A., Dutra, A., Pike, B., Root, H., Rubenstein, J., Boyer, R., Stenroos, E. S., Chandrasekharappa, S., Athanassiadou, A., Papapetropoulos, T., Johnson, W. G., Lazzarini, A. M., Duvoisin, R. C., Di Iorio, G., Golbe, L. I. and Nussbaum, R. L. (1997) *Science* **276**, 2045-2047
2. Kruger, R., Kuhn, W., Muller, T., Woitalla, D., Graeber, M., Kosel, S., Przuntek, H., Epplen, J. T., Schols, L. and Riess, O. (1998) *Nat Genet* **18(2)**, 106-108
3. Zarranz, J. J., Alegre, J., Gomez-Esteban, J. C., Lezcano, E., Ros, R., Ampuero, I., Vidal, L., Hoenicka, J., Rodriguez, O., Atares, B., Llorens, V., Gomez Tortosa, E., del Ser, T., Munoz, D. G. and de Yebenes, J. G. (2004) *Ann Neurol* **55**, 164-173
4. Ibanez, P., Bonnet, A. M., Debarges, B., Lohmann, E., Tison, F., Pollak, P., Agid, Y., Durr, A. and Brice, A. (2004) *Lancet* **364**, 1169-1171
5. Chartier-Harlin, M. C., Kachergus, J., Roumier, C., Mouroux, V., Douay, X., Lincoln, S., Levecque, C., Larvor, L., Andrieux, J., Hulihan, M., Waucquier, N., Defebvre, L., Amouyel, P., Farrer, M. and Destee, A. (2004) *Lancet* **364**, 1167-1169
6. Spillantini, M. G., Crowther, R. A., Jakes, R., Hasegawa, M. and Goedert, M. (1998) *Proc Natl Acad Sci U S A* **95**, 6469-6473
7. Galvin, J. E., Lee, V. M. and Trojanowski, J. Q. (2001) *Arch Neurol* **58**, 186-190
8. Maroteaux, L., Campanelli, J. T. and Scheller, R. H. (1988) *J Neurosci* **8**, 2804-2815

9. Ueda, K., Fukushima, H., Masliah, E., Xia, Y., Iwai, A., Yoshimoto, M., Otero, D. A., Kondo, J., Ihara, Y. and Saitoh, T. (1993) *Proc Natl Acad Sci U S A* **90**, 11282-11286

10. George, J. M., Jin, H., Woods, W. S. and Clayton, D. F. (1995) *Neuron* **15**, 361-372

11. Abeliovich, A., Schmitz, Y., Farinas, I., Choi-Lundberg, D., Ho, W. H., Castillo, P. E., Shinsky, N., Verdugo, J. M., Armanini, M., Ryan, A., Hynes, M., Phillips, H., Sulzer, D. and Rosenthal, A. (2000) *Neuron* **25**, 239-252

12. Cabin, D. E., Shimazu, K., Murphy, D., Cole, N. B., Gottschalk, W., McIlwain, K. L., Orrison, B., Chen, A., Ellis, C. E., Paylor, R., Lu, B. and Nussbaum, R. L. (2002) *J Neurosci* **22**, 8797-8807

13. Davidson, W. S., Jonas, A., Clayton, D. F. and George, J. M. (1998) *J Biol Chem* **273**, 9443-9449

14. Perrin, R. J., Woods, W. S., Clayton, D. F. and George, J. M. (2000) *J Biol Chem* **275**, 34393-34398

15. Eliezer, D., Kutluay, E., Bussell, R., Jr. and Browne, G. (2001) *J Mol Biol* **307**, 1061-1073

16. Jao, C. C., Der-Sarkissian, A., Chen, J. and Langen, R. (2004) *Proc Natl Acad Sci U S A* **101**, 8331-8336

17. Barenholz, Y., Gibbes, D., Litman, B. J., Goll, J., Thompson, T. E. and Carlson, R. D. (1977) *Biochemistry* **16**, 2806-2810

18. Kloepper, K. D., Woods, W. S., Winter, K. A., George, J. M. and Rienstra, C. M. (2006) *Protein Expr Purif* **48**, 112-117

19. Delaglio, F., Grzesiek, S., Vuister, G. W., Zhu, G., Pfeifer, J. and Bax, A. (1995) *J Biomol NMR* **6**, 277-293

20. Goddard, T. D. and Kneller, D. G. (2005) **3.112**,

21. Bussell, R. J. and Eliezer, D. (2001) *J Biol Chem* **276**, 45996-46003

22. Chandra, S., Chen, X., Rizo, J., Jahn, R. and Sudhof, T. C. (2003) *J Biol Chem* **278**, 15313-15318

23. Payton, J. E., Perrin, R. J., Clayton, D. F. and George, J. M. (2001) *Brain Res Mol Brain Res* **95**, 138-145

24. Alim, M. A., Ma, Q. L., Takeda, K., Aizawa, T., Matsubara, M., Nakamura, M., Asada, A., Saito, T., Kaji, H., Yoshii, M., Hisanaga, S. and Ueda, K. (2004) *J Alzheimers Dis* **6**, 435-42; discussion 443-9

25. Spiliotis, E. T. and Nelson, W. J. (2006) *J Cell Sci* **119**, 4-10

26. Ihara, M., Tomimoto, H., Kitayama, H., Morioka, Y., Akiguchi, I., Shibasaki, H., Noda, M. and Kinoshita, M. (2003) *J Biol Chem* **278**, 24095-24102

27. Utton, M. A., Noble, W. J., Hill, J. E., Anderton, B. H. and Hanger, D. P. (2005) *J Cell Sci* **118**, 4645-4654

28. Elkon, H., Don, J., Melamed, E., Ziv, I., Shirvan, A. and Offen, D. (2002) *J Mol Neurosci* **18**, 229-238

29. Gerard, M., Debyser, Z., Desender, L., Kahle, P. J., Baert, J., Baekelandt, V. and Engelborghs, Y. (2006) *FASEB J* **20**, 524-526

30. Smith, W. W., Margolis, R. L., Li, X., Troncoso, J. C., Lee, M. K., Dawson, V. L., Dawson, T. M., Iwatsubo, T. and Ross, C. A. (2005) *J Neurosci* **25**, 5544-5552

31. Chen, L. and Feany, M. B. (2005) *Nat Neurosci* **8**, 657-663

32. Virsolvy-Vergine, A., Leray, H., Kuroki, S., Lupo, B., Dufour, M. and Bataille, D. (1992) *Proc Natl Acad Sci U S A* **89**, 6629-6633

33. Kim, S. H. and Lubec, G. (2001) *Neurosci Lett* **310**, 77-80

34. Kim, S. H. and Lubec, G. (2001) *J Neural Transm Suppl* 1-9

35. Bussell, R. and Eliezer, D. (2003) *J Mol Biol* **329**, 763-778

36. Ulmer, T. S., Bax, A., Cole, N. B. and Nussbaum, R. L. (2005) *J Biol Chem* **280**, 9595-9603

37. Boettcher, J. M., Hartman, K. L., Ladror, D. T., Qi, Z., Woods, W. S., George, J. M. and Rienstra, C. M. (in press) *Biomol NMR Assign*

38. Palmer, A. G., Williams, J. and A, M. (1996) *J Phys Chem* **100**, 13293-13310

39. Zuiderweg, E. R. (2002) *Biochemistry* **41**, 1-7

40. Pontius, J. U., Wanger, L. and Schuler, G. D. (2003) in *The NCBI handbook [Internet]* eds.) pp. Chapter 21, National Library of Medicine (US), National Center for Biotechnology Information, Bethesda (MD)

41. Thameem, F., Farook, V. S., Yang, X., Lee, Y. H., Permana, P. A., Bogardus, C. and Prochazka, M. (2004) *Mol Genet Metab* **81**, 16-21

42. Menegon, A., Bonanomi, D., Albertinazzi, C., Lotti, F., Ferrari, G., Kao, H. T., Benfenati, F., Baldelli, P. and Valtorta, F. (2006) *J Neurosci* **26**, 11670-11681

43. Hilfiker, S., Benfenati, F., Doussau, F., Nairn, A. C., Czernik, A. J., Augustine, G. J. and Greengard, P. (2005) *J Neurosci* **25**, 2658-2669

44. Hilfiker, S., Schweizer, F. E., Kao, H. T., Czernik, A. J., Greengard, P. and Augustine, G. J. (1998) *Nat Neurosci* **1**, 29-35

45. Goers, J., Manning-Bog, A. B., McCormack, A. L., Millett, I. S., Doniach, S., Di Monte, D. A., Uversky, V. N. and Fink, A. L. (2003) *Biochemistry* **42**, 8465-8471

46. Kontopoulos, E., Parvin, J. D. and Feany, M. B. (2006) *Hum Mol Genet*

47. Jiang, Y., Liu, Y. E., Goldberg, I. D. and Shi, Y. E. (2004) *Cancer Res* **64**, 4539-4546

48. Kweon, G. R., Marks, J. D., Krencik, R., Leung, E. H., Schumacker, P. T., Hyland, K. and Kang, U. J. (2004) *J Biol Chem* **279**, 51783-51792

49. Tieu, K., Perier, C., Caspersen, C., Teismann, P., Wu, D. C., Yan, S. D., Naini, A., Vila, M., Jackson-Lewis, V., Ramasamy, R. and Przedborski, S. (2003) *J Clin Invest* **112**, 892-901

50. Ved, R., Saha, S., Westlund, B., Perier, C., Burnam, L., Sluder, A., Hoener, M., Rodrigues, C. M., Alfonso, A., Steer, C., Liu, L., Przedborski, S. and Wolozin, B. (2005) *J Biol Chem* **280**, 42655-42668

51. Meyers, M. B., Puri, T. S., Chien, A. J., Gao, T., Hsu, P. H., Hosey, M. M. and Fishman, G. I. (1998) *J Biol Chem* **273**, 18930-18935

52. Naciff, J. M., Behbehani, M. M., Kaetzel, M. A. and Dedman, J. R. (1996) *Am J Physiol* **271**, C2004-15

53. Heron, L., Virsolvy, A., Peyrollier, K., Gribble, F. M., Le Cam, A., Ashcroft, F. M. and Bataille, D. (1998) *Proc Natl Acad Sci U S A* **95**, 8387-8391

54. Virsolvy, A., Smith, P., Bertrand, G., Gros, L., Heron, L., Salazar, G., Puech, R. and Bataille, D. (2002) *Br J Pharmacol* **135**, 1810-1818

55. Gros, L., Breant, B., Duchene, B., Leroy, C., Fauconnier, G., Bataille, D. and Virsolvy, A. (2002) *Diabetologia* **45**, 703-710

56. Dou, J., Cui, C., Dufour, F., Alkon, D. L. and Zhao, W. Q. (2003) *J Neurochem* **87**, 1086-1100

57. Ulmer, T. S. and Bax, A. (2005) *J Biol Chem* **280**, 43179-43187

58. Walaas, S. I., Nairn, A. C. and Greengard, P. (1983) *J Neurosci* **3**, 302-311

59. Dulubova, I., Horiuchi, A., Snyder, G. L., Girault, J. A., Czernik, A. J., Shao, L., Ramabhadran, R., Greengard, P. and Nairn, A. C. (2001) *J Neurochem* **77**, 229-238

60. Kim, S. H., Nairn, A. C., Cairns, N. and Lubec, G. (2001) *J Neural Transm Suppl* 263-272

61. Johnson, P. E., Tomme, P., Joshi, M. D. and McIntosh, L. P. (1996) *Biochemistry* **35**, 13895-13906

62. Labeikovsky, W., Eisenmesser, E. Z., Bosco, D. A. and Kern, D. (2007) *J Mol Biol* **367**, 1370-1381

63. Lee, D., Lee, S. Y., Lee, E. N., Chang, C. S. and Paik, S. R. (2002) *J Neurochem* **82**, 1007-1017

64. Lee, F. J., Liu, F., Pristupa, Z. B. and Niznik, H. B. (2001) *FASEB J* **15**, 916-926

65. Engelender, S., Kaminsky, Z., Guo, X., Sharp, A. H., Amaravi, R. K., Kleiderlein, J. J., Margolis, R. L., Troncoso, J. C., Lanahan, A. A., Worley, P. F., Dawson, V. L., Dawson, T. M. and Ross, C. A. (1999) *Nat Genet* **22**, 110-114

66. Jensen, P. H., Hojrup, P., Hager, H., Nielsen, M. S., Jacobsen, L., Olesen, O. F., Gliemann, J. and Jakes, R. (1997) *Biochem J* **323**, 539-546

67. Ahn, B. H., Rhim, H., Kim, S. Y., Sung, Y. M., Lee, M. Y., Choi, J. Y., Wolozin, B., Chang, J. S., Lee, Y. H., Kwon, T. K., Chung, K. C., Yoon, S. H., Hahn, S. J., Kim, M. S., Jo, Y. H. and Min do, S. (2002) *J Biol Chem* **277**, 12334-12342

68. Huang, H. B., Chen, Y. C., Horiuchi, A., Tsai, L. H., Liu, H. T., Chyan, C. L., Hsieh, M. J., Liu, C. K., Lin, F. M., Greengard, P., Nairn, A. C., Shiao, M. S. and Lin, T. H. (2001) *J Biomol NMR* **19**, 383-384

69. de Beer, T., Carter, R. E., Lobel-Rice, K. E., Sorkin, A. and Overduin, M. (1998) *Science* **281**, 1357-1360

70. Dafforn, T. R. and Smith, C. J. (2004) *EMBO Rep* **5**, 1046-1052

71. Miele, A. E., Watson, P. J., Evans, P. R., Traub, L. M. and Owen, D. J. (2004) *Nat Struct Mol Biol* **11**, 242-248

72. Clayton, D. F. and George, J. M. (1998) *Trends Neurosci* **21**, 249-254

73. Segrest, J. P., Jones, M. K., De Loof, H., Brouillette, C. G., Venkatachalapathi, Y. V. and Anantharamaiah, G. M. (1992) *J Lipid Res* **33**, 141-166

74. Pronin, A. N., Morris, A. J., Surguchov, A. and Benovic, J. L. (2000) *J Biol Chem* **275**, 26515-26522

75. Cavanagh, J., Fairbrother, W. J., Palmer, I. I. I., Arthur G., Rance, M. and Skelton, N. J. (2006) *Protein NMR Spectroscopy: Principles and Practice*, Academic Press, San Diego, CA

CHAPTER 4

^{1}H, ^{13}C and ^{15}N Resonance Assignment of the cAMP-regulated Phosphoprotein Endosulfine-Alpha in Free and Micelle-Bound States

4.1 Notes and Acknowledgements

This chapter was adapted from John M. Boettcher, Kevin L. Hartman, Daniel T. Ladror, Zhi Qi, Wendy S. Woods, Julia M. George, and Chad M. Rienstra, *Biomol. NMR Assign.* **2007**, *1*, 167-169. This work was supported by the University of Illinois (startup funds to C.M.R.) and the Research Corporation (Cottrell Scholars Award to C.M.R.).

4.2 Abstract

^{13}C, ^{15}N, and ^{1}H chemical shift assignments are presented for the cAMP-regulated phosphoprotein endosulfine-alpha in its free and micelle-bound states. Secondary chemical shift analysis demonstrates formation of four helices in the membrane-bound state, which are not present in the absence of membranes.

4.3 Biological context

Endosulfine alpha (ENSA) was originally identified as an endogenous regulator of ATP-sensitive potassium channels (K-ATP channels), which function as metabolic sensors in a variety of cell types, and are known to play a central role in the regulation of insulin secretion (*1*). K-ATP channels are the molecular targets of sulfonylurea drugs, a class of compounds used widely in the treatment of type II diabetes (*2*). Sulfonylureas bind to the sulfonylurea receptor (SUR) subunits of K-ATP channels in the pancreatic β cell membrane. The resulting inhibition of K^{+}

currents causes membrane depolarization and activation of voltage-gated Ca^{2+} channels, triggering insulin release.

Based on the identification of the SUR subunits as specific receptors for sulfonylurea drugs, the existence of endogenous ligands for these receptors was proposed, akin to the discovery of endorphins as endogenous ligands for opioid receptors (*3*). ENSA was thus purified from ovine brain in a biochemical screen for proteins that could compete with sulfonylurea drugs for binding to the K-ATP channel (*4*). Recombinant ENSA protein was shown to inhibit K+ currents in reconstituted pancreatic K-ATP channels, leading to the proposal that ENSA might regulate insulin secretion (*5*). The amino acid sequence of ENSA is highly similar to the cAMP-regulated phosphoproteins ARPP-16 and –19, which are all robust substrates for protein kinase A (PKA) phosphorylation (*6*).

There is no published structural data available for ENSA and its interactions have, so far, only been observed at low resolution. Here we report the backbone and side-chain resonance assignments of ENSA bound to sodium dodecyl sulfate (SDS) micelles and free in aqueous buffer. Second shift analysis demonstrate that ENSA undergoes a conformational change in the presence of lipid mimetics, forming four well-ordered helices.

4.4 Methods and experiments

4.4.1 Recombinant protein expression

For isotopically labeled ENSA, cultures were grown in M9 minimal media supplemented with 2 g [^{13}C]-glucose, 1 g [^{15}N]-ammonium chloride, 10 mg biotin, 10 mg thiamine and 10 ml [^{13}C, ^{15}N]-Bioexpress (Cambridge Isotopes Laboratories, Inc., Andover, MA). The ENSA construct was prepared in pET21 vector (Novagen). Protein expression was induced with IPTG at 30 ºC, followed by alkaline lysis, boiling, and precipitation with 60% ammonium sulfate.

Precipitates were resolubilized and purified by hydrophobic interaction chromatography on a HiPrep 16/10 Butyl Fast Flow Sepharose column (GE Biosciences), and eluted with decreasing salt. ENSA-containing fractions were pooled and concentrated, then subjected to high-resolution gel filtration chromatography (HiPrep 16/160 Sephacryl S-200, GE Biosciences).

4.4.2 NMR Spectroscopy

Solution NMR spectra were acquired at the VOICE NMR Facility (School of Chemical Sciences, University of Illinois at Urbana-Champaign) on a Varian INOVA 600 MHz spectrometer equipped with a 5 mm, triple resonance (1H-13C-15N) triaxial gradient probe, using VNMRJ version 2.1B with the BioPack suite of pulse programs released in early 2006. 2D 1H-15N HSQC spectra were measured for an average of two hours per spectrum, digitizing 512 points in the indirect 15N dimension (t1max = 232 ms). The standard suite of heteronuclear triple resonance 3D spectra (HNCO, HNCA, HNN, HNCACB, CBCA(CO)NH) was utilized to establish correlations among backbone resonances. Measurement times for the 3D spectra were 12 to 48 hours. Side chain ^{1}H resonances were assigned using HC(CO)NH, HCCH-TOCSY and NOESY-HSQC spectra.

Spectra were processed with NMRPipe (*7*) and analyzed in Sparky (*8*). The free state consisted of 0.5 mM ^{15}N, ^{13}C-labeled-ENSA in 50 mM phosphate buffer, pH 7.4, 10% D_2O. All subsequent SDS solutions were prepared using the same buffer (pH ~7.4) to minimize chemical shift perturbations due to changes in pH or ionic composition during titrations. The SDS micelle-bound state of ENSA was prepared by addition of 750 mM sodium dodecyl sulfate (SDS), with a final concentration of at least 70 mM, i.e., a 140:1 molar ratio of SDS to ENSA, beyond which no further changes in chemical shifts were observed. In all NMR experiments, the ^{15}N or ^{15}N, ^{13}C ENSA sample was filtered (0.2 mm) and first examined in the unfolded state by HSQC

experiments; immediately thereafter, SDS was added to prepare the bound state. Sample lifetime under these conditions typically ranged from five to seven days. HSQC spectra were acquired in between blocks of lengthier 3D experiments to confirm sample integrity. In SDS micelle-bound samples the concentration of SDS significantly exceeded its critical micelle concentration.

4.5 Extent of assignments and data deposition

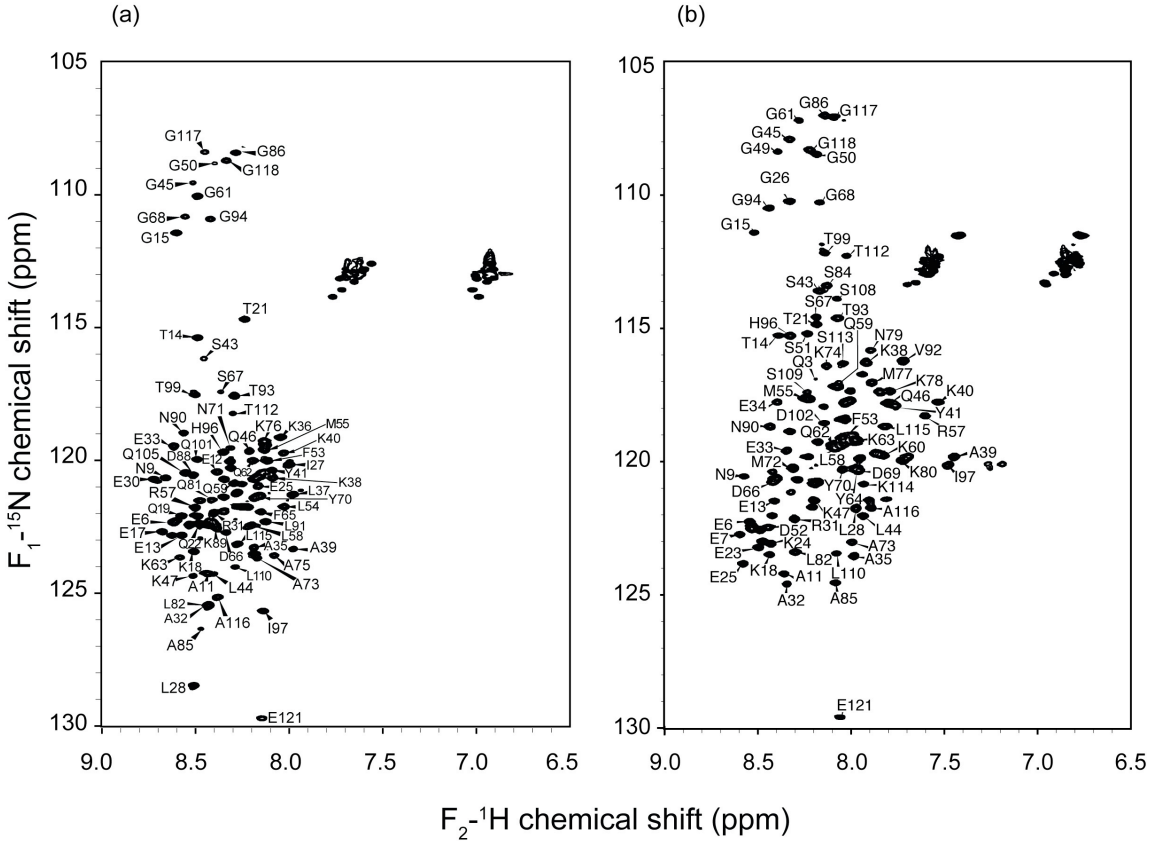

Figure 4.1 ^{15}N-^{1}H 2D HSQC NMR spectra of ENSA.

(a) ENSA free in aqueous buffer solution at 10 ºC; (b) bound to SDS micelles at 25 ºC. All the spectra were acquired with 4 scans per row, 512 rows, processed with sine bell apodization and zero filled in each dimension.

The 1H -15N HSQC spectrum for ENSA free in solution is shown in Figure 1. HN, N, Cα, C' and Cβ backbone assignments were performed (to ~91% completeness) with standard triple

resonance methods. No assignments were made or the first 3 residues (M1, S2, Q3) and the K4 assignments are tentative. The assignments were deposited in the BMRB under accession number 15136 (for release upon publication). The spectra demonstrate all the anticipated features of a predominantly unfolded protein, including minimal dispersion of 1H chemical shifts, rapid and strongly temperature-dependent exchange of most amide proton sites with water, and small secondary chemical shifts (*9*). At 10 °C, the 1H -15N HSQC spectrum (Figure 7.1a) contains 110 of the 112 expected peaks in the amide region (excluding 9 Pro residues). The dispersion of the amide peaks in the 1H dimension is only ~0.8 ppm, typical of proteins with minimal secondary structure. Moreover, compared to the spectrum acquired at 10 °C, the HSQC spectrum at 25 °C (data not shown) shows substantial decreases in signal intensities throughout the spectrum and prominent upfield shifts of most peaks, indicating rapid chemical exchange with water. Consensus chemical shift index (CSI) (*10*) analysis demonstrates that one short helix is present from residues 32 to 36, while other short stretches (e.g. 71 to 75) possess slight helical tendencies (i.e., although strictly random coil the population of helical conformations is likely higher than beta-sheet, based on the fractional secondary shifts). In addition, some residues show beta-sheet tendencies; these regions include a stretch of several near the N terminus (N9, A11, T14, E16), and several near or at the C terminus (I97, T99, V110, T111, S112, K113 and E121). These trends are modest and not indicative of well-ordered secondary structure, but residual secondary structure in a mostly unfolded protein. All other sites in ENSA (80% of the sequence) have unambiguous characteristics indicative of an unfolded protein.

The SDS micelle-bound state yielded essentially all of the expected cross peaks in this case despite the lack of 2H labeling. Figure 1b shows the 1H -15N HSQC spectrum of ENSA bound to SDS micelles at 25 °C. The quality of the data enabled nearly ~98% of HN, N, Cα, Cβ,

and C' resonance assignments. The majority of the proton and carbon side chain chemical shift assignments were performed using a combination of 3D spectra. Residues preceding proline residues (9 total) are missing C' assignments and no assignments were possible for the first residue (M1). The assignments were deposited in the BMRB under accession number 15135 (for release upon publication). CSI analysis (*10*) indicated an increase in the degree of helical structure throughout the protein. Semi-empirical analysis of the chemical shifts was also performed using the program TALOS (*11*). TALOS-reported ϕ and ψ backbone dihedral angles confirm the helical structures reported by CSI analysis. The first helix identified by chemical shift analysis extends from residue 34 to 39, whereas in the free state only a few residues in this region could confidently be identified as helical. The three new helices consist of residues 49 to 64, 68 to 78 and 106 to 113. The fourth helix, which includes the PKA phosphorylation site S109 (*5*), shows no secondary structure in the free state. Several residues retained beta sheet tendencies, as seen in the ENSA free in solution. This included stretches near the N terminus and several near the C terminus.

4.6 References

1. Nichols, C. G. (2006) K-ATP channels as molecular sensors of cellular metabolism. Nature 440, 470-476.
2. Ashcroft, S. J. H. (2000) The beta-cell K-ATP channel. J. Membr. Biol. 176, 187-206.
3. Lupo, B., and Bataille, D. (1987) A Binding-Site for [H-3] Glipizide in the Rat Cerebral-Cortex. Euro. J. Pharmacol. 140, 157-169.
4. Virsolvyvergine, A., Leray, H., Kuroki, S., Lupo, B., Dufour, M., and Bataille, D. (1992) Endosulfine, an Endogenous Peptidic Ligand for the Sulfonylurea Receptor - Purification

and Partial Characterization from Ovine Brain. Proc. Natl. Acad. Sci. U. S. A. 89, 6629-6633.

5. Heron, L., Virsolvy, A., Peyrollier, K., Gribble, F. M., Le Cam, A., Aschcroft, F. M., and Bataille, D. (1998) Human alpha endosulfine, a possible regulator of sulphonylurea-sensitive K-ATP channel. Diabetologia 41, A138-A138.

6. Peyrollier, K., Heron, L., LeCam, A., and Bataille, D. (1996) Alpha endosulfine is a novel molecule, structurally related to a family of phosphoproteins. Diabetologia 39, 893-893.

7. Delaglio, F., Grzesiek, S., Vuister, G. W., Zhu, G., Pfeifer, J., and Bax, A. (1995) NMRpipe - a Multidimensional Spectral Processing System Based on Unix Pipes. J. Biomol. NMR 6, 277-293.

8. Goddard, T. D., and Kneller, D. G. (2005), University of California, San Francisco.

9. Dyson, H. J., and Wright, P. E. (2004) Unfolded proteins and protein folding studied by NMR. Chem. Rev. 104, 3607-3622.

10. Wishart, D. S., and Sykes, B. D. (1994) The C-13 Chemical-Shift Index - a Simple Method for the Identification of Protein Secondary Structure Using C-13 Chemical-Shift Data. J. Biomol. NMR 4, 171-180.

11. Cornilescu, G., Delaglio, F., and Bax, A. (1999) Protein backbone angle restraints from searching a database for chemical shift and sequence homology. J. Biomol. NMR 13, 289-302.

CHAPTER 5

Membrane-Induced Folding of the cAMP-Regulated Phosphoprotein Endosulfine-Alpha

5.1 Notes and Acknowledgements

This chapter was adapted from John M. Boettcher, Kevin L. Hartman, Daniel T. Ladror, Zhi Qi, Wendy S, Woods, Julia M. George, and Chad M. Rienstra, Biochemistry. 2008, 47, 12357-12364. This work was supported by grants from the Research Corporation (Cottrell Scholars Award to CMR), the University of Illinois and the Branfman Family Foundation (to JMG)

5.2 Abstract

Endosulfine alpha (ENSA) is a 121-residue cAMP-regulated phosphoprotein, originally identified as an endogenous regulator of ATP-sensitive potassium channels. ENSA has been implicated in the regulation of insulin secretion, and expression of ENSA is decreased in brains of both Alzheimer's disease (AD) and Down's syndrome patients. We recently described membrane-dependent interactions between ENSA and the Parkinson's disease associated protein alpha-synuclein. Here we characterize the conformational change in ENSA that occurs upon binding to membranes. Secondary chemical shift analysis demonstrates formation of four helices in the lipid-bound state that are not present in the absence of lipid. The helical structure is maintained in several different lipid mimetics (sodium dodecyl sulfate, dodecyl phosphocholine, lyso 1-palmitoyl phosphatidylglycerol, and phospholipid vesicles). Introduction of a mutation (S109E) to mimic PKA phosphorylation of ENSA leads to a perturbation of the fourth helix and disrupts the interaction with alpha-synuclein. These data establish ENSA as an intrinsically

unstructured protein that adopts a stable structure upon membrane binding, properties it shares with its binding partner alpha-synuclein.

5.3 Introduction

Endosulfine alpha (ENSA) is a small cytosolic protein belonging to the cAMP-regulated phosphoprotein (ARPP) family (1). It was originally identified as an endogenous regulator of ATP-sensitive potassium channels (K-ATP channels), which function as metabolic sensors in a variety of cell types, where they couple secretory activity to the availability of ATP (2). K-ATP channels are the molecular targets of sulfonylurea drugs, a class of compounds used widely in the treatment of type II diabetes (3). Sulfonylureas bind to the sulfonylurea receptor (SUR) regulatory subunits of K-ATP channels in the pancreatic β cell membrane, leading to closure of the channel pore. The resulting inhibition of K+ currents causes membrane depolarization and activation of voltage-gated Ca^{2+} channels, triggering insulin release. These same channels mediate glucose-stimulated insulin secretion, as they are alternately inhibited and activated via binding of metabolically produced ATP or MgADP to the SUR subunits. In brain tissue, K-ATP channel closure is associated with neurotransmitter release (4).

Based on the identification of the SUR subunits as specific receptors for sulfonylurea drugs, the existence of endogenous ligands for these receptors was proposed, akin to the discovery of endorphins as endogenous ligands for opioid receptors (5). ENSA was thus purified from ovine brain in a biochemical screen for proteins that could compete with sulfonylurea drugs for binding to the K-ATP channel (6). Recombinant ENSA protein was shown to inhibit K+ currents in reconstituted pancreatic K-ATP channels, leading to the proposal that ENSA might regulate insulin secretion (7). Recent studies have failed to observe localization of ENSA to rat pancreatic β cells, raising some doubts regarding its proposed role in insulin secretion (8). However, other

reports have demonstrated regulation of ENSA expression by glucose in mesangial cells of the kidney (9), which also express K-ATP channels that are sensitive to sulfonylureas. Treatment of insulin-deficient rats with low doses of glibenclamide (to mimic the effects of increased ENSA expression) protected against the development of glomerulosclerosis, a typical complication of diabetes (10).

While the function of ENSA has not been analyzed in the brain, its expression varies significantly in several pathological and functional contexts. ENSA protein is greatly decreased in frontal cortex and cerebellum of Alzheimer's patients (11) and in Down's syndrome patients with Alzheimer's disease pathology (12). ENSA mRNA is down-regulated in rat hippocampus with long-term memory consolidation, but up-regulated with swimming-related stress (13). Recent studies suggest that modulation of K-ATP channel activity by oxidative stress contributes to the differential vulnerability of midbrain dopamine neurons to neurodegeneration in Parkinson's disease (14), but a potential role for ENSA in this process has not been considered.

We recently identified ENSA in a screen for conformation-dependent binding partners of alpha-synuclein (AS), an activity-dependent inhibitor of synaptic neurotransmission (15, 16) which is associated with both familial (17-21) and sporadic (22, 23) Parkinson's disease. The two proteins were found to interact only in the presence of SDS micelles or small unilamellar vesicles (24), conditions known to promote a dramatic conformational shift in AS from random coil to alpha helix (25). We speculate that ENSA and AS interact physiologically in a membrane-dependent fashion to regulate neuronal excitability and synaptic vesicle release. Here we use a combination of solution NMR, circular dichroism spectroscopy, and gel exclusion chromatography to characterize the structure of lipid-bound ENSA, and to investigate the potential effects of PKA phosphorylation on the lipid-dependent interactions of ENSA and AS.

5.4 Experimental Procedures

5.4.1 Recombinant protein expression.

For isotopically labeled protein, cultures were grown in M9 minimal media supplemented with 2 g [^{13}C]-glucose, 1 g [^{15}N]-ammonium chloride, 10 mg biotin, 10 mg thiamine and 10 ml [^{13}C, ^{15}N]-Bioexpress (Cambridge Isotopes Laboratories, Inc., Andover, MA). The wild type and S109E ENSA constructs were prepared in pET21 vector (Novagen). Protein expression was induced with IPTG at 30 ºC, followed by alkaline lysis, boiling, and precipitation with 60% ammonium sulfate. Precipitates were resolubilized and purified by hydrophobic interaction chromatography on a HiPrep 16/10 Butyl Fast Flow Sepharose column (GE Biosciences), and eluted with decreasing salt. ENSA-containing fractions were pooled and concentrated, then subjected to high-resolution gel filtration chromatography (HiPrep 16/160 Sephacryl S-200, GE Biosciences).

Full-length, untagged AS protein was produced for NMR experiments according to published procedures (26). Protein concentrations were determined spectrophotometrically by measuring absorbance at 280 nm assuming molar extinction coefficients of 4470 $M^{-1}cm^{-1}$ and 5200 $M^{-1}cm^{-1}$ for ENSA and AS respectively.

5.4.2 Circular Dichroism Spectroscopy

Circular dichroism spectra were acquired on a Jasco J720 Spectropolarimeter at room temperature. Spectra were taken on ENSA free in solution and in the presence of lyso 1-palmitoyl phosphatidylglycerol (LPPG), dodecyl phosphocholine (DPC), sodium dodecyl sulfate (SDS) and small unilamelar vesicles (SUV). In all samples ENSA was at a concentration of 15 μM. The concentration of LPPG, DPC and SDS was 20 mM. The concentration of the small unilamellar vesicles was 4 mg/ml.

5.4.3 NMR Spectroscopy

Solution NMR spectra were acquired at the NMR Facility (School of Chemical Sciences, University of Illinois at Urbana-Champaign) on a Varian INOVA 600 MHz spectrometer equipped with a 5 mm, triple resonance (^{1}H-^{13}C-^{15}N) triaxial gradient probe, using VNMRJ version 2.1B with the BioPack suite of pulse programs released in early 2006. 2D ^{1}H-^{15}N HSQC spectra were measured for an average of two hours per spectrum, digitizing 512 points in the indirect ^{15}N dimension (t1max = 232 ms). The standard suite of heteronuclear triple resonance 3D spectra (HNCO, HNCA, HNCACB, CBCA(CO)NH) was utilized to establish correlations among backbone resonances for the S109E sample. Measurement times for the 3D spectra were 12 to 48 hours. In all spectra, the direct 1H dimension was acquired over a ~15 ppm bandwidth with an acquisition time ($t_3$max) of at least 100 ms, using standard ^{15}N and ^{13}C decoupling methods. The HNCO spectrum was digitized with 64 points in the ^{13}C dimension and 48 points in the ^{15}N dimension ($t_1$max = 21 ms, $t_2$max = 22 ms). The HNCA spectrum was digitized with 64 points in the ^{15}N dimension and 48 points in the ^{15}N dimension ($t_1$max = 14 ms, $t_2$max = 22 ms). The HNCACB spectrum was digitized with 96 points in the ^{13}C dimension and 60 points in the ^{15}N dimension ($t_1$max = 8 ms, $t_2$max = 25 ms). The CBCA(CO)NH spectrum was digitized with 64 points in the ^{13}C dimension and 48 points in the ^{15}N dimension ($t_1$max = 5 ms, $t_2$max = 22 ms). Spectral widths were adjusted to cover the bandwidths of interest, using default parameters in the BioPack software. Steady-state heteronuclear {^{1}H}-^{15}N NOE experiments were acquired on ^{15}N-labeled ENSA. {^{1}H}-^{15}N NOE spectra were acquired for ENSA in the free (10 °C) and SDS micelle-bound (>140:1 SDS to ENSA ratio, 25 °C) states. This included one spectrum with proton saturation and one without saturation during a 5 s relaxation delay. The acquisition time for each spectrum was ~12 hours.

Spectra were processed with NMRPipe (27) and analyzed in Sparky (28). The free state consisted of 0.5 mM ^{15}N, ^{13}C-labeled-ENSA in 50 mM phosphate buffer, pH 7.4, 10% D_2O. All subsequent lipid mimetic solutions were prepared using the same buffer (pH ~7.4) to minimize chemical shifts due to changes in pH or ionic composition during titrations. The titrations were performed by the addition of the lipid mimetic solution directly to the NMR tube. The SDS micelle-bound state of ENSA was prepared by addition of 750 mM SDS in 4.6 ml aliquots, achieving a final concentration of at least 70 mM, i.e., a 140:1 molar ratio of SDS to ENSA. The LPPG micelle-bound state of ENSA was prepared by the addition of 120 mM LPPG solution in 40 μl aliquots, achieving a final concentration of at least 60 mM, a 120:1 molar ratio of LPPG to ENSA. DPC micelle-bound state of ENSA was prepared by the addition of 150 mM DPC solution in 29.5 μl aliquots, achieving a final concentration of at least 60 mM, a 120:1 molar ratio of DPC to ENSA. The SUV-bound ENSA sample started with a 0.15 mM ENSA sample, and a 54 mM SUV solution was added in 58.3 μL aliquots. The final concentration reached was 22 mM SUV concentration (250:1 SUV:ENSA molar ratio). The S109E mutant was prepared in the SDS micelle-bound state in the same manner as the wild type ENSA and following similar stoichiometry. For all NMR experiments, ENSA (wild type and S109E) was filtered (0.2 μm) and first examined in the unfolded state by HSQC experiments; immediately thereafter, lipid mimetic was added to prepare the bound state and additional HSQC experiments acquired to confirm the titration end point. During subsequent experiments and for spectra of the WT and S109E ENSA-AS interaction, natural abundance AS was titrated immediately thereafter to the SDS micelle-bound ENSA and followed the procedure previously described (24). Sample lifetime under these conditions typically ranged from five to seven days. HSQC spectra were acquired in between blocks of lengthier 3D experiments to confirm sample integrity. In all the

lipid-bound samples the concentration of lipid mimetic significantly exceeded its critical micelle concentration.

5.4.4 Vesicle Preparation

1-Palmitoyl 2-oleoyl phosphatidylcholine (POPC) and 1-palmitoyl 2-oleoyl phosphatidic acid (POPA) in chloroform were purchased from Avanti Polar Lipids (Alabaster, AL). A thin film of 3:1 POPC and POPA mixture was evenly applied to the inside of a round bottom flask under gentle N2 stream and then allowed to fully evaporate over at least half an hour. The dry lipids were resuspended in 3.5 ml low salt STB buffer (7.7 mM Tris, 50 mM NaCl, 10 mM EDTA, pH 7.4) per 60 mg lipids, followed by a 2-hour sonication in a Branson 2510 bath sonicator (Branson Ultrasonics, Danbury, CT) (29). The solution was ultracentrifuged at 55,000 rpm (~125,000 x g) in a TLA 100.3 rotor for 2 h at 25 °C according to a previous protocol (25). The top two-thirds of the solution at this stage contained a significant amount of multilamellar vesicles (MLVs), as confirmed by HPLC (30). Preparative-scale HPLC was impractical for preparation of quantities of SUVs required for NMR studies. Rather, centrifugation at 85,000 rpm (~300,000 g) for 2.5 hours separated SUVs from MLVs. To improve the yield of SUVs, the bottom one-third fraction was collected from several centrifuge tubes and sonicated for two hours (30).

5.5 Results

5.5.1 ENSA is an unfolded protein in solution and forms a helical structure in complex with lipid mimetics

Solution NMR was previously used to characterize the structure of ENSA in aqueous buffer and in the presence of sodium dodecyl sulfate (SDS) micelles (31). In the absence of SDS, the spectra demonstrated all the anticipated features of an unfolded protein, including minimal

dispersion of 1H chemical shifts (Figure 1A), rapid and strongly temperature-dependent exchange of most amide proton sites with water (Figure 1B) and small secondary chemical shifts (32). Consensus chemical shift index (CSI) (33) analysis concurred that ENSA is a predominantly unfolded protein in aqueous buffer, possessing secondary structure only in one short helix (residues 32 to 36). Heteronuclear ^{1}H-^{15}N NOE experiments revealed low order parameters throughout, consistent with this disordered state (data not shown). Closer examination of the secondary chemical shifts (Figure 2A) illustrates a small residual helicity among two other short stretches of residues.

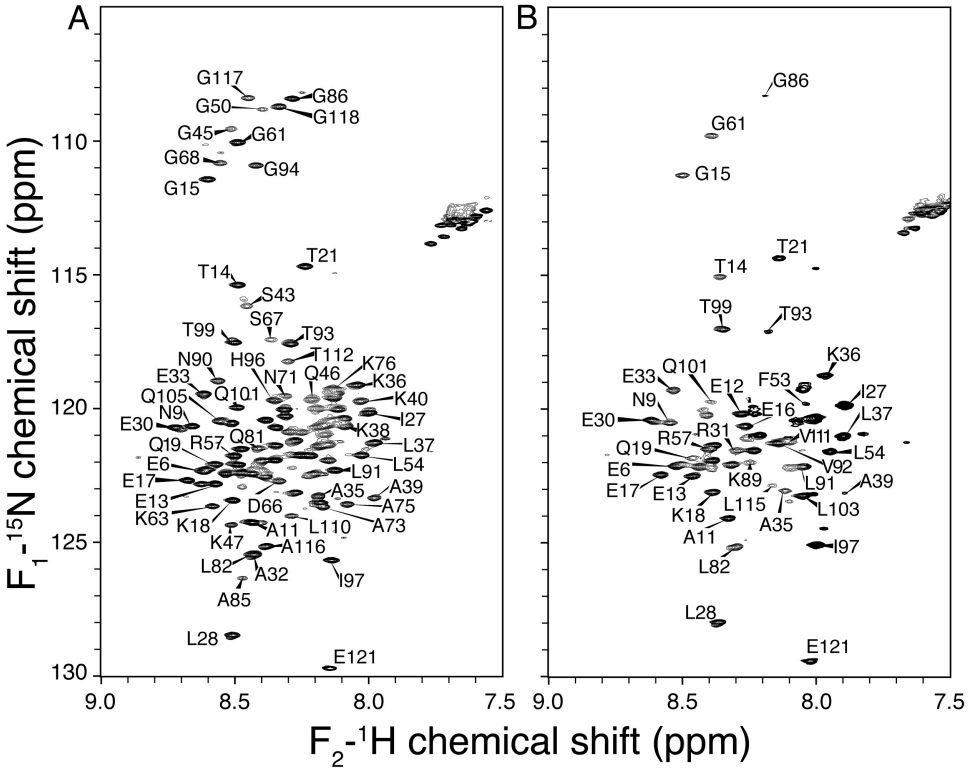

Figure 5.1 ^{15}N-^{1}H 2D HSQC NMR spectra of ENSA.

(A) Free (lacking detergent micelles) in solution at 10 ºC (modified with permission from Figure 1 of Ref. (31)); (B) free in solution at 25 ºC. All the spectra were acquired with 4 scans per row, 512 rows, processed with sine bell apodization and zero filled in each dimension. Additional experimental details are reported in the text.

In the presence of SDS, ENSA undergoes a prominent conformational change to a more helical structure (31). CSI and TALOS analysis (33, 34) indicated the formation of 4 helices, consisting of residues 34 to 39, 49 to 64, 68 to 78 and 106 to 114 (31). Secondary Cα chemical shifts (Figure 2B) further confirm the significance of the change. Heteronuclear ^{1}H-^{15}N NOE experiments in this case revealed strong steady-state enhancements for the region from residue 34 to 116; the terminal domains yielded weak negative NOE intensities, consistent with a lack of secondary structure. Within the ordered domain, highest NOE enhancements were observed for residue within the four helices (data not shown).

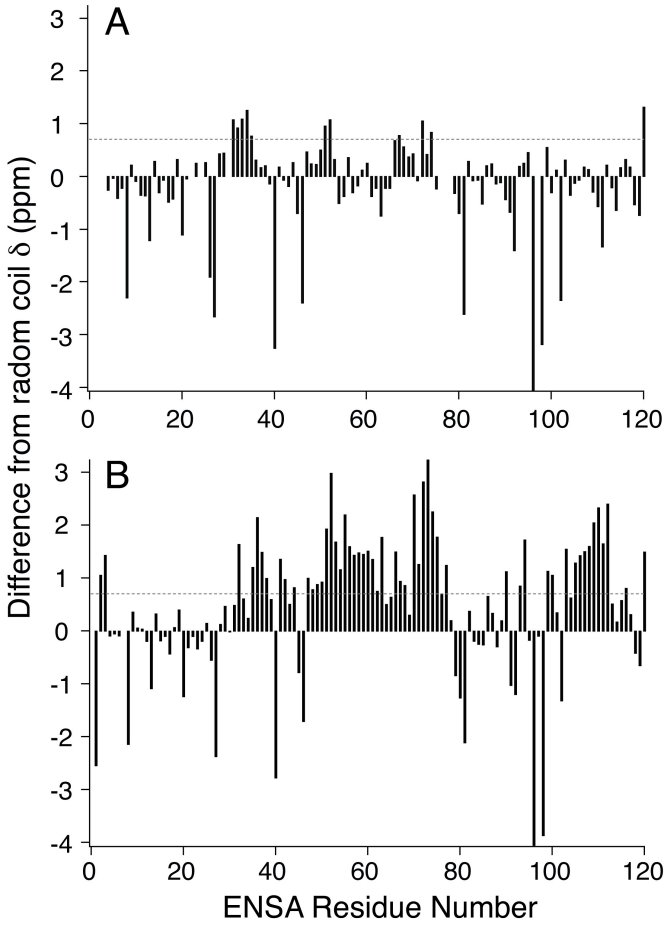

Figure 5.2 Secondary chemical shifts of α-carbons in ENSA.

Data are calculated as the deviation of the amino acid type-specific random coil value. Positive values indicate helical structure. (A) ENSA in aqueous buffer. (B) ENSA bound to SDS micelles.

5.5.2 Gel filtration chromatography confirms ENSA binding to phospholipid membranes

The observation that ENSA undergoes a conformational change in the presence of SDS micelles suggested that ENSA might also interact with phospholipid bilayers, a more physiologically relevant membrane environment. We incubated ENSA (0.1 mg/ml) with small unilamellar phospholipid vesicles (SUV, 2 mg/ml) prepared at a ratio of 3:1 POPC/POPA, and separated the mixture by gel filtration chromatography (Figure 3). Chromatograms of pure ENSA and pure SUV were acquired as controls. Pure ENSA eluted at ~19 ml. The pure SUV

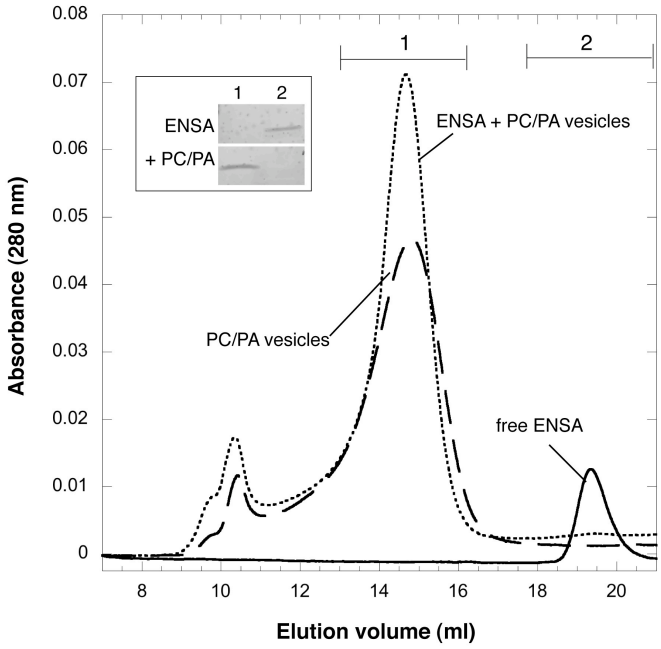

Figure 5.3 ENSA binds phospholipid vesicles.

Vesicles (2 mg/ml) prepared from a 3:1 mixture of POPC and POPA were incubated 10 minutes with recombinant ENSA protein (0.1 mg/ml), and the mixture was separated by gel filtration chromatography (…). For comparison, lipid-free ENSA protein (—) and pure vesicles (---) were subjected to similar separation. Pooled fractions (indicated by brackets) from the free ENSA and ENSA/lipid samples were separated by SDS-PAGE, stained with Coomassie blue, and visualized by scanning with the Odyssey infrared imaging system (inset). (Figure supplied by Wendy Woods and Dr. Julia George.)

solution eluted predominantly at 14.5 ml, with two smaller peaks (representing larger multilamellar vesicles) detected near 10 ml (25). Upon incubation with SUV, the free ENSA peak essentially disappeared, and the SUV peak increased in intensity, indicating binding of the

protein to the phospholipid vesicles. Integration of peak areas in the presence and absence of vesicles indicated that >80% of the protein bound under these conditions. The SUV peak also eluted at a slightly lower elution volume, indicating an increase in the hydrodynamic radius of the vesicles upon protein binding. The MLV peaks were also shifted slightly, suggesting that ENSA binds these larger vesicles as well. The inset to Figure 3 shows SDS-PAGE gel electrophoresis of pooled fractions representing the free protein peak (lane 2) and the SUV:ENSA peak (lane 1) to confirm the shift in ENSA elution time in the presence of SUV. These data confirm that ENSA binds phospholipid vesicles.

5.5.3 Far UV circular dichroism demonstrates conformational changes in the presence of lipid mimetic

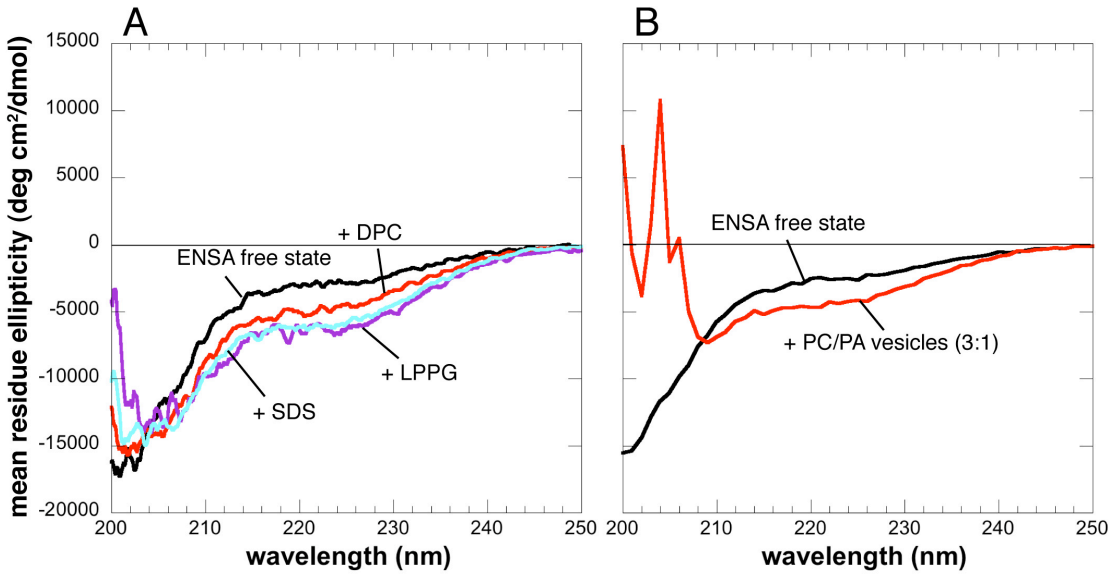

Figure 5.4 UV circular dichroism of ENSA.

Far UV circular dichroism spectra plotted with mean residue ellipticity [Θ] as a function of wavelength for (A) ENSA: free in solution (black), with excess SDS (light blue), with excess DPC (red), with excess LPPG (purple). (B) CD spectra of ENSA free in solution (black) and with excess SUV (red). (Figure supplied by Dr. Julia George.)

We next investigated the ENSA structure in complex with different membrane mimetics using far-UV circular dichroism (CD) spectroscopy, comparing the results to the SDS-induced structure. CD spectra were obtained for ENSA in the presence of micelles (SDS, dodecyl phosphocholine (DPC), or lyso 1-palmitoyl phosphatidylglycerol (LPPG)) and small unilamellar vesicles (SUV, 3:1 POPC/POPA). The CD spectra (Figure 4) agreed with the NMR analysis of SDS-bound ENSA, indicating little secondary structure for ENSA in the absence of lipid but significant increases in helical content in the presence of lipid mimetic; these structural elements are indicated by local minima at 208 and 222 nm (Figure 4). The CD spectra of ENSA in the presence of SDS and LPPG were very similar, indicating almost identical helical content for both, according to the intensity at 222 nm (35). The spectra obtained in the presence of DPC and SUV (Figure 4A,B) showed an increase in helical content over free ENSA, but less than in the presence of SDS or LPPG.

5.5.4 HSQC spectra demonstrate structural changes of ENSA in the presence of several lipid mimetics

The specific conformational events driving the association with membranes were examined further by solution NMR spectroscopy of ^{15}N-ENSA in complex with the lipid mimetics (SDS, LPPG, DPC, and SUV) used previously for the CD experiments (Figure 5). In all cases, significant changes in the HSQC spectra are observed as the lipid mimetic-to-protein ratio is increased. In the limit of excess lipid or detergent (molar ratio greater than 100:1 SDS:ENSA, LPPG:ENSA, and DPC:ENSA and greater than 200:1 SUV:ENSA) no further changes of statistical significance occur, indicating that ENSA exists in the lipid-bound state if provided a sufficient excess of lipid mimetic. The HSQC spectra obtained in the presence of SDS, LPPG and DPC at 25 °C (Figure 5A, B, C) demonstrate greater chemical shift dispersion than free

ENSA (~1.4 ppm for SDS and LPPG, ~1.1 ppm for DPC), consistent with an increase in secondary structure throughout the protein. Temperature-dependent chemical shift changes were also greatly reduced in the micelle-bound states, indicative of decreases in the accessibility of the protein to bulk water, as expected when the protein folds.

Initial assignments were made of the spectra by observing changes from the free state assignments and during the course of the titrations with lipid mimetics. In the presence of SUV, many of the ENSA resonances broaden and become depressed in intensity, leaving only ~35 of the expected 112 resonances (Figure 5D) in the HSQC spectrum in the presence of SUVs. This is approximately half the number seen for ENSA in solution at 25 °C. The resonances remaining were assigned to the N and C termini, which are unstructured in the SDS micelle-bound samples (31). Likewise, in the presence of DPC and LPPG, the same ~45 peaks appear in similar regions of the spectrum, and have chemical shifts consistent with random coil conformations. In addition to those signals that could be assigned straightforwardly, other resonances appeared at higher ratios of lipid to protein and therefore required de novo backbone assignment, which we performed for the SDS and LPPG bound states. The DPC spectra contained ~75 total peaks (excluding resonances associated with side chain amines) while both the SDS and LPPG spectra contained ~ 110 resonances.

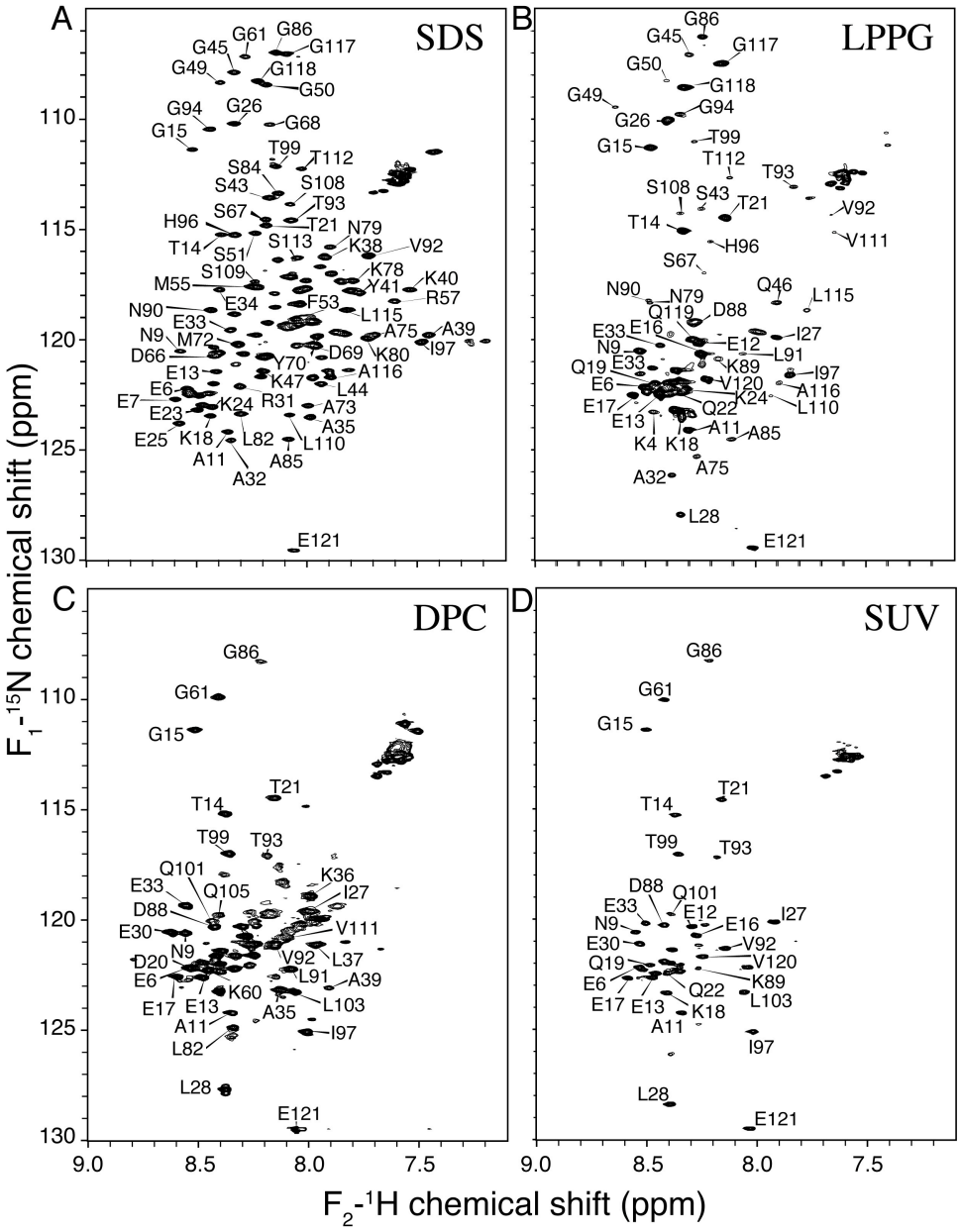

Figure 5.5 ^{15}N-^{1}H HSQC NMR spectrum of ENSA bound to membrane mimetics.

^{15}N-^{1}H HSQC NMR spectrum of (A) SDS micelle-bound ENSA (modified with permission from Figure 1 of Ref. (*31*)); (B) LPPG micelle-bound ENSA, (C) DPC micelle-bound ENSA and (D) ENSA bound to SUV. HSQC spectra were acquired as a function of lipid mimetic concentration to confirm the end point of the titration. An excess of lipid mimetic was employed for all subsequent experiments. Experimental and processing parameters are identical to those in Figure 1.

5.5.5 Assignment and structural interpretation of the LPPG micelle-bound ENSA NMR data

We have previously reported the assignments of the SDS micelle-bound sample (31). To validate the significance of this conformation to the physiology of ENSA, we have further investigated this behavior with lysophospholipids and vesicles. The LPPG micelle is a better approximation of physiological lipids than is SDS, and so it was of interest to assess whether ENSA assumes the same detailed structural properties in this context. Although the signals for the LPPG:ENSA complex were generally weaker and broader than the SDS micelle-bound ENSA (due to the larger size (~30 kDa) of the LPPG micelle) assignments were 80% complete. Resonances assigned to residues 6 to 30, 82 to 97 and 116 to 121 displayed high sensitivity and narrow line widths, which along with a lack of significant secondary shifts indicated that these regions of the protein are not directly bound to the micelle. Several other stretches of amino acids were assigned, despite depressed signal intensities, to regions within the same portions of the sequence that formed helices in the presence of SDS, and CSI analysis (33) for the assigned regions showed good agreement with the secondary structure domains observed in SDS. The helices found in the SDS micelle-bound sample are present in the LPPG micelle-bound sample, including the formation of a helix that contains S109, the site of phosphorylation by protein kinase A (PKA) (7).

Figure 5 also illustrates that signals assigned in ENSA bound to SUV are consistent with random coil conformation. Resonances from residues bound to the SUV (and in helical conformation, based upon the CD results) are broadened beyond detection; therefore assignments were possible only for regions where ENSA is not tightly bound to the vesicle. These regions of the protein agree well with the disordered ENSA residues in the SDS, DPC and LPPG complexes.

5.5.6 S109 phosphorylation affects the interaction of ENSA with membranes

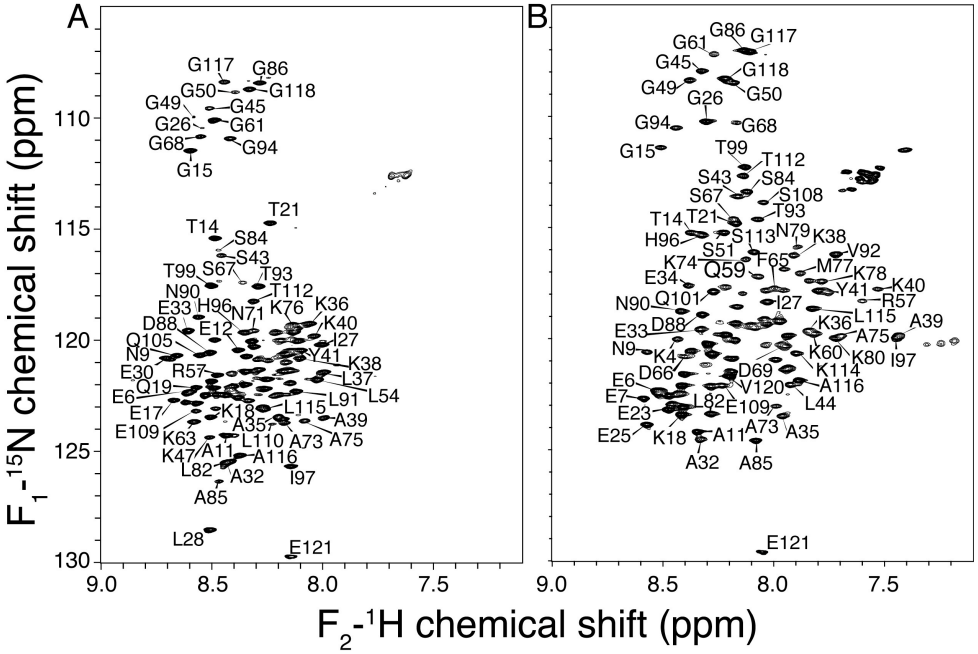

Figure 5.6 ^{15}N-^{1}H 2D HSQC NMR spectra of S109E-ENSA.

(A) ^{15}N-^{1}H 2D HSQC NMR spectra of S109E-ENSA Free (lacking detergent micelles) in solution at 10 ºC; (B) SDS micelle-bound S109E-ENSA at 25 ºC. Experimental and processing parameters are identical to those in Figure 1.

The results of the previous experiments indicate that ENSA undergoes a conformational change upon binding to membranes that includes the formation of the four helices reported previously for SDS (31). An interesting feature of the membrane-bound structure of ENSA is the formation of a helix that contains the site of phosphorylation (S109) by PKA (7). To examine the effect of phosphorylation on the structure of membrane-bound ENSA, we investigated a phosphorylation mutant, S109E, by NMR. Initially, HSQC spectra for S109E were obtained in the absence of membrane mimetic at 10 °C (pH 7.5, Figure 6A). The spectra were highly similar to wild type ENSA in solution and showed the same unstructured characteristics previously reported for wild type ENSA (31). Assignments for the S109E resonances in aqueous buffer therefore were presumed to be similar to the wild type ENSA assignments and confirmed

through a subset of 3D experiments. Regions showing significant chemical shift perturbations in the S109E mutant included not only the region near the mutation site, but also residues 30 to 40; this region contains the only element of secondary structure observed for ENSA in solution (31), a helix from residue 32 to 36.

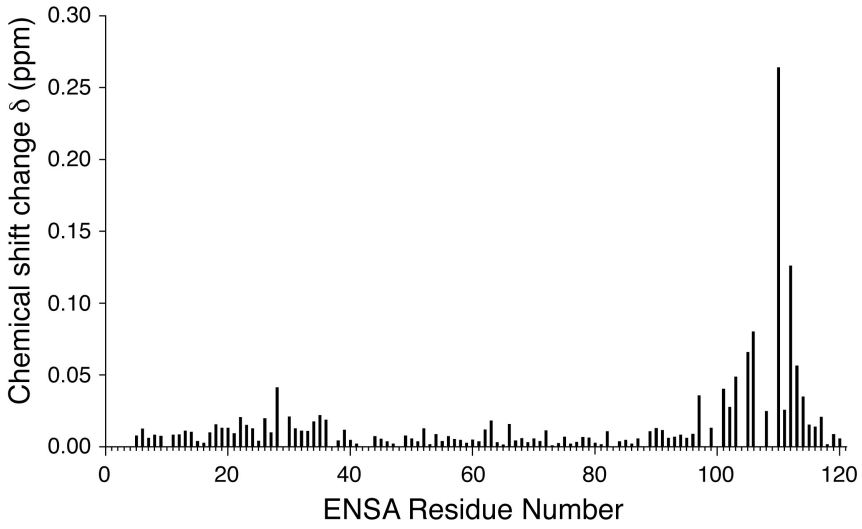

Figure 5.7 Chemical shift differences between wild type ENSA and the S109E mutant.

N and HN differences were calculated for the 107 assigned residues in the HSQC spectra using the formula $\delta = ([0.1\delta_N]^2 + \delta_H^2)^{1/2}$, where δ_N and δ_H are the respective changes in ^{15}N and ^{1}H chemical shifts in the units of ppm.

Next, NMR spectra were acquired on the S109E phosphorylation mutant of ENSA in the presence of saturating quantities of SDS (as confirmed by titrations as described above). HSQC (Figure 6B), HNCACB, HN(CO)CACB and HNCO spectra were acquired for the S109E micelle-bound sample and unambiguous assignments of CA, CB, CO, N and HN were obtained, from which the secondary structure could be inferred (33). The secondary structures are highly similar throughout the majority of the protein; however, the helix near the S109E mutation site is disrupted, containing only one helix turn (from residue 105 to 109) rather than three turns as observed in the wild type protein. Chemical shift perturbation analysis (Figure 7) confirms that

the only significant change in local conformation must occur near the C-terminus, although some of these conformational events may be allosterically transmitted to the short N-terminal helix. Most of these latter changes are on the order of 0.01 to 0.03 ppm, at the limit of significance for this experiment.

Previously, we used chemical shift perturbation mapping to explore the conformation dependence and structural specificity of the interaction of the neuronal protein α-synuclein (AS) and ENSA in the presence of SDS (24). Here we employ the same approach but with ^{15}N-labeled ENSA and natural abundance AS. The ENSA-AS interaction depends upon the helical conformation of each protein; therefore we examined the effect of titrating SDS-bound AS into a preformed solution of SDS-bound ENSA. The chemical shift perturbations in ENSA were continuous and approximately linear in AS concentration (Figure 8A). At a 1:1 molar ratio ENSA:AS, several ENSA residues show substantial changes in chemical shift (>0.03 ppm), including K4, Q5, several residues among L28 to E34, K89, G94, H96 and I97. Other residues showed smaller changes (0.01 to 0.03 ppm), while a majority of residues indicated no conformational change with differences in chemical shift within the expected error of the experiments (<0.01 ppm). We also performed chemical shift perturbation mapping with the ENSA S109E mutant (Figure 8B). In contrast to the wild type behavior, only four peaks are perturbed (L28, K63, Y64 and L103), at the borderline of statistical significance, indicative of a much weaker interaction between AS and the S109E ENSA mutant, as compared to wild type.

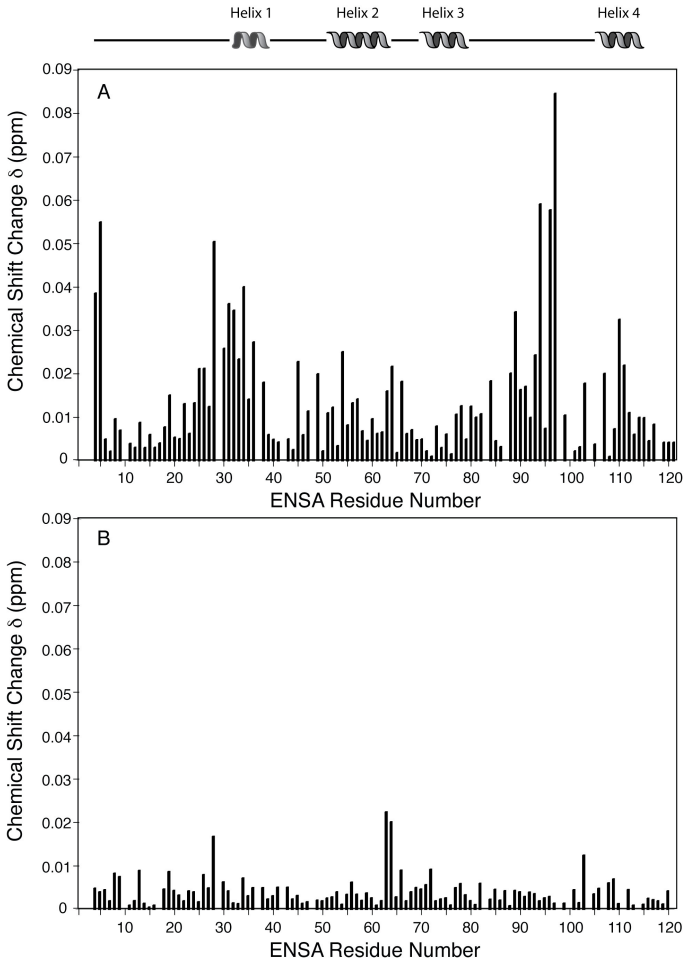

Figure 5.8 Chemical shift perturbations upon titration of ENSA with AS.

(A) Chemical shift changes upon interaction of micelle-bound wild type ENSA with AS. Chemical shift differences are reported as a function of residue number, where $\delta = ([0.1\delta_N]^2 + \delta_H^2)^{1/2}$ and δ_N and δ_H are the respective changes in ^{15}N and ^{1}H chemical shifts in the units of ppm. (B) Chemical shift changes upon interaction of micelle-bound S109E-ENSA with AS. Superimposed is a cartoon representation of the CSI predicted secondary structure for wild type membrane bound ENSA, with lines indicating random coil regions.

5.6 Discussion

5.6.1 ENSA forms a helical structure when bound to lipids

ENSA is a predominantly unfolded protein in aqueous solution with some nascent structure present. We find that ENSA undergoes a major structural rearrangement when bound to lipids such that the protein has well-defined secondary structure. We previously observed that residues ~30 to ~115 of ENSA, in the presence of SDS, adopt a helical structure (31). In the current

study, we demonstrate further that the binding is not SDS specific but that several lipid mimetics (DPC, LPPG and POPC/POPA SUVs) cause a similar conformational change. In all cases, increased helicity is observed in CD spectra (based upon ellipticity at 222 nm), which is confirmed by ^{1}H-^{15}N HSQC NMR spectra for the micelles. Furthermore, the ^{1}H-^{15}N HSQC spectra of ENSA in the presence of SUVs show strong signals for only the disordered termini and loops; residues bound tightly to the vesicle tumble too slowly for conventional solution NMR spectra to yield narrow resonance lines (residues 30 to 116). Thus the observed resonances in the spectra of SUV bound samples were assigned to the N and C termini, correlating well with the regions that are unstructured in both the SDS and LPPG bound samples. The remainder of the protein is, as expected from the other mimetics, helical. Thus all evidence consistently reports a secondary structure change throughout approximately one-third of the protein. Like ENSA, the homologous protein ARPP-19 (~87% sequence homology) was also reported to be largely unstructured in solution (36). Given the strong sequence similarity between ENSA and ARPP-19, it is likely that ARPP-19 undergoes a similar conformational change upon lipid binding.

5.6.2 The helical regions of lipid-bound ENSA are rich in basic residues

Like other peripheral membrane proteins (37), ENSA contains large numbers of positively charged residues and preferentially binds lipids that contain anionic head-groups. The four helices that form in the membrane-bound state correspond to regions of the protein rich in positively charged amino acids. For example, helix 1 contains residues K36 and K38; in addition, R31 and K40 are at either end of the helix. The second and third helixes are rich in basic residues (K56, R57, K60, K63, K74, K76, K78). Likewise, the fourth helix contains R106, K107 and K114.

The involvement of positively charged amino acids likely accounts for the higher affinity of ENSA for lipids with anionic head groups, as illustrated by comparison of the spectra in complex with anionic SDS and zwitterionic DPC micelle-bound ENSA. Both detergents have the same length side chain and form micelles of ~20 kDa. While CD data indicated that binding to both mimetics increased the helical content of ENSA, the SDS bound state showed a more robust change to helical conformation (Figure 4A), in agreement with data obtained for LPPG, also bearing an anionic head-group. In the NMR data, additional resonances were observed for the SDS micelle-bound sample (~110) than for the DPC bound sample (~75), and the resonances in the DPC-bound state were broader, which we attribute to intermediate exchange of the helices on and off the micelle.

5.6.3 PKA phosphorylation may regulate the ENSA-AS interaction

As previously shown (24), AS must be in a helical conformation in order to interact with ENSA, and here we have shown that ENSA also adopts a helical conformation as a prerequisite to AS binding. Here we extended upon this idea by evaluating the role of phosphorylation in ENSA-AS interactions. Phosphorylation is a common mechanism for regulation of protein-protein interactions, and it is known that PKA phosphorylates S109 of ENSA (7). Thus we investigated the S109E mutant, a mimic of phosphorylated ENSA, and found that the fourth helix was disrupted and interactions with AS were significantly attenuated. Chemical shift perturbation measurements indicated that the binding of AS to wild type ENSA primarily involves ENSA residues 28 to 36 and 88 to 97 (Figure 8), with smaller but still significant perturbations involving residues near S109. In contrast, no chemical shift perturbations of significance are observed in the S109E mutant of ENSA upon titration with AS.

5.6.4 Significance of lipid-binding to ENSA function

K-ATP channels are found at the plasma membrane and at intracellular membranes including the endoplasmic reticulum, secretory granules, and mitochondrial membranes (38). The SUR1 and SUR2 regulatory subunits of K-ATP channels are oriented toward the cytoplasmic membrane face, and sulfonylurea drugs are thought to exert their effects intracellularly after first crossing the plasma membrane (39). Likewise, ENSA is localized to the cytoplasm, where it is proposed to bind the SUR subunits and thereby modulate the K-ATP channel conductance (8, 9). Here we show that ENSA is also a lipid-binding protein, and that lipid interactions alter folding. We propose that the local membrane environment may regulate the interaction between ENSA and the SUR subunits of the K-ATP channel.

5.7 Conclusion

Here we have demonstrated that ENSA belongs to the class of intrinsically unstructured proteins (IUPs), which show little to no tertiary structure in isolation, but assume function in concert with a conformational change induced by interaction with target molecules. IUPs thereby exhibit biological properties that are not found in their highly structured counterparts. For example, IUPs can bind to multiple target molecules due to the plasticity of their structure (40). Induction of tertiary structure upon target binding can enhance specificity while keeping the binding affinity low (40), enabling interactions with multiple partners, and sometimes producing disparate physiological effects. Because of these properties, IUPs often display complex regulatory properties in signaling networks (41).

In the case of ENSA, published studies suggest a role in the regulation of K-ATP channels, which are central to the physiological regulation of insulin secretion (2). Other studies, including our own, implicate ENSA in brain physiology (13, 24), where its loss is associated with

neurodegeneration (11, 12). We propose that ENSA may participate in multiple physiological processes, involving multiple binding partners, by virtue of its intrinsic structural plasticity. ENSA may partner functionally with AS (also a lipid-stabilized IUP (25)) in neural tissue, to subserve a neural-specific function and yet also partner with other molecules in different cellular contexts. As with many other regulatory proteins, these interactions are modified by phosphorylation. The structural data reported here begin to clarify the importance of environmental effects on ENSA structure and will facilitate a better understanding of the role ENSA plays in diverse processes from insulin secretion to neurodegeneration.

5.8 Acknowledgements

We thank Kathryn Kloepper and Dr. Donghua Zhou for their help in the initial stages of this project, and we also acknowledge Dr. Zhou's assistance with vesicle preparation.

5.9 References

1. Peyrollier, K., Heron, L., Virsolvy-Vergine, A., LeCam, A., and Bataille, D. (1996) Alpha endosulfine is a novel molecule, structurally related to a family of phosphoproteins. Biochem. Biophys. Res. Comm. 223, 583-586.
2. Nichols, C. G. (2006) K-ATP channels as molecular sensors of cellular metabolism. Nature 440, 470-476.
3. Ashcroft, S. J. H. (2000) The beta-cell K-ATP channel. J. Membr. Biol. 176, 187-206.
4. Lee, K., Brownhill, V., and Richardson, P. J. (1997) Antidiabetic sulphonylureas stimulate acetylcholine release from striatal cholinergic interneurones through inhibition of K-ATP channel activity. J. Neurochem. 69, 1774-1776.
5. Lupo, B., and Bataille, D. (1987) A binding-Site for [3H] Glipizide in the Rat Cerebral-Cortex. Euro. J. Pharmacol. 140, 157-169.

6. Virsolvy-Vergine, A., Leray, H., Kuroki, S., Lupo, B., Dufour, M., and Bataille, D. (1992) Endosulfine, an endogenous peptidic ligand for the sulfonylurea receptor: purification and partial characterization from ovine brain. Proc. Natl. Acad. Sci. U. S. A. 89, 6629-6633.

7. Heron, L., Virsolvy, A., Peyrollier, K., Gribble, F. M., Le Cam, A., Aschcroft, F. M., and Bataille, D. (1998) Human alpha endosulfine, a possible regulator of sulphonylurea-sensitive K-ATP channel. Proc. Natl. Acad. Sci. U.S.A. 95, 8387-8391.

8. Gros, L., Breant, B., Duchene, B., Leroy, C., Fauconnier, G., Bataille, D., and Virsolvy, A. (2002) Localization of alpha-endosulfine in pancreatic somatostatin delta cells and expression during rat pancreas development. Diabetologia 45, 703-710.

9. Yee, J., Cortes, P., Barnes, J. L., Alviani, R., Biederman, J. I., and Szamosfalvi, B. (2004) Rat mesangial alpha-endosulfine. Kidney Int 65, 1731-9.

10. Biederman, J. I., Vera, E., Pankhaniya, R., Hasset, C., Giannico, G., Yee, J., and Cortes, P. (2005) Effects of sulfonylureas, alpha-endosulfine counterparts, on glomerulosclerosis in type 1 and type 2 models of diabetes (vol 67, pg 554, 2005). Kidney International 67, 1213-1213.

11. Kim, S. H., and Lubec, G. (2001) Brain alpha-endosulfine is manifold decreased in brains from patients with Alzheimer's disease: a tentative marker and drug target? Neurosci. Lett. 310, 77-80.

12. Kim, S. H., and Lubec, G. (2001) Decreased alpha-endosulfine, an endogenous regulator of ATP-sensitive potassium channels, in brains from adult Down syndrome patients. J. Neural Transm-Supp., 1-9.

13. Dou, J. T., Cui, C. H., Dufour, F., Alkon, D. L., and Zhao, W. Q. (2003) Gene expression of alpha-endosulfine in the rat brain: correlative changes with aging, learning and stress. J. Neurochem. 87, 1086-1100.

14. Liss, B., Haeckel, O., Wildmann, J., Miki, T., Seino, S., and Roeper, J. (2005) K-ATP channels promote the differential degeneration of dopaminergic midbrain neurons. Nat. Neurosci. 8, 1742-1751.

15. Cabin, D. E., Shimazu, K., Murphy, D., Cole, N. B., Gottschalk, W., McIlwain, K. L., Orrison, B., Chen, A., Ellis, C. E., Paylor, R., Lu, B., and Nussbaum, R. L. (2002) Synaptic vesicle depletion correlates with attenuated synaptic responses to prolonged repetitive stimulation in mice lacking alpha-synuclein. J. Neurosci. 22, 8797-8807.

16. Abeliovich, A., Schmitz, Y., Farinas, I., Choi-Lundberg, D., Ho, W. H., Castillo, P. E., Shinsky, N., Verdugo, J. M. G., Armanini, M., Ryan, A., Hynes, M., Phillips, H., Sulzer, D., and Rosenthal, A. (2000) Mice lacking alpha-synuclein display functional deficits in the nigrostriatal dopamine system. Neuron 25, 239-252.

17. Chartier-Harlin, M. C., Kachergus, J., Roumier, C., Mouroux, V., Douay, X., Lincoln, S., Levecque, C., Larvor, L., Andrieux, J., Hulihan, M., Waucquier, N., Defebvre, L., Amouyel, P., Farrer, M., and Destee, A. (2004) Alpha-synuclein locus duplication as a cause of familial Parkinson's disease. Lancet 364, 1167-1169.

18. Kruger, R., Kuhn, W., Muller, T., Woitalla, D., Graeber, M., Kosel, S., Przuntek, H., Epplen, J. T., Schols, L., and Riess, O. (1998) Ala30Pro mutation in the gene encoding alpha-synuclein in Parkinson's disease. Nat. Genet. 18, 106-108.

19. Polymeropoulos, M. H., Lavedan, C., Leroy, E., Ide, S. E., Dehejia, A., Dutra, A., Pike, B., Root, H., Rubenstein, J., Boyer, R., Stenroos, E. S., Chandrasekharappa, S.,

Athanassiadou, A., Papapetropoulos, T., Johnson, W. G., Lazzarini, A. M., Duvoisin, R. C., DiIorio, G., Golbe, L. I., and Nussbaum, R. L. (1997) Mutation in the alpha-synuclein gene identified in families with Parkinson's disease. Science 276, 2045-2047.

20. Singleton, A. B., Farrer, M., Johnson, J., Singleton, A., Hague, S., Kachergus, J., Hulihan, M., Peuralinna, T., Dutra, A., Nussbaum, R., Lincoln, S., Crawley, A., Hanson, M., Maraganore, D., Adler, C., Cookson, M. R., Muenter, M., Baptista, M., Miller, D., Blancato, J., Hardy, J., and Gwinn-Hardy, K. (2003) Alpha-synuclein locus triplication causes Parkinson's disease. Science 302, 841-841.

21. Zarranz, J. J., Alegre, J., Gomez-Esteban, J. C., Lezcano, E., Ros, R., Ampuero, I., Vidal, L., Hoenicka, J., Rodriguez, O., Atares, B., Llorens, V., Tortosa, E. G., del Ser, T., Munoz, D. G., and de Yebenes, J. G. (2004) The new mutation, E46K, of alpha-synuclein causes Parkinson and Lewy body dementia. Ann. Neurol. 55, 164-173.

22. Spillantini, M. G., Schmidt, M. L., Lee, V. M. Y., Trojanowski, J. Q., Jakes, R., and Goedert, M. (1997) Alpha-synuclein in Lewy bodies. Nature 388, 839-840.

23. Irizarry, M. C., Growdon, W., Gomez-Isla, T., Newell, K., George, J. M., Clayton, D. F., and Hyman, B. T. (1998) Nigral and cortical Lewy bodies and dystrophic nigral neurites in Parkinson's disease and cortical Lewy body disease contain alpha-synuclein immunoreactivity. J. Neuropath. Exp. Neur. 57, 334-337.

24. Woods, W. S., Boettcher, J. M., Zhou, D. H., Kloepper, K. D., Hartman, K. L., Ladror, D. T., Qi, Z., Rienstra, C. M., and George, J. M. (2007) Conformation-specific binding of alpha-synuclein to novel protein partners detected by phage display and NMR spectroscopy. J. Biol. Chem. 282, 34555-34567.

25. Davidson, W. S., Jonas, A., Clayton, D. F., and George, J. M. (1998) Stabilization of alpha-synuclein secondary structure upon binding to synthetic membranes. J. Biol. Chem. 273, 9443-9449.

26. Kloepper, K. D., Woods, W. S., Winter, K. A., George, J. M., and Rienstra, C. M. (2006) Preparation of alpha-synuclein fibrils for solid-state NMR: Expression, purification, and incubation of wild-type and mutant forms. Protein Expres. Purif. 48, 112-117.

27. Delaglio, F., Grzesiek, S., Vuister, G. W., Zhu, G., Pfeifer, J., and Bax, A. (1995) NMRPipe: a Multidimensional Spectral Processing System Based On Unix Pipes. J. Biomol. NMR 6, 277-293.

28. Goddard, T. D., and Kneller, D. G. (2005), University of California, San Francisco.

29. Barenholz, Y., Gibbes, D., Litman, B. J., Goll, J., Thompson, T. E., and Carlson, R. D. (1977) A simple method for the preparation of homogeneous phospholipid vesicles. Biochemistry 16, 2806-10.

30. Huang, C.-h. (1969) Studies on Phosphatidylcholine Vesicles. Formation and Physical Characteristics. Biochemistry 8, 344-352.

31. Boettcher, J. M., Hartman, K. L., Ladror, D. T., Qi, Z., Woods, W. S., George, J. M., and Rienstra, C. M. (2007) ^{1}H, ^{13}C and ^{15}N resonance assignment of the cAMP-regulated phosphoprotein endosulfine-alpha in free and micelle-bound states. Biomol. NMR Assign. 1, 167-169.

32. Dyson, H. J., and Wright, P. E. (2004) Unfolded proteins and protein folding studied by NMR. Chem. Rev. 104, 3607-3622.

33. Wishart, D. S., and Sykes, B. D. (1994) The ^{13}C Chemical-Shift Index: a Simple Method for the Identification of Protein Secondary Structure Using ^{13}C Chemical-Shift Data. J. Biomol. NMR 4, 171-180.

34. Cornilescu, G., Delaglio, F., and Bax, A. (1999) Protein backbone angle restraints from searching a database for chemical shift and sequence homology. J. Biomol. NMR 13, 289-302.

35. Rohl, C. A., and Baldwin, R. L. (1997) Comparison of NH exchange and circular dichroism as techniques for measuring the parameters of the helix-coil transition in peptides. Biochemistry 36, 8435-8442.

36. Huang, H. B., Chen, Y. C., Horiuchi, A., Tsai, L. H., Liu, H. T., Chyan, C. L., Hsieh, M. J., Liu, C. K., Lin, F. M., Greengard, P., Nairn, A. C., Shiao, M. S., and Lin, T. H. (2001) Letter to the Editor: Backbone ^{1}H, ^{15}N, and ^{13}C resonance assignments of ARPP-19. J. Biomol. NMR 19, 383-384.

37. Sankaram, M. B., and Marsh, D. (1993) Protein-lipid interactions with peripheral membrane proteins, in Protein-Lipid interactions (Watts, A., Ed.) pp 127-158, Elsevier.

38. Quesada, I., and Soria, B. (2004) Intracellular location of KATP channels and sulphonylurea receptors in the pancreatic beta-cell: new targets for oral antidiabetic agents. Curr Med Chem 11, 2707-16.

39. Schwanstecher, M., Schwanstecher, C., Dickel, C., Chudziak, F., Moshiri, A., and Panten, U. (1994) Location of the sulphonylurea receptor at the cytoplasmic face of the beta-cell membrane. Br J Pharmacol 113, 903-11.

40. Wright, P. E., and Dyson, H. J. (1999) Intrinsically unstructured proteins: Re-assessing the protein structure-function paradigm. J. Mol. Biol. 293, 321-331.

41. Tompa, P., Szasz, C., and Buday, L. (2005) Structural disorder throws new light on moonlighting. Trends Biochem. Sci. 30, 484-489.

CHAPTER 6

Calcium-induced clustering of phosphatidylserine in mixed lipid bilayers observed by SSNMR

6.1 Notes and Acknowledgements

This chapter was adapted from John M. Boettcher, Rebecca Davis-Harrison, Mary Clay, Andrew J. Nieuwkoop, James H. Morrissey, and Chad M. Rienstra (manuscript in preparation). This work was supported by the National Institute of General Medical Sciences, NIH (R01 HL47014), the National Heart Lung and Blood Institute, NIH (HL47014 to J.H.M.), and by the American Heart Association (0920045G to R.D.H.).

6.2 Abstract

Membranes play key regulatory roles in biological processes, with bilayer composition exerting marked effects on binding affinities and catalytic activities of a number of membrane-associated proteins. In particular, proteins involved in diverse processes such as vesicle fusion, intracellular signaling cascades and blood coagulation interact specifically with anionic lipids like phosphatidylserine in the presence of calcium ions. Calcium is known to induce clustering of phosphatidylserine in mixed phospholipid bilayers, yet little is known about the roles of phospholipid clustering or headgroup conformation in these important biological processes. In this study, we used magic angle spinning (MAS) solid-state NMR (SSNMR) to obtain site-resolved insights into the structure of lipid bilayers containing isotopically labeled serine headgroups in the context of mixed phosphatidylserine-phosphatidylcholine membranes. Here we report on Ca^{2+}-induced conformational changes of phosphatidylserine in mixed bilayers using

both liposomes and Nanodiscs, a nanoscale membrane-mimetic. Site-resolved multidimensional correlation SSNMR spectra of bilayers containing ^{13}C, ^{15}N-labeled phosphatidylserine demonstrate that Ca^{2+} ions promote the stabilization of two major phosphatidylserine headgroup conformations, which are well resolved in 2D ^{13}C-^{13}C, ^{15}N-^{13}C and ^{31}P-^{13}C spectra. The data shows these two conformations are within 6 Å of each other. Results also show the effect that Ca^{2+}-PS interactions have on lipid dynamics and bulk properties of nanometer-scale bilayers.

6.3 Introduction

A wide variety of biological processes take place on membrane surfaces, and many of these are mediated by Ca^{2+}-dependent interactions with anionic phospholipids like phosphatidylserine (PS[1]). Calcium ions can play various roles in these membrane-associated processes, including binding of Ca^{2+} to proteins (enhancing their ability to interact with the membrane surfaces) and/or the bilayer itself (altering the membrane surface presented for protein binding). As an example, Ca^{2+}-triggered vesicle fusion is coupled to Ca^{2+}-dependent synaptotagmin binding to PS in the bilayer. Synaptotagmin-1 binds Ca^{2+} ions with low affinity in its two C2 domains (*1*), but the Ca^{2+}-binding site is completed by interactions with PS, thus enhancing Ca^{2+} affinity and promoting protein-membrane interactions (*2*). The presence of PS in liposomes is required for synaptotagmin C2 domains to confer Ca^{2+} stimulation on SNARE-dependent liposome fusion (*3*). It has also been suggested that Ca^{2+} plays an additional role in membrane fusion by directly interacting with the headgroups of membrane phospholipids, thus bridging the two opposing bilayers (*4-6*). Another example is protein kinase C (PKCα), a ubiquitous signaling protein that binds preferentially, via its C2 domain, to membranes containing PS and phosphatidylinositol-4,5-bisphosphate (PIP_2). While the PIP_2 binding site has no direct interactions with Ca^{2+}, PS interacts directly with two ligated Ca^{2+} ions in the C2 domain (*7-9*). In the absence of Ca^{2+}

and/or PS, PKCα does not bind plasma membranes and therefore cannot readily interact with and phosphorylate its membrane-embedded protein targets.

Other examples include several serine proteases in the blood clotting systems that bind, via their γ-carboxyglutamate rich (GLA) domains, to PS-containing membranes in a Ca^{2+}-dependent manner (*10-13*). This binding interaction enhances the enzymatic activities of blood clotting proteases by many thousand-fold (*10, 14*). The Ca^{2+}-dependent association of GLA domains with PS-containing membranes is thought to be mediated, at least in part, via coordination of Ca^{2+} ions between negatively charged GLA residues and PS headgroups (*15-17*).

It has also been shown that membrane-binding proteins and plasma Ca^{2+} concentrations can induce clustering of PS into membrane microdomains (*18, 19*), which may act as target regions to enhance activities such as cell signaling and blood coagulation. Structures of PS headgroups exist only for samples in the absence of Ca^{2+} (*20*), although previous NMR studies have shown that Ca^{2+}-PS interactions in mixed bilayers cause conformational changes in PS headgroups (*21, 22*) a detailed molecular picture of exactly how Ca^{2+} ions interact with PS molecules at a membrane surface has yet to emerge. An understanding of how Ca^{2+} ions affect PS-containing lipid bilayers is an important step toward elucidating the molecular details of a variety of Ca^{2+}-dependent protein-membrane complexes.

In this study, we investigate the interactions of Ca^{2+} with PS-containing lipid bilayers using magic angle spinning (MAS) solid-state NMR (SSNMR) studies that employ two membrane mimetics, liposomes and Nanodiscs. Nanodiscs are discoidal phospholipid bilayers of 8 nm-diameter containing ~67 lipids per leaflet which are wrapped and stabilized by two molecules of an amphipathic helical protein termed membrane scaffold protein (MSP) (*23-26*). There are several examples in the literature that have effectively used the Nanodisc system as a membrane

mimetic in membrane protein interactions (*16, 27*) and SSNMR studies of membrane protein structures (*28-30*). One advantage of the Nanodisc system is that the structural integrity of the Nanodiscs persists with up to 90% PS in the bilayer, as opposed to liposomes which cannot tolerate more than 40% PS in the presence of Ca^{2+}. For these reasons, this system is the ideal experimental platform for investigating Ca^{2+}-PS interactions on a membrane surface by SSNMR.

In the present study, the serine headgroup of PS has been isotopically labeled and incorporated into the lipid bilayers, allowing for high resolution NMR spectra of PS headgroup moieties interacting with Ca^{2+} ions. Our results indicate that Ca^{2+} ions promote the formation of a liquid-ordered phase, producing rigid conformations for PS headgroups. Mobility of the lipid acyl chains are not as affected by interactions with Ca^{2+} ions as the headgroups, although alteration of the phase transition behavior of the bilayer by Ca^{2+}-PS interactions is shown. Furthermore, we report carbon, nitrogen and phosphorous chemical shift values for two Ca^{2+}-induced PS conformations as well as intermolecular distances between the two PS conformations in the bilayer. These observations are consistent with Ca^{2+}-induced clustering of membrane-incorporated PS molecules.

6.4 Experimental Procedures

6.4.1 Isotopically Labeled POPS

In a modification of the method of Iwasaki, *et al*. (*31*), phospholipase D from *Streptomyces* (PLD; Sigma-Aldrich, St. Louis, MO) was used to replace the choline headgroup of POPC (1-palmitoyl-2-oleoyl-phosphatidylcholine) with U-^{13}C, ^{15}N-L-serine (Cambridge Isotopes Laboratories, Andover, MA) to yield POPS (1-palmitoyl-2-oleoyl-phosphatidylserine) that was isotopically labeled in the serine headgroup (termed POPS*). Briefly, 5 μg/mL PLD was added, with stirring, to a mixture of 1.5 M ^{13}C, ^{15}N-serine, 36 mg/mL POPC (Avanti Polar Lipids,

Alabaster, AL) and $CaSO_4$ in 50 mM sodium acetate buffer, pH 5.6, and allowed to react overnight at 42 °C. The supernatant was collected by centrifugation, flushed with nitrogen gas and stored at 4 °C for use in subsequent reactions. The pellet was washed with water and re-suspended in 2:1 hexane:ethanol (5 mL per 1 mL original reaction volume), followed by water (1/4 the volume of hexane:ethanol) and 1 N HCl (1/10 the volume of the water). After vortexing, the hexane phase was collected, and the aqueous phase and pellet were extracted with additional hexane. The pooled hexane phases were dried under vacuum and POPS* was purified by CM52 chromatography (*32*). Purity of POPS* was evaluated by two-dimensional thin-layer chromatography, using 90:54 chloroform:methanol for the first dimension and 65:25:4 chloroform:methanol:water for the second dimension. When necessary, POPS* was further purified by flash silica chromatography developed with 90:40:12:2 chloroform:methanol:acetic acid:water. Purified POPS* was stored in chloroform and its concentration determined by inorganic phosphate analysis after complete hydrolysis. POPS* purity and the level of ^{13}C, ^{15}N-serine incorporation was verified by HSQC solution NMR in chloroform.

6.4.2 Nanodisc Preparation

Nanodiscs were prepared as previously described (*25*) using mixtures of POPC and POPS*. Briefly, dried phospholipids were suspended in Tris buffer containing a 2:1 molar ratio of deoxycholate:phospholipid and the mixture was sonicated. MSP was added at a 67:1 molar ratio of lipid:MSP and incubated for 1-2 hours, after which detergent was removed using SM-2 Absorbent Bio-Beads (BioRad, Hercules, CA) to allow Nanodisc self-assembly. Nanodiscs were purified by size-exclusion chromatography (*25*), except that the buffer was 10 mM Tris-HCl pH 7.4, 10 mM NaCl, with 2 mM $CaCl_2$. Samples were concentrated by centrifuging at 3000g in a Amicon Ultra 10000 NMWL centrifugal filter (Thermo Fisher Scientific, Waltham, MA) to 2-3

mM phospholipid (15-22 μM Nanodiscs), and the lyoprotectant, trehalose, was added in a 1:1 molar ratio to phospholipid. Samples were lyophilized and the powders (~50% Nanodiscs by weight) were packed into 3.2 mm SSNMR rotors, after which water was added (equal to ~50% of the dry weight of packed samples).

6.4.3 Liposome Preparation

Mixtures of dried POPC and POPS* (10 mg total) were suspended in 30 μL of 50 mM Tris-HCl pH 7.4, 100 mM NaCl, 2.5 mM $CaCl_2$ and sonicated until the solution was visually homogeneous, after which 1 mL of 2.5 mM $CaCl_2$ was added and the solution was sonicated again. Preparations of samples in the absence of Ca^{2+} were identical except for the inclusion or addition of $CaCl_2$. Liposomes were collected by ultracentrifugation at 4 °C for 2.5 hours at 250,000 rcf, and the pelleted liposomes were packed into 3.2 mm SSNMR rotors.

6.4.4 Solid-State NMR

SSNMR studies were performed on four-channel Varian InfinityPlus spectrometers. POPS*:POPC Nanodiscs spectra were acquired at 600 MHz with a Varian T3 ^{1}H-^{13}C-^{15}N 3.2 mm probe at an MAS rate of 10,000±3 Hz. The variable temperature gas was maintained at 90±10 scfh flow, and the reported sample temperatures take into account thermocouple calibration and frictional heating due to MAS, as calibrated with ethylene glycol (*33*). All experiments utilized tangent ramped cross polarization (CP) (*34*) with TPPM (*35*) decoupling of the protons applied during acquisition and evolution periods on average at ~80 kHz. Data were processed with NMRPipe (*36*) with back linear prediction and polynomial baseline (frequency domain) correction applied to the direct dimension, and zero filling and Lorentzian-to-Gaussian apodization applied to each dimension before Fourier transformation; additional processing

parameters are located in the figure captions. Chemical shifts are referenced to adamantane (*37*). Peak picking and assignments were performed with Sparky (*38*).

6.5 Results

6.5.1 Effects of Ca^{2+} binding on ^{13}C chemical shifts

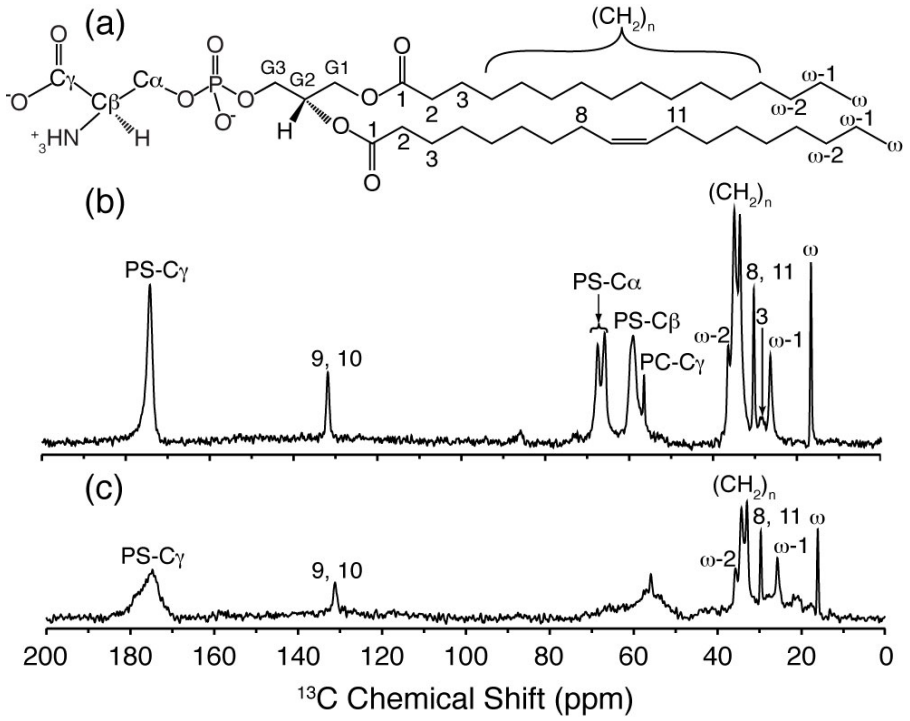

Figure 6.1 One-dimensional ^{13}C spectra of POPS*:POPC liposomes.

(a) POPS structure is shown with ^{13}C One-dimensional spectra of 30% POPS* 70% POPC liposomes (b) with 2 mM Ca^{2+}, and (c) without calcium acquired on a 500 MHz (^{1}H frequency) spectrometer. Both spectra were acquired with the same number of scans (4096) at -20 °C, below the liquid crystal phase transition, to remove spurious contributions from the natural abundance POPC headgroup. Both spectra were zero filled to twice the original data size and line broadened 0.2 ppm.

Previous studies have shown that plasma Ca^{2+} concentrations can cause PS to cluster into microdomains (*18, 19*). Initial analysis of these microdomains began by comparing one-dimensional ^{13}C spectra of mixed POPS*:POPC bilayers and the effects Ca^{2+} has on the chemical shifts, which are sensitive to binding events and structural changes. One-dimensional CP ^{13}C spectra at -20 °C (Figure 1) were acquired on liposomes containing 30% POPS*, 70% POPC in the presence and absence of 2.5 mM Ca^{2+}. Signals due to natural abundance ^{13}C on the fatty acyl

chains are readily observed below 40 ppm (one resonance at ~132 ppm is ascribed to the olefinic carbons in the oleoyl chain) and consistent with previous SSNMR assignments of lipids in bilayers (*39*). Spectra of liposomes in the presence of 2.5 mM Ca^{2+} contain distinct ^{13}C resonances (Figure 1b) from POPS* headgroups. Two resonances, at 66.26 and 67.91 ppm, are observed for the POPS* alpha carbon (Cα), and the POPS* beta carbon (Cβ) peak, at ~60 ppm, is broadened (line width 190 Hz) indicating two unresolved signals. Similarly, the POPS* gamma carbon (Cγ) (at ~174.2 ppm) resonance is also slightly broadened to 131 Hz, which, while not as dramatic as the Cβ, is still consistent with two unresolved signals. The appearance of two chemical shifts for the carbons in the PS headgroup is indicative of two distinct chemical environments for the PS in the presence of Ca^{2+} that are long lived on the NMR time scale (>5 ms). This result is compatible with earlier studies (*21, 22*) that show PS headgroups, in mixed bilayers, adopt two conformations in the presence of Ca^{2+}. In the absence of Ca^{2+} (Figure 1c), at -20 °C, the POPS*:POPC liposomes display very broad resonances from ~55 to ~67 and from ~170 to ~180 ppm. These broad resonances are attributed to the PS headgroup adopting multiple confirmations leading to multiple chemical shift values. Spectra of these liposomes in the absence of Ca^{2+} at 10 °C (data not shown) contain only one chemical shift value for each POPS* carbon signal indicating the multiple conformations are in fast exchange on the NMR timescale (exchange between conformations is <5 ms). The liposomes with Ca^{2+} exhibit the same splitting of the POPS* Cα, and broadening of the POPS* Cβ and Cγ resonances in spectra acquired at 10 °C as seen at -20 °C (not shown).

6.5.2 Ca^{2+}-PS interactions observed in Nanodiscs

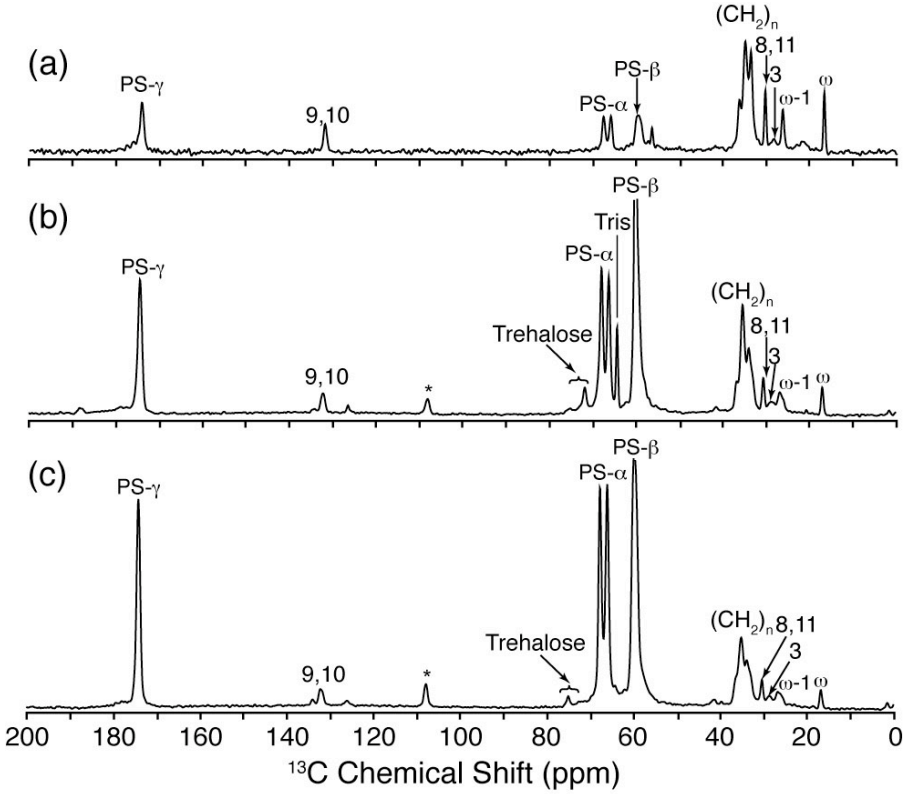

Figure 6.2 One-dimensional ^{13}C spectra of POPS*:POPC liposomes and Nanodiscs with Ca^{2+}.

^{13}C One-dimensional spectra of (a) 10% POPS*, 90% POPC liposomes containing 2.5 mM calcium (b) 30% POPS*, 70% POPC Nanodisc containing 2 mM calcium and, (c) 70% POPS*, 30% POPC Nanodisc sample with 2 mM calcium. All spectra were acquired at -20 °C with an MAS rate of 10.000 kHz on a 600 MHz (H1 frequency) spectrometer; asterisks indicate a carrier frequency artifact at ~108 ppm. All spectra were zero filled to twice the original data size and line broadened 0.2 ppm.

We investigated the effect of Ca^{2+} on PS headgroups using two different membrane mimetics: liposomes and Nanodiscs. Samples were prepared with 10%, 30% or 70% POPS* (balance = POPC). The 10% POPS* sample was prepared in liposomes while the 30% and 70% POPS* samples were prepared using the Nanodisc system. All samples were prepared in the presence of 2 mM Ca^{2+}. One-dimensional ^{13}C spectra were acquired for all three samples (Figure 2). The spectra are consistent with the spectrum from Figure 1b, with identical chemical shifts observed for the POPS* headgroup carbons. These data show that the same Ca^{2+}-induced PS conformations are present in both liposomes and Nanodiscs over a range of PS concentrations.

6.5.3 Ca^{2+}-PS Interactions Alter the Phase Transition and Dynamics of Lipids within the Bilayer

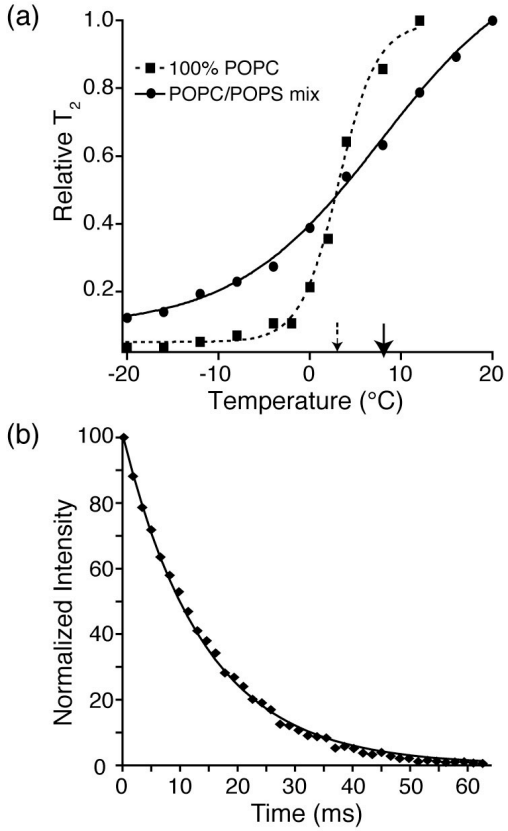

Figure 6.3 Relaxation measurements of Ca^{2+} bound PS.

a) Normalized ^1H T_2 values of the bulk fatty acyl CH_2 peaks of nanobilayers, as a function of temperature. Nanodiscs had either 100% POPC (squares with dashed lines) or 30%POPS*, 70% POPC (circles with solid lines) prepared in the presence of 2 mM Ca^{2+}. The data was acquired over a temperature range of -20 to 20 °C. Transition temperatures were determined using signals from the lipid side chains. ^1H T_2 values were used to fit the inflection point of the curve as a function of temperature. The solid arrow just above the x-axis denotes the lipid phase transition for the 30%POPS*, 70% POPC Nanodiscs (~8 °C), while the dotted arrow denotes the phase transition for 100% POPC Nanodiscs (~3 °C). (b) ^1H Hahn echo experiment was used to investigate the T_2 of the methylene protons (8 and 11; Figure 1a) neighboring the olefinic bond at 25 °C. Plotted is the intensity of the methylene proton peak as a function of the echo time. A single exponential decay curve is shown fit to the data (using Spinsight 3.0). Both a single and bi-exponential function were fit to the data. An F test of the single exponential and bi-exponential fits resulted in an F statistic of 1.00 confirming that the best fit is a single exponential decay. The T_2 was calculated to be 14.1 ms.

We investigated the dynamics of Ca^{2+}-induced PS clustering by examining the change in the phase transition of the mixed POPS:POPC Nanodisc bilayers in the presence of Ca^{2+}. ^1H T_2

values of directly detected ^{1}H spectra over a ±20 °C temperature range reveal acyl chain dynamics as a function of temperature (Figure 3a). We confirmed the expected ~3 °C phase transition of pure POPC Nanodisc bilayers (Figure 3a) observed in previous differential scanning calorimetry measurements (*40*). Dynamics measurements on mixed lipid POPS*:POPC Nanodiscs with 2 mM Ca^{2+} (Figure 3a), display a broad (range of 30 °C) and slightly elevated phase transition in comparison to POPC Nanodisc. This effect has been reported previously using other membrane mimetics (*41-43*) and is attributed to the Ca^{2+}-PS coordination. The acyl chain dynamics that dictate the ^{1}H T_2 report the transition as a bulk property; however, subtleties in the data arise from site-specific variations in dynamics along the acyl chain approaching the PS headgroup.

An additional dynamics study was performed on the POPC Nanodisc bilayer to investigate the presence of a boundary layer of lipids whose lateral mobility would be severely restricted and distort the phase transition. The ^{1}H T_2 (at 25°C) of the methylene protons neighboring the olefinic bond (position 8 and 11 of Figure 1a), unique to the lipid acyl chain, were measured to prevent spurious contributions from MSP protons (Figure 3b). A single exponential fit best described (Figure 3b) the decay behavior indicating that all the lipids are mobile within the Nanodisc and diffuse freely. The interactions of lipids with the membrane scaffold protein occur in the rapid exchange regime and have a negligible effect on the phase transition.

To further understand the dynamics of Ca^{2+} on the POPS*:POPC bilayers, a more detailed, site-specific investigation of the bilayer dynamics was performed. Site-specific dynamics measurements using SSNMR were acquired for POPS*:POPC Nanodisc bilayers utilizing the symmetry based recoupling sequence $R18_1^7$ (*44*), which reports on amplitudes of motions on the microsecond and faster time scale. These studies show that the serine headgroups have very little

motional freedom over a temperature range of 20 °C to -30 °C in the presence of calcium ions (Figure 4); in contrast, the acyl chains' motions are more varied over the same temperature range, becoming less mobile as the temperature is decreased. The $R18_1^7$ sequence recouples the ^1H-^{13}C-dipolar interactions and signal intensity measured as a function of time reports on the dynamics of the system. Observed here are the ^1H-Cα and ^1H-Cβ relaxation curves due to ^1H-^{13}C-dipolar interactions of the POPS* headgroup at varying temperatures (Figure 4a,b). These time domain trajectories represent the rigid lattice limit of motion (S≈0.95) over a range of temperatures from 20 °C to -30 °C. This shows that, both above and below the phase transition, there is very little to no motion in the headgroup. However, the same interactions of the CH_2 groups of the acyl chain show a much larger dependence on temperature changes with an order parameter that goes from 0.3 to 0.8 as the temperature goes from 20 °C to -30 °C (Figure 4c).

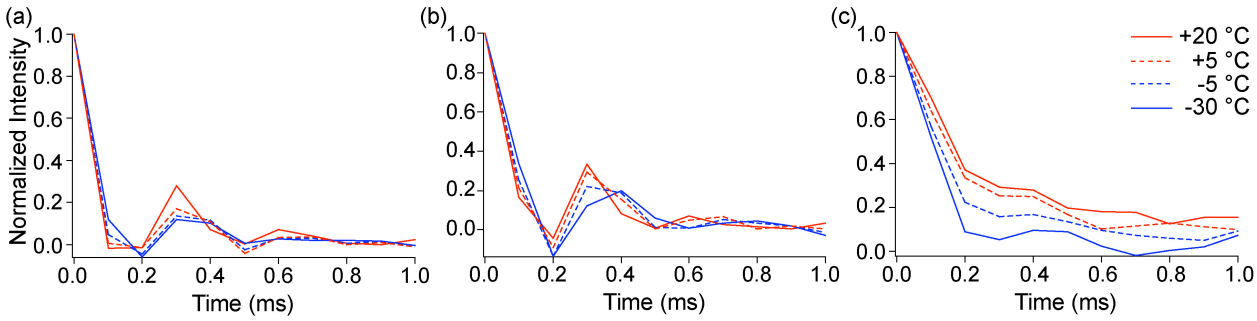

Figure 6.4 Dynamics of PS headgroups and acyl chains.

Dynamics of phospholipid headgroups and acyl chains in 30%POPS*, 70% POPC Nanodiscs in the presence of 2 mM Ca^{2+} as a function of temperature. ^1H-^{13}C dipolar trajectories (plotted as normalized intensities) are presented at the indicated temperatures for (a) the Cα (CH_2) of the serine headgroup, (b) the Cβ (CH) of the serine headgroup, and (c) the bulk CH_2 (resonance at 32 ppm of Figure 2b) group of fatty acyl chains, recoupled using $R18_1^7$. The PS headgroup maintains an order parameter near the rigid lattice limit (S=X), while the acyl chain motion is substantially activated (S= X to Y) over the range from -30 °C to +20 °C.

6.5.4 Two-dimensional Spectra of POPS:POPC Nanodiscs*

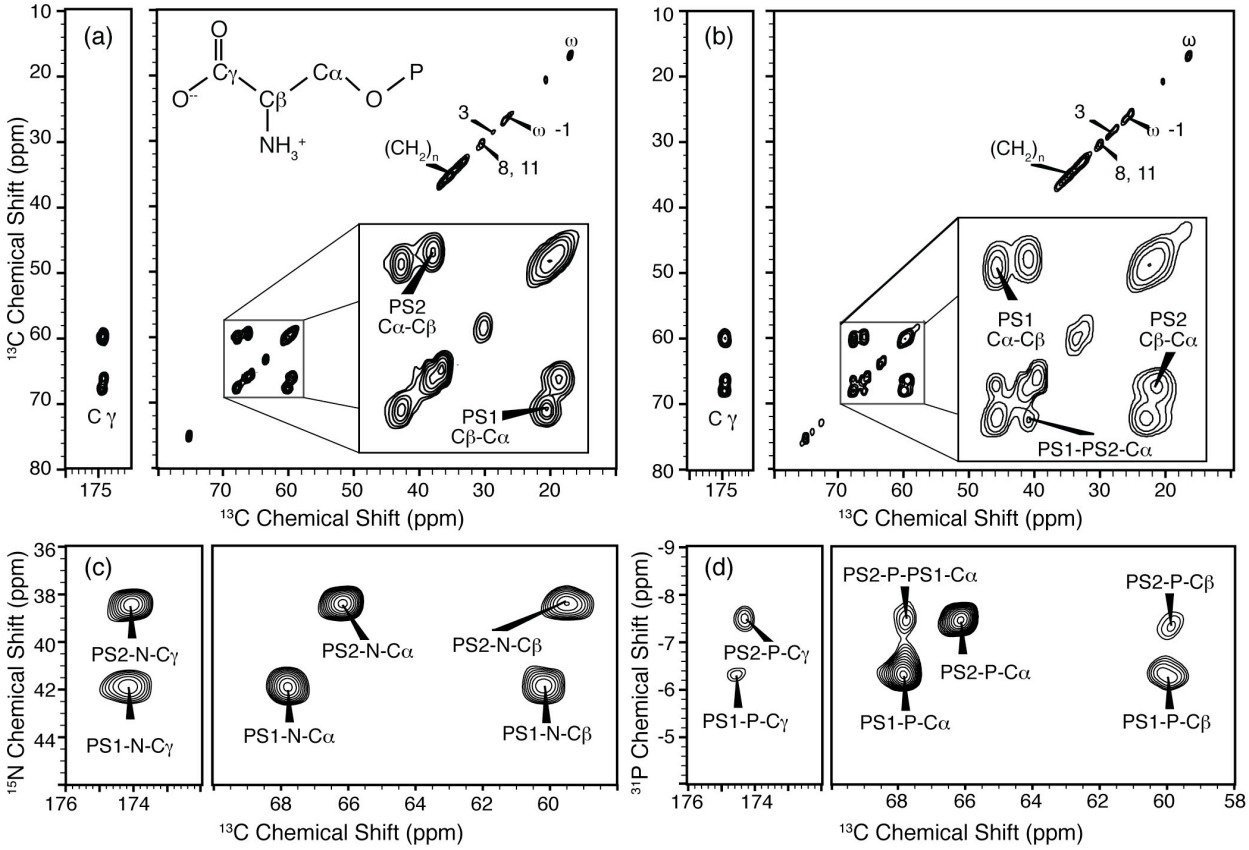

Figure 6.5 Two-dimensional SSNMR spectra of 70% POPS*, 30% POPC Nanodiscs.

Ca^{2+} induces two conformations of PS headgroups as evidenced by two-dimensional SSNMR. 70% POPS*, 30% POPC Nanodiscs were prepared with 2 mM Ca^{2+} and spectra were acquired with an MAS rate of 10 kHz on a 600 MHz (^{1}H frequency) spectrometer. ^{13}C-^{13}C 2D DARR spectra with (a) 25 ms DARR mixing acquired at -30 °C and (b) with 200 ms DARR mixing acquired at 5 °C. For both a+b panels, the insets are expansions of the Cα-Cβ regions. The phosphorus and nitrogen chemical shifts of the two Ca^{2+}-induced conformers are also well resolved as shown in expansions of the serine Cα-Cβ and Cγ regions of (c) ^{15}N-^{13}C TEDOR spectrum with 6.4 ms REDOR mixing acquired at -10 °C and (d) ^{31}P-^{13}C TEDOR spectrum with 2.4 ms of REDOR mixing acquired at -20 °C. All spectra were zero filled to twice the original data size. The ^{13}C-^{13}C two-dimensional spectra were line broadened 0.2 ppm in both dimensions.

Using a series of two-dimensional spectra (Figure 5) acquired on the 70% POPS*, 30% PPC Nanodisc sample in the presence of 2 mM Ca^{2+} we site specifically assign the chemical shifts of the two PS headgroup conformations and report on intra and intermolecular correlations of the two conformers. We acquired ^{13}C-^{13}C, ^{15}N-^{13}C, and ^{31}P-^{13}C two-dimensional spectra (Figure 5)

and assigned the chemical shifts for both PS spin systems (Table 1) for all carbon, nitrogen and phosphorous atoms. We have labeled the two spin systems PS1 and PS2 (Table 1), based on appearance of chemical shifts. The ^{13}C-^{13}C two-dimensional spectra were acquired with 25 and 200 ms of DARR mixing (*45, 46*) (Figure 5a,b). The carbon signals arising from the natural abundant ^{13}C on the acyl chains are again seen along the diagonal below 40 ppm; no cross peaks are observed or expected from these resonances. ^{13}C-^{13}C spectra with 25 ms DARR mixing (Figure 5a) show intramolecular Cα-Cβ cross peaks of both PS1 and PS2. The ratio of integrated intensity of the PS1:PS2 intramolecular Cα-Cβ cross peaks is 52:48, indicating that the PS is divided approximately equally between the two conformations. Additionally, intramolecular Cα-Cγ and Cβ-Cγ correlations are observed for both conformations. Similar intramolecular correlations are observed between both ^{15}N and ^{31}P of the two PS conformations and the three carbon resonances (Cα, Cβ, Cγ) in the ^{15}N-^{13}C and ^{31}P-^{13}C two-dimensional TEDOR (*47*) spectra (Figure 5c,d).

	Chemical Shift Value (ppm)				
	Cα	Cβ	Cγ	N	P
PS1	67.91	60.18	174.38	41.82	-6.29
PS2	66.26	59.55	174.19	38.43	-7.40

Table 6.1 Carbon, nitrogen and phosphorous chemical shift values for PS headgroups bound to Ca^{2+} in mixed POPS:POPC bilayers.

Intra and intermolecular correlations in the two-dimensional spectra reveal structural insights of individual PS headgroups and on clustering of the two conformations, respectively. Both TEDOR (heteronuclear) (*47*) and DARR (homonuclear) (*45, 46*) pulse sequences take advantage of strong dipolar interactions present in SSNMR. The dipolar interaction is a through space interaction and therefore inherently contains information on distance ($\propto 1/r^3$) that is reflected in

the intensity of the cross peaks as a function of mixing time. Using the ^{13}C-^{13}C and ^{13}C-^{31}P dipolar interactions, distances up to ~6 Å can be measured between atoms. The ^{31}P-^{13}C TEDOR spectrum (Figure 5d) contains P-Cγ and P-Cβ intramolecular cross peaks with differing intensities for the PS1 and PS2 conformation. The intensities of the cross peaks are directly related to carbon-phosphorous distances. Preliminary distance data (not shown) collected with ^{31}P-^{13}C TEDOR spectra indicate that Cγ-P distance in PS1 is ~4 Å. The other conformation, PS2, adopts a more extended structure with an approximate Cγ-P distance of ~5 Å. The preliminary data on the PS1 and PS2 conformations do not exclude the two headgroup conformers solved previously at pH 7.5 for 1,2-dimyristoyl-phosphatidylserine (DMPS) in dodecylphosphocholine (DPC) micelles (*20*). The two conformations solved previously were done at varying pH, in the presence of Na^{2+} and are in fast chemical exchange (*20, 48*). The data presented here suggest that the Ca^{2+} coordination does not necessarily change the headgroup structures, but there is a definite change in the exchange rate between headgroups. Our data show that in the presence of Ca^{2+} the PS1 and PS2 are in slow chemical exchange on the NMR time scale. More structural investigations are underway to solve atomically resolved structures for PS1 and PS2 conformations in the presence of Ca^{2+}.

Finally, using ^{13}C-^{13}C DARR spectrum with 200 ms mixing, and the ^{31}P-^{13}C TEDOR spectrum (Figure 5b,d) we show direct evidence of Ca^{2+} induced PS clustering. The ^{13}C-^{13}C DARR spectrum with 200 ms mixing (Figure 5b) shows a cross peak between the Cα of PS1 and the Cα of PS2. Additionally, the ^{31}P-^{13}C TEDOR spectrum (Figure 5d) has an intermolecular correlation from the phosphorous of PS2 to the Cα of PS1. These intermolecular cross peaks are evidence of a distance of 5-6 Å between PS1 and PS2 and give insight into the geometric arrangement of the PS clusters. These distance measurements are preliminary and more distance

constraints coupled with angular restraints are necessary for a full calculation of an atomically resolved structure of the Ca^{2+} induced PS microdomain.

6.6 Discussion

Calcium interactions not only induce specific conformations of the PS headgroup but also arrange the two conformations within ~6 Å of each other. The spectra show the presence of two conformations of PS in the presence of Ca^{2+}. These findings are consistent with previous studies (*21, 22*) and extend on the current knowledge with site-specific assignments of the two conformations, PS1 and PS2, for headgroup nitrogen, carbon and phosphorous resonances (Table 1). Previous work has reported on the structure of PS in the presence of Na^{+} in mixed DPC:DMPS micelles (*20*). Sanson *et al*. reported two dominate PS species and focused on the conformation of the glycerol backbone. No angular or distance data was specifically reported for the serine headgroups. This makes comparing our preliminary distance data with previous structures difficult. Therefore, we cannot exclude or confirm the existence of these structures in the Ca^{2+} induced PS-clusters. What is of significant note is a major change in the dynamics of the conformations in the presence of Ca^{2+}. PS conformers in the presence of Na^{+} are in fast chemical exchange and are likely to have intermediate structures during exchange (*20, 48*). We note that this fast exchange between conformations, in the absence of Ca^{2+}, results in only one chemical shift value for the three carbons (Cα, Cβ, Cγ) above the phase transition and broad signals below the phase transition (Figure 1c). Addition of calcium to the system coordinates PS into two distinct conformations, changing the dynamics of the system, so that PS1 and PS2 are long lived on the NMR timescale.

Additionally, we report on the intermolecular organization of the PS1 and PS2 conformers. Two-dimensional ^{13}C-^{13}C and ^{31}P-^{13}C spectra revealed cross peaks between PS1 and PS2

conformations, which indicate that the two conformers are within ~5-6 Å of each other. POPS lipids are split evenly between the two conformers, suggesting that each cluster contains an approximate two-fold symmetric organization of PS headgroups within 6 Å of each other around Ca^{2+} coordination centers. This conclusion is consistent with binding data and molecular dynamics simulations that show a 2:1 ratio of PS:Ca^{2+} (*49-51*); though, the exact stoichiometry of the coordination center is yet to be determined.

The results of the dynamics studies using the Nanodisc system demonstrate that Ca^{2+} interactions with mix POPS:POPC bilayers are consistent with previous studies using liposomes (*21, 22, 43, 52*). Our site-specific dynamics data (Figure 4) show interactions of Ca^{2+} with mixed POPS:POPC bilayers cause the PS headgroups to become highly ordered, while, the acyl chains are only slightly affected by this ordering. This detailed investigation of the dynamics explains the increase in the liquid-crystalline to solid-gel phase transition of these mixed bilayers presented earlier (Figure 3a) and observed by others (*41-43*). As Browning *et al*. reported (*52*), in the presence of Ca^{2+}, the PS headgroup does not dominate the properties of the hydrophobic tails in the liquid-crystalline state. The restricted motion of the headgroup translates minimally to the carbons on the acyl chains near the glycerol backbone causing slight increase and broadening in the transition temperature. This is what we would expect in the model where headgroups in PS microdomains are locked in position by the coordination of Ca^{2+}; while the acyl chains experience only slight restrictions on their motion. We propose that Ca^{2+} induces a liquid-ordered phase (*53*) in which there is some order to system (in the PS headgroups) but the acyl chains remain disordered as in a liquid phase. We picture this as a microdomain of PS where diffusion of PS within the microdomain is likely and the microdomain, as a whole unit, is free to diffuse laterally in the bilayer. This picture is consistent with the dynamics data including the increase in

the liquid-crystalline to solid-gel phase transition temperature as well as a broadening of this transition.

The results of Ca^{2+} induced PS-clustering into microdomains on Nanodisc samples and liposomes samples are identical. This investigation demonstrates that the Nanodisc system is an excellent tool for investigating Ca^{2+} interactions with biological membranes and has several advantages over liposomes. Liposomes have short sample lifetimes, do not tolerate temperature fluctuations well and are limited in the range of PS concentrations available in the presence of Ca^{2+}. In contrast, Nanodiscs are thermostable and have a sample lifetime measured in years and have advantages over liposomes in ease of SSNMR sample preparation. Nanodisc samples are lyophilized prior to packing into a SSNMR rotor. This allows for the efficient transfer (~80%) of powder to the SSNMR rotor verses a gelatinous liposome pellet. After lyophilization the Nanodiscs are rehydrated to 50% by mass with deionized water. Liposomes do not tolerate lyophilization well and transfer of the centrifuged liposome pellet into the SSNMR rotor is ~50% efficient. Furthermore, liposome samples prepared for SSNMR are only stable for 1-2 weeks, while Nanodisc samples have long lifetimes (years). One key advantage of the Nanodisc system is that it allows facile control of the lipid content on the nanoscale. Liposomes with high PS content are unstable in the presence of calcium, forming PS-Ca^{2+} cochleate in samples that contain >40% PS (*42, 54*). Nanodiscs allow for as much as 90% PS to be incorporated into the membrane bilayer in the presence of Ca^{2+}. The increased stability and inherent control of lipid composition over a range of PS concentrations allows for the effective isolation of PS-microdomains. These domains have locally high PS concentrations and are where key biological interactions take place (*18, 19*).

In conclusion, we have demonstrated that Ca^{2+} interacts with PS in membrane bilayers to form liquid-ordered microdomains. The interaction forms a symmetric organization of the PS in the lipid bilayer, which is free to diffuse laterally through the bilayer. This presents a unique binding site for PS-Ca^{2+} dependent membrane proteins. Nanodiscs are an excellent membrane mimetic to investigate these structures. Current work in the lab is focused on completing analysis of distance and angular restraints to use in calculations of an atomically resolved structure of the PS microdomains in membrane bilayers. Structural understandings of these PS microdomains will give insight into many biologically relevant membrane-protein interactions that are dependent on presence of Ca^{2+} and PS containing membranes.

6.7 Acknowledgement

The authors would like to thank Dr. Steven Sligar and Dr. Aleksandra Kijac for assistance with the Nanodisc system; Lindsay Sperling for help with dynamics simulations; Drs. Emad Tajkhorshid and Y. Zenmei Ohkubo for many useful discussions; and Dr. Jennifer Rap (NMR Facility, School of Chemical Sciences, University of Illinois at Urbana-Champaign) for assisting in acquisition of experiments.

6.8 References

1. Fernandez-Chacon, R., Shin, O. H., Konigstorfer, A., Matos, M. F., Meyer, A. C., Garcia, J., Gerber, S. H., Rizo, J., Sudhof, T. C., and Rosenmund, C. (2002) Structure/function analysis of Ca^{2+} binding to the C(2)A domain of synaptotagmin 1. *J. Neurosci. 22*, 8438-8446.
2. Zhang, X. Y., Rizo, J., and Sudhof, T. C. (1998) Mechanism of phospholipid binding by the C(2)A-domain of synaptotagmin I. *Biochemistry 37*, 12395-12403.

3. Bhalla, A., Tucker, W. C., and Chapman, E. R. (2005) Synaptotagmin isoforms couple distinct ranges of Ca^{2+}, Ba^{2+}, and Sr^{2+} concentration to SNARE-mediated membrane fusion. *Mol. Biol. Cell 16*, 4755-4764.

4. Potoff, J. J., Issa, Z., Manke, C. W., and Jena, B. P. (2008) Ca^{2+}-dimethylphosphate complex formation: Providing insight into Ca^{2+}-mediated local dehydration and membrane fusion in cells. *Cell Biol. Int. 32*, 361-366.

5. Jeremic, A., Kelly, M., Cho, J. A., Cho, S. J., Horber, J. K. H., and Jena, B. P. (2004) Calcium drives fusion of SNARE-apposed bilayers. *Cell Biol. Int. 28*, 19-31.

6. Jeremic, A., Cho, W. J., and Jena, B. P. (2004) Membrane fusion: What may transpire at the atomic level. *J. Biol. Phys. Chem. 4*, 139-142.

7. Verdaguer, N., Corbalan-Garcia, S., Ochoa, W. F., Fita, I., and Gomez-Fernandez, J. C. (1999) Ca^{2+} bridges the C2 membrane-binding domain of protein kinase C alpha directly to phosphatidylserine. *EMBO J. 18*, 6329-6338.

8. Evans, J. H., Murray, D., Leslie, C. C., and Falke, J. J. (2006) Specific translocation of protein kinase C alpha to the plasma membrane requires both Ca^{2+} and PIP2 recognition by its C2 domain. *Mol. Biol. Cell 17*, 56-66.

9. Corbin, J. A., Evans, J. H., Landgraf, K. E., and Falke, J. J. (2007) Mechanism of specific membrane targeting by C2 domains: Localized pools of target lipids enhance Ca^{2+} affinity. *Biochemistry 46*, 4322-4336.

10. Zwaal, R. F., Comfurius, P., and Bevers, E. M. (1998) Lipid-protein interactions in blood coagulation. *Biochim Biophys Acta 1376*, 433-53.

11. Nelsestuen, G. L., Shah, A. M., and Harvey, S. B. (2000) Vitamin K-dependent proteins. *Vitam. Horm. 58*, 355-389.

12. Stenflo, J. (1999) Contributions of Gla and EGF-like domains to the function of vitamin K dependent coagulation factors. *Crit. Rev. Eukaryotic Gene Expression 9*, 59-88.

13. Ohkubo, Y. Z., and Tajkhorshid, E. (2008) Distinct structural and adhesive roles of Ca^{2+} in membrane binding of blood coagulation factors. *Structure 16*, 72-81.

14. Rosing, J., Tans, G., Goversriemslag, J. W. P., Zwaal, R. F. A., and Hemker, H. C. (1980) Role of Phospholipids and Factor-Va in the Prothrombinase Complex. *J. Biol. Chem. 255*, 274-283.

15. Huang, M. D., Rigby, A. C., Morelli, X., Grant, M. A., Huang, G. Q., Furie, B., Seaton, B., and Furie, B. C. (2003) Structural basis of membrane binding by Gla domains of vitamin K-dependent proteins. *Nat. Struct. Biol. 10*, 751-756.

16. Morrissey, J. H., Pureza, V., Davis-Harrison, R. L., Sligar, S. G., Ohkubo, Y. Z., and Tajkhorshid, E. (2008) Blood clotting reactions on nanoscale phospholipid bilayers. *Thromb. Res. 122*, S23-6.

17. Falls, L. A., Furie, B., Jacobs, M., Furie, B., and Rigby, A. C. (2001) The ω-loop region of the human prothrombin γ-carboxyglutamic acid domain penetrates anionic phospholipid membranes. *J. Biol. Chem. 276*, 23895-23902.

18. Haverstick, D. M., and Glaser, M. (1987) Visualization of Ca^{2+}-Induced Phospholipid Domains. *Proc. Natl. Acad. Sci. USA 84*, 4475-4479.

19. Yang, L., and Glaser, M. (1996) Formation of membrane domains during the activation of protein kinase C. *Biochemistry 35*, 13966-13974.

20. Sanson, A., Monck, M. A., and Neumann, J. M. (1995) 2D ^{1}H-NMR Conformational Study of Phosphatidylserine Diluted in Perdeuterated Dodecylphosphocholine Micelles - Evidence for a pH-Induced Conformational Transition. *Biochemistry 34*, 5938-5944.

21. Roux, M., and Bloom, M. (1990) Ca^{2+}, Mg^{2+}, Li^{+}, Na^{+}, and K^{+} Distributions in the Headgroup Region of Binary Membranes of Phosphatidylcholine and Phosphatidylserine as Seen by Deuterium NMR. *Biochemistry 29*, 7077-7089.

22. Roux, M., and Bloom, M. (1991) Calcium-Binding by Phosphatidylserine Headgroups - Deuterium NMR-Study. *Biophys. J. 60*, 38-44.

23. Bayburt, T. H., and Sligar, S. G. (2003) Self-assembly of single integral membrane proteins into soluble nanoscale phospholipid bilayers. *Protein Sci. 12*, 2476-2481.

24. Bayburt, T. H., and Sligar, S. G. (2002) Single-molecule height measurements on microsomal cytochrome P450 in nanometer-scale phospholipid bilayer disks. *Proc. Natl. Acad. Sci. USA 99*, 6725-6730.

25. Bayburt, T. H., Grinkova, Y. V., and Sligar, S. G. (2002) Self-assembly of discoidal phospholipid bilayer nanoparticles with membrane scaffold proteins. *Nano Lett. 2*, 853-856.

26. Bayburt, T. H., Carlson, J. W., and Sligar, S. G. (2000) Single molecule height measurements on a membrane protein in nanometer-scale phospholipid bilayer disks. *Langmuir 16*, 5993-5997.

27. Morrissey, J. H., Pureza, V., Davis-Harrison, R. L., Sligar, S. G., Rienstra, C. M., Kijac, A. Z., Ohkubo, Y. Z., and Tajkhorshid, E. (2009) Protein-membrane interactions: blood clotting on nanoscale bilayers. *J. Thromb. Haemost. 7*, 169-172.

28. Li, Y., Kijac, A. Z., Sligar, S. G., and Rienstra, C. M. (2006) Structural analysis of nanoscale self-assembled discoidal lipid bilayers by solid-state NMR spectroscopy. *Biophys. J. 91*, 3819-3828.

29. Frericks, H. L., Zhou, D. H., Yap, L. L., Gennis, R. B., and Rienstra, C. M. (2006) Magic-angle spinning solid-state NMR of a 144 kDa membrane protein complex: E-coli cytochrome bo_3 oxidase. *J. Biomol. NMR 36*, 55-71.

30. Kijac, A. Z., Li, Y., Sligar, S. G., and Rienstra, C. M. (2007) Magic-Angle Spinning Solid-State NMR Spectroscopy of Nanodisc-Embedded Human CYP3A4. *Biochemistry 46*, 13696-13703.

31. Iwasaki, Y., Mizumoto, Y., Okada, T., Yamamoto, T., Tsutsumi, K., and Yamane, T. (2003) An aqueous suspension system for phospholipase D-mediated synthesis of PS without toxic organic solvent. *J. Am. Oil Chem. Soc. 80*, 653-657.

32. Comfurius, P., and Zwaal, R. F. A. (1977) Enzymatic-Synthesis of Phosphatidylserine and Purification by Cm-Cellulose Column Chromatography. *Biochim. Biophys. Acta 488*, 36-42.

33. Van Geet, A. L. (1968) *Anal. Chem. 42*, 2227.

34. Hediger, S., Meier, B. H., Kurur, N. D., Bodenhausen, G., and Ernst, R. R. (1994) NMR cross-polarization by adiabatic passage through the Hartmann-Hahn condition (APHH). *Chem. Phys. Lett. 223*, 283-288.

35. Bennett, A. E., Rienstra, C. M., Auger, M., Lakshmi, K. V., and Griffin, R. G. (1995) Heteronuclear decoupling in rotating solids. *J. Chem. Phys. 103*, 6951-6958.

36. Delaglio, F., Grzesiek, S., Vuister, G. W., Zhu, G., Pfeifer, J., and Bax, A. (1995) NMRpipe: a Multidimensional Spectral Processing System Based On Unix Pipes. *J. Biomol. NMR 6*, 277-293.

37. Morcombe, C. R., and Zilm, K. W. (2003) Chemical shift referencing in MAS solid state NMR. *J. Magn. Reson. 162*, 479-486.

38. Goddard, T. D., and Kneller, D. G., University of California, San Francisco.

39. Husted, C., Montez, B., Le, C., Moscarello, M. A., and Oldfield, E. (1993) ^{13}C Magic-Angle Sample-Spinning Nuclear-Magnetic-Resonance Studies of Human Myelin, and Model Membrane Systems. *Magnet. Reson. Med. 29*, 168-178.

40. Denisov, I. G., McLean, M. A., Shaw, A. W., Grinkova, Y. V., and Sligar, S. G. (2005) Thermotropic phase transition in soluble nanoscale lipid bilayers. *J. Phys. Chem. B 109*, 15580-8.

41. Jacobson, K., and Papahadjopoulos, D. (1975) Phase-Transitions and Phase Separations in Phospholipid Membranes Induced by Changes in Temperature, Ph, and Concentration of Bivalent-Cations. *Biochemistry 14*, 152-161.

42. Silvius, J. R., and Gagne, J. (1984) Calcium-Induced Fusion and Lateral Phase Separations in Phosphatidylcholine-Phosphatidylserine Vesicles - Correlation by Calorimetric and Fusion Measurements. *Biochemistry 23*, 3241-3247.

43. Sinn, C. G., Antonietti, M., and Dimova, R. (2006) Binding of calcium to phosphatidylcholine-phosphatidylserine membranes. *Colloids Surf., A 282*, 410-419.

44. Zhao, X., Eden, M., and Levitt, M. H. (2001) Recoupling of heteronuclear dipolar interactions in solid-state NMR using symmetry-based pulse sequences. *Chem. Phys. Lett. 342*, 353-361.

45. Takegoshi, K., Nakamura, S., and Terao, T. (2001) ^{13}C-^{1}H dipolar-assisted rotational resonance in magic-angle spinning NMR. *Chem. Phys. Lett. 344*, 631-637.

46. Morcombe, C. R., Gaponenko, V., Byrd, R. A., and Zilm, K. W. (2004) Diluting abundant spins by isotope edited radio frequency field assisted diffusion. *J. Am. Chem. Soc. 126*, 7196-7197.

47. Hing, A., Vega, S., and Schaefer, J. (1992) Transferred-echo double-resonance NMR. *J. Magn. Reson. 96*, 205-209.

48. Hauser, H., Pascher, I., and Sundell, S. (1988) Preferred Conformation and Dynamics of the Glycerol Backbone in Phospholipids - an NMR and X-Ray Single-Crystal Analysis. *Biochemistry 27*, 9166-9174.

49. Mattai, J., Hauser, H., Demel, R. A., and Shipley, G. G. (1989) Interactions of Metal-Ions with Phosphatidylserine Bilayer-Membranes - Effect of Hydrocarbon Chain Unsaturation. *Biochemistry 28*, 2322-2330.

50. Feigenson, G. W. (1986) On the Nature of Calcium-Ion Binding between Phosphatidylserine Lamellae. *Biochemistry 25*, 5819-5825.

51. Vernier, P. T., Ziegler, M. J., and Dimova, R. (2009) Calcium Binding and Head Group Dipole Angle in Phosphatidylserine-Phosphatidylcholine Bilayers. *Langmuir 25*, 1020-1027.

52. Browning, J. L., and Seelig, J. (1980) Bilayers of Phosphatidylserine - Deuterium and Phosphorus Nuclear Magnetic-Resonance Study. *Biochemistry 19*, 1262-1270.

53. van Meer, G., Voelker, D. R., and Feigenson, G. W. (2008) Membrane lipids: where they are and how they behave. *Nat. Rev. Mol. Cell Bio. 9*, 112-124.

54. Hui, S. W., Boni, L. T., Stewart, T. P., and Isac, T. (1983) Identification of Phosphatidylserine and Phosphatidylcholine in Calcium-Induced Phase Separated Domains. *Biochemistry 22*, 3511-3516.

CHAPTER 7

Backbone ^{1}H, ^{13}C, and ^{15}N resonance assignments of the extracellular domain of tissue factor

7.1 Notes and Acknowledgements

This chapter was adapted from John M. Boettcher, Mary Clay, Benjamin J. LaHood, Jamse H. Morrissey, and Chad M. Rienstra (manuscript in preparation). This work was supported by NIH grants R01 GM075937 and R01 HL47014.

7.2 Abstract

^{13}C, ^{15}N, and ^{1}H backbone chemical shift assignments are presented for the extracellular domain of tissue factor. Tissue factor is the integral membrane protein that initiates blood coagulation through the formation an enzymatic complex with the plasma serine protease, factor VIIa.

7.3 Biological context

In normal hemostasis and most thrombotic diseases, blood clotting is triggered upon the assembly of the cell-surface complex of tissue factor (TF) and activated factor VII (FVIIa) (*1*). TF is a type-I integral membrane protein found on the surface of a variety of cells outside the vasculature (*2*), while FVIIa is a plasma serine protease. The TF:FVIIa complex can be considered a two-subunit enzyme, with FVIIa as the catalytic subunit and TF the essential regulatory subunit; it triggers the clotting cascade via limited proteolysis of FIX and FX, which ends in the formation of a fibrin clot.

A 263-residue integral membrane protein, human TF is composed of three domains: the cytoplasmic domain (residues 243-263), a membrane spanning helix (residues 220-242) and the

extracellular domain (residues 1-219) which in turn is composed of two fibronectin type III domains (*3*). The cytoplasmic domain may function in signaling, and the single transmembrane helix anchors the protein in the membrane bilayer. The isolated extracellular domain, referred to as soluble tissue factor (sTF), constitutes the bulk of the protein (~83%) and is the domain that allosterically activates FVIIa. Crystal structures are available for sTF (*4*) as is a ^{1}H-^{15}N HSQC spectrum of sTF (*5*), although no site-specific resonance assignments have been reported for sTF or the full-length, membrane-bound TF. Here we report the assignment of ~90% of the backbone resonances in sTF. These site-specific chemical shift assignments will allow for further investigations into conformational changes of sTF upon interaction with FVIIa and/or the membrane bilayer.

7.4 Methods and experiments

7.4.1 Recombinant Protein Expression and Purification

^{2}H,^{13}C,^{15}N-labeled human sTF protein was expressed in T7 Express *E. coli* cells (New England BioLabs, Inc., Ipswitch, MA) from plasmid pJH677. Detailed expression conditions will be communicated elsewhere (manuscript in preparation); briefly, a starter culture was grown at 37 °C to OD_{600} = 6 in a modified Studier MDG medium (*6*) at natural isotopic abundance. The bacteria were then harvested and resuspended in 3 volumes of fresh medium containing ^{2}H,^{13}C,^{15}N-BioExpress (Cambridge Isotopes Laboratories, Inc., Andover, MA), U-^{13}C-glycerol and phosphate. Specifically, BioExpress (10X stock solution) was diluted to 1X with 100 mM phosphate buffer at pH 7.5. U-^{13}C-glycerol was added at 2 g/L and the culture was grown at 25° C until the OD_{600} reached ~3. Expression of sTF was induced with 20 μM isopropyl β-D-1-thiogalactopyranoside for 24 hours. The cells were harvested, sTF released by osmotic shock, and the cell debris pelleted. The supernatant was purified with Q-Sepharose, Ni^{2+} affinity and gel

filtration chromatography (HiPrep 16/160 Sephacryl S-200, GE Biosciences). This resulted in >95% purity, and a yield of 70-100 mg/L sTF. All purification solutions contained $^{1}H_2O$, in order to exchange backbone amides.

7.4.2 NMR Spectroscopy

Solution NMR spectra were acquired at the School of Chemical Sciences NMR Facility (University of Illinois at Urbana-Champaign) on Varian INOVA 600 MHz and 750 MHz spectrometers equipped with a 5 mm, triple resonance (^{1}H-^{13}C-^{15}N) triaxial gradient probes, using VNMRJ version 2.1B with the BioPack suite of pulse programs. Spectra were acquired at 35 °C on back-exchanged ^{2}H, ^{13}C, ^{15}N-sTF samples (1 mM in a 50 mM phosphate buffer, pH 6.5, containing 50 mM NaCl and 10% D_2O (v/v)). 2D ^{1}H-^{15}N TROSY spectra were measured for an average of two hours per spectrum, digitizing 512 points in the indirect ^{15}N dimension ($t_1$max = 232 ms). The standard suite of TROSY-based heteronuclear triple resonance 3D spectra (HNCO, HN(CA)CO, HNCA, HNCACB, HN(CO)CA) was utilized to establish correlations among backbone resonances of the sTF sample. Measurement times for the 3D spectra were 12 to 48 hours. Spectra were processed with NMRPipe (*7*) and analyzed in Sparky (*8*).

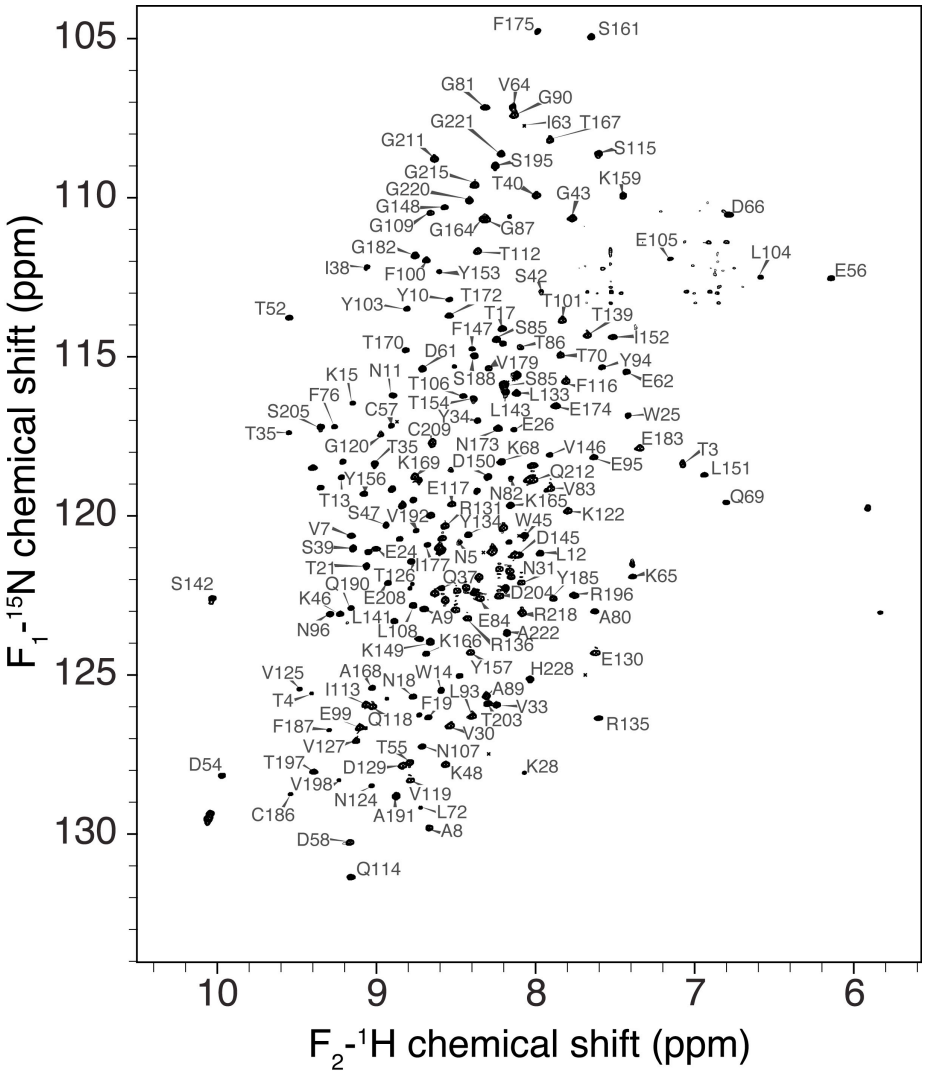

Figure 7.1 ^{15}N-^{1}H 2D TROSY-HSQC NMR spectrum of sTF.

^{15}N-^{1}H 2D TROSY-HSQC NMR spectrum of sTF acquired at 600 MHz (^{1}H frequency) (in phosphate buffer, 50 mM NaCl, pH 6.5, 35 ºC). 213 of the expected 218 resonances are resolved. The spectrum was processed with sine bell apodization and zero filled to at least double the original size in both dimensions. Subsets of the available assignments are labeled.

7.5 Extent of assignments and data deposition

A standard set of triple resonance TROSY based spectra was used to complete ~90% of the H^N, N, Cα, Cβ, C' backbone assignments of sTF; this includes >95% of all the H^N, N, Cα, C' and ~60% of the Cβ. The assignments are deposited in the BMRB under accession number XXX (for release upon publication). The ^{1}H-^{15}N TROSY spectrum (Figure 7.1) is qualitatively

consistent with previously published sTF ^{1}H-^{15}N HSQC spectra, which were not assigned (*5*). The improved sensitivity and resolution enabled us to assign 213 of the expected 218 amide resonances (excluding the 9 prolines but including the 10 residue His tag). We were not able to make unambiguous assignments of residues 77, 78 and 137, or residues 229 and 230 (within the His tag). Residues 77 and 78 precede a proline, and resumption of the backbone walk was further complicated by relatively weak signal intensities throughout this portion of the protein. Residue 137, in a flexible loop, was also missing in the 3D experiments and therefore could not be assigned.

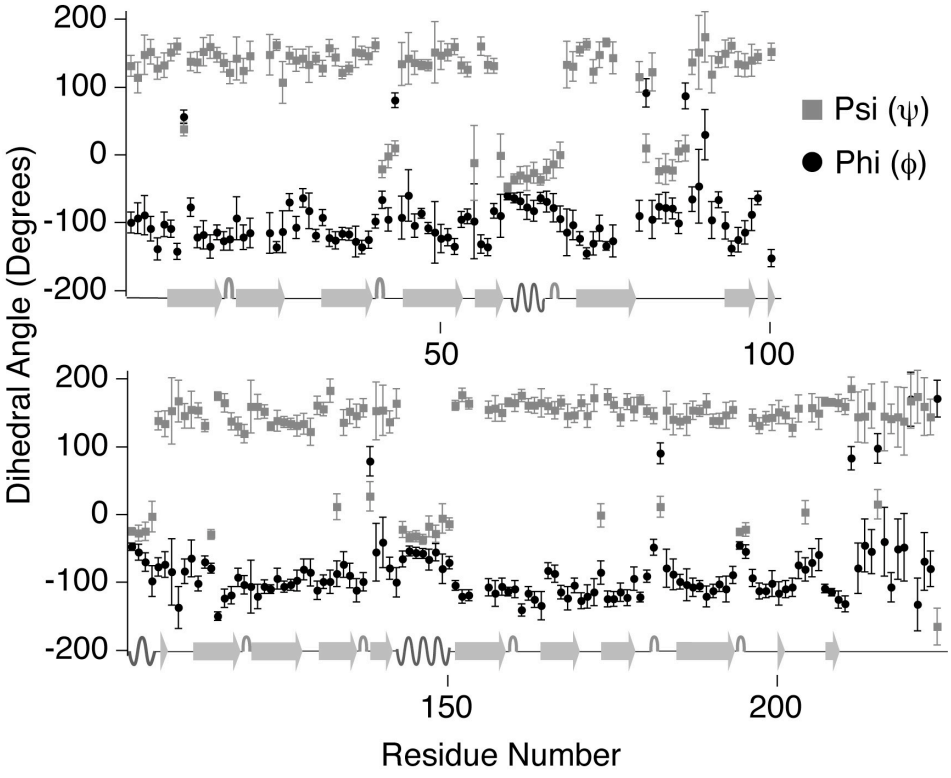

Figure 7.2 Secondary structure elements of sTF identified by chemical shift analysis.

Secondary structure elements of sTF identified by TALOS+ (*9*). Plotted are the Phi (Φ) (black circles) and Psi (Ψ) (gray squares) backbone torsion angles as predicted by TALSO+ (*9*) with error bars. Along the x-axis is a cartoon representation of the secondary structure based on the crystal structure (2HFT (*4*)). The results of the secondary structural analysis show the majority of sTF is β-strand with three α helices (shaded gray boxes), in agreement with the crystal structure.

TALOS+ (*9*) analysis of the secondary structure (Figure 7.2) by NMR illustrates the α-helical and β-strand positions in good agreement with the crystal structure (*4*). We also report data for residues 87 to 90, 161, 162 and 212 to 219 that are not in the crystal structure due to the lack of electron density (*4*). The TALOS+ (*9*) analysis shows that residues 87 to 90 and 212 to 219 are in unstructured, dynamic regions, while residues 161 and 162 are both in an extended conformations.

7.6 References

1. Morrissey, J. H. (2004) Tissue factor: A key molecule in hemostatic and nonhemostatic systems. *Int J Hematol 79*, 103-108.
2. Drake, T. A., Morrissey, J. H., and Edgington, T. S. (1989) Selective Cellular Expression of Tissue Factor in Human-Tissues - Implications for Disorders of Hemostasis and Thrombosis. *Am J Pathol 134*, 1087-1097.
3. Daubie, V., Pochet, R., Houard, S., and Philippart, P. (2007) Tissue factor: a mini-review. *J Tissue Eng Regen Med 1*, 161-9.
4. Muller, Y. A., Ultsch, M. H., and deVos, A. M. (1996) The crystal structure of the extracellular domain of human tissue factor refined to 1.7 angstrom resolution. *J. Mol. Biol. 256*, 144-159.
5. Stone, M. J., Ruf, W., Miles, D. J., Edgington, T. S., and Wright, P. E. (1995) Recombinant Soluble Human Tissue Factor Secreted by Saccharomyces-Cerevisiae and Refolded from Escherichia-Coli Inclusion-Bodies - Glycosylation of Mutants, Activity and Physical Characterization. *Biochem. J 310*, 605-614.
6. Studier, F. W. (2005) Protein production by auto-induction in high density shaking cultures. *Protein Expr Purif 41*, 207-34.

7. Delaglio, F., Grzesiek, S., Vuister, G. W., Zhu, G., Pfeifer, J., and Bax, A. (1995) NMRpipe: a Multidimensional Spectral Processing System Based On Unix Pipes. *J. Biomol. NMR 6*, 277-293.

8. Goddard, T. D., and Kneller, D. G., University of California, San Francisco.

9. Shen, Y., Delaglio, F., Cornilescu, G., and Bax, A. (2009) TALOS plus : a hybrid method for predicting protein backbone torsion angles from NMR chemical shifts. *J. Biomol. NMR 44*, 213-223.

CHAPTER 8

Structural investigations of Tissue Factor, a blood coagulation protein

8.1 Notes and Acknowledgements

This chapter was adapted from a manuscript in preparation by John M. Boettcher, Mary Clay, Benjamin J. LaHood, Rebecca Davis-Harrison, James H. Morrissey, and Chad M. Rienstra. This work was supported by the National Institute of General Medical Sciences, NIH (GM075937-01to C.M.R.), the National Heart Lung and Blood Institute, NIH (HL47014 to J.H.M.), and by the American Heart Association (0920045G to R.D.H.).

8.2 Abstract

The formation of the cell-surface complex of tissue factor (TF) with activated factor VII (FVIIa) initiates blood clotting in normal hemostasis. It is well known that TF allosterically activates FVIIa, though; how TF dramatically increases the activity of FVIIa is not well understood. The TF:FVIIa complex triggers the clotting cascade through activation of factor X and factor IX. Residues in both TF and FVIIa, near the membrane surface, are reported to form an exosite for substrate binding. Several crystal structures and mutagenesis studies have given insights into the TF:FVIIa complex, yet, a complete understanding of essential interactions are lacking. The available crystal structures were solved for the soluble, extracellular domain of TF (sTF), in the absence of membranes. In addition to missing membrane interactions, the structures lack information on many residues reported to be involved in vital allosteric and substrate interactions. Understanding the conformational changes of the key TF residues involved in

allosteric activation and substrate binding will allow a more thorough understanding of the TF:FVIIa complex. Here we report the sTF chemical shift assignments of sTF for 82% of the residues using solid-state NMR, which agree well with previously reported solution chemical shifts for sTF. These data are also compared to initial two-dimensional spectra acquired on membrane bound TF and we report on an interaction between a loop in extracellular domain of TF and the membrane surface involved in the TF:FVIIa substrate binding site.

8.3 Introduction

In normal hemostasis and most thrombotic diseases, blood clotting is triggered upon the assembly of the cell-surface complex of tissue factor (TF) and activated factor VII (FVIIa) (1). TF is a type-I integral membrane protein found on the surface of a variety of cells outside the vasculature (2). The ligand for TF is factor VII (FVII), a plasma serine protease that circulates mostly in the zymogen form, although a little less than 1% circulates as FVIIa (3). Both FVII and FVIIa bind to TF with similar affinities (4). Once bound to TF, FVII is rapidly converted to FVIIa via cleavage of a single peptide bond. The resulting TF:FVIIa complex is a two-subunit enzyme, in which FVIIa is the catalytic subunit and TF is the essential regulatory subunit. TF:FVIIa triggers the clotting cascade via limited proteolysis of factor IX (FIX) and factor X (FX).

X-ray crystal structures of a truncated, soluble form of tissue factor (sTF; composed of just the extracellular domain) have been determined (*5-9*) as well as complexes of sTF with FVIIa (*10, 11*). Previous mutagenesis studies have identified the residues of sTF that interact with FVIIa (*12*) and the complex structures reveal a large surface area of interaction between sTF and all 4 domains of FVIIa (*10, 11*). Though, it is well understood that these interactions induce conformational changes in the FVIIa active site; precisely how TF dramatically enhances the

enzymatic activity of FVIIa is not completely understood (*13*). Membrane-anchoring of TF is, however, absolutely required for full procoagulant activity (*14*).

TF contains two fibronectin type III domains. The C-terminal fibronectin type III domain of sTF contains key residues, including K165 and K166, that are necessary for the binding of TF:FVIIa substrates (*15, 16*). This region of sTF is adjacent to the γ-carboxyglutamic acid (GLA) domain of FVIIa in the TF:FVIIA complex and together form a proposed binding site (exosite) for substrates, FX and FIX (*15-17*). The exosite interacts with the GLA domain of various substrates and is in close contact with the membrane surface. Though the structure of this exosite is paramount to substrate binding; current sTF:FVIIa crystal structures differ on the conformation of the exosite (*10, 11*). Additionally, the crystal structures are missing several residues in TF (K159-K165; 2A2Q and K159-S163; 1DAN) between 159 and 184, the putative exosite (*16, 18*). Membrane interactions with TF, which are missing in the sTF crystal structures, are likely to play a key role in determining which conformation the exosite adopts in the TF:FVIIa complex.

Solid-state NMR (SSNMR) is a potent technique used to investigate conformational and dynamic changes of proteins at atomic resolution. Protein ^{13}C and ^{15}N chemical shifts are highly dependent on secondary structure (*19*), as well as on the electrostatic environment, crystal contacts and solvent exposure. Here we present chemical shift assignments for nanocrystalline sTF by SSNMR. We compare these assignments with previously reported solution NMR backbone chemical shifts for sTF (manuscript in prep, see chapter 7). Included in the chemical shift assignments are key residues that are near the membrane surface in membrane bound TF (membTF) and involved in the putative exosite of the TF:FVIIa complex ,as well as residues that interact with FVIIa. Additionally, we show initial SSNMR spectra of membTF embedded in

Nanodiscs (*20*), a membrane mimetic. Comparing the unbound sTF with membTF spectra and using chemical shift perturbation we report a preliminary conformational change of a loop (residues 159-165) in the extracellular domain of TF upon membrane insertion. These residues are contained in the proposed TF:FVIIa exosite (residues 159-184) (*10, 11*) whose conformation and interaction with the membrane surface is key to understanding the binding of substrate to the TF:FVIIA complex. These studies give key insights into the structure and membrane interactions of membTF and are the starting point for understanding the allosteric activation and substrate binding of the TF:FVIIA complex.

8.4 Experimental Procedures

8.4.1 Recombinant Protein Expression.

For uniformly labeled ^{13}C, ^{15}N-sTF and ^{13}C, ^{15}N-membTF proteins, cultures were grown in BioExpress (a isotopically labeled algal hydrolysate; Cambridge Isotopes Labs), ^{13}C-glycerol and phosphate. Specifically, 10X ^{13}C, ^{15}N-BioExpress is diluted to 1X concentration with 100 mM phosphate buffer at pH 7.5. ^{13}C-glycerol is added to achieve a 0.2% mass ratio (i.e. 2 grams of ^{13}C-glycerol in 1 liter). A starter culture was grown at 37 °C to OD600 = 6 in a modified Studier medium (*21*) (MDG) with natural abundance isotopes. MDG media contains 25 mM Na_2HPO_4, 25 mM KH_2PO_4, 5 mM Na_2SO_4, 2 mM $MgSO_4$, 0.2% NH_4Cl, 0.4% glucose (pH ~7) and supplemented with trace metals. The cells were then harvested and transferred to 3 volumes of fresh BioExpress media containing isotopes, and the culture was grown at 25° C until the OD reached ~3. Expression of sTF was induced with 20 μM IPTG for 24 hours. Expression of membTF was induced with 0.1 mM IPTG for 4 hours.

For proteins grown with either 1,3-^{13}C-glycerol or 2-^{13}C-glycerol, cultures were grown using the MDG media that contained 25 mM Na_2HPO_4, 25 mM KH_2PO_4, 5 mM Na_2SO_4, 2 mM

$MgSO_4$, 0.2% ^{15}N-NH_4Cl, 0.4% 1,3-^{13}C-glycerol (or 2-^{13}C-glycerol), pH ~7, supplemented with trace metals. Starter growths, expression and purification protocols are the same as for uniform labeled sTF. This protocol results in a yield of 20-30 mg sTF per liter.

8.4.2 Soluble Tissue Factor purification.

The cells were harvested, sTF released by osmotic shock, and the cell debris pelleted. The supernatant was treated with Q-Sepharose to remove a large fraction of the contaminating protein, and was then applied to a Ni affinity column. Fractions containing sTF were concentrated and the solution was then subjected to high-resolution gel filtration chromatography (HiPrep 16/160 Sephacryl S-200, GE Biosciences). This protocol results in a >95% purity, and a yield of 70-100 mg sTF per liter.

8.4.3 Membrane Tissue Factor purification.

The cells were harvested and suspended in a lysis buffer that contained 2.5% (w/v) octylglucoside in 50 mM phosphate buffer, pH 7.4, 50 mM NaCl and 0.1% NaN3. Benzonase (Novagen) is added to remove DNA and RNA. The cells debris was pelleted and the supernatant was treated with Q-Sepharose to remove a large fraction of the contaminating protein. The membTF protein contains a HPC4 epitope tag and after the Q-Sepharose the solution was applied to a HPC4 affinity column. Fractions containing sTF were concentrated and incorporated into Nanodiscs following previously published procedures (*22*).

8.4.4 SSNMR Spectroscopy.

Nanocrystalline sTF was prepared for SSNMR experiments by addition of 15% PEG 3350 to a 1 mM sTF sample in phosphate buffer (pH 7.5) and allowed to crystallize at 20 °C overnight. To confirm sample integrity, nanocrystalline sTF was dissolved in a phosphate buffer (pH 7.5) and the clotting activity measured. The re-dissolved sTF Nanocrystals retained >95% of its

activity, confirming that crystallization does not adversely affect the sample. Nanocrystals samples of sTF were grown with 1, 3-^{13}C glycerol, 2-^{13}C glycerol and with uniform ^{13}C labeling and were packed into 3.2-mm rotors with ~6-9 mg protein in standard wall rotors and ~10-15 mg in thin wall rotors. All samples contained uniform ^{15}N labeling. Nanodiscs containing ^{13}C, ^{15}N-membTF were lyophilized and rehydrated in the rotor at a 2:1 sample mass:water ratio. Protein assays and NMR experiments (calibrated to ^{13}C standards) indicate that 1.5±0.5 mg of membTF protein was packed into the 3.2 mm standard rotor. Experiments were performed on a 14.0 Tesla (600 MHz ^{1}H frequency) Varian Infinity Plus spectrometer and a 17.6 Tesla (750 MHz ^{1}H frequency) Varian Unity Inova spectrometer equipped with Varian Balun™ ^{1}H-^{13}C-^{15}N 3.2-mm probes. All data was acquired at 10±3 °C actual sample temperature (determined by ethylene glycol calibration) (*23*). All experiments utilized tangent ramped cross polarization (*24*) with TPPM (*25*) decoupling of the protons applied during acquisition and evolution periods at ~80 kHz. For 3D ^{15}N-^{13}C-^{13}C and ^{13}C-^{15}N-^{13}C correlation experiments, band-selective SPECIFIC CP (*26*) was used for polarization transfer between ^{15}N and ^{13}C. Other experiments were performed according to published procedures as cited in the main text. Hard π/2 pulse widths were typically 3.0 μs for ^{1}H and ^{13}C, and 4.5 ms for ^{15}N. Backbone and side chain assignments were based on several spectra; two-dimensional (2D) ^{13}C-^{13}C spectrum, 2D NCA and NCO spectra, and three-dimensional (3D) NCACX, NCOCX and CANCO spectra.

Spectra were processed with NMRPipe (*27*) employing zero filling and Lorentzian-to-Gaussian line broadening for each dimension before Fourier transformation. Back linear prediction and polynomial baseline correction were applied to the frequency domain in the direct dimension. Chemical shifts were referenced externally with adamantane (assuming the

downfield peak to resonate at 40.48 ppm) (*28*). Additional experimental details are listed in the figure captions. Peak picking and assignments were performed with Sparky (*29*).

8.5 Results and Discussion

8.5.1 Solid-State NMR Assignments of soluble Tissue Factor.

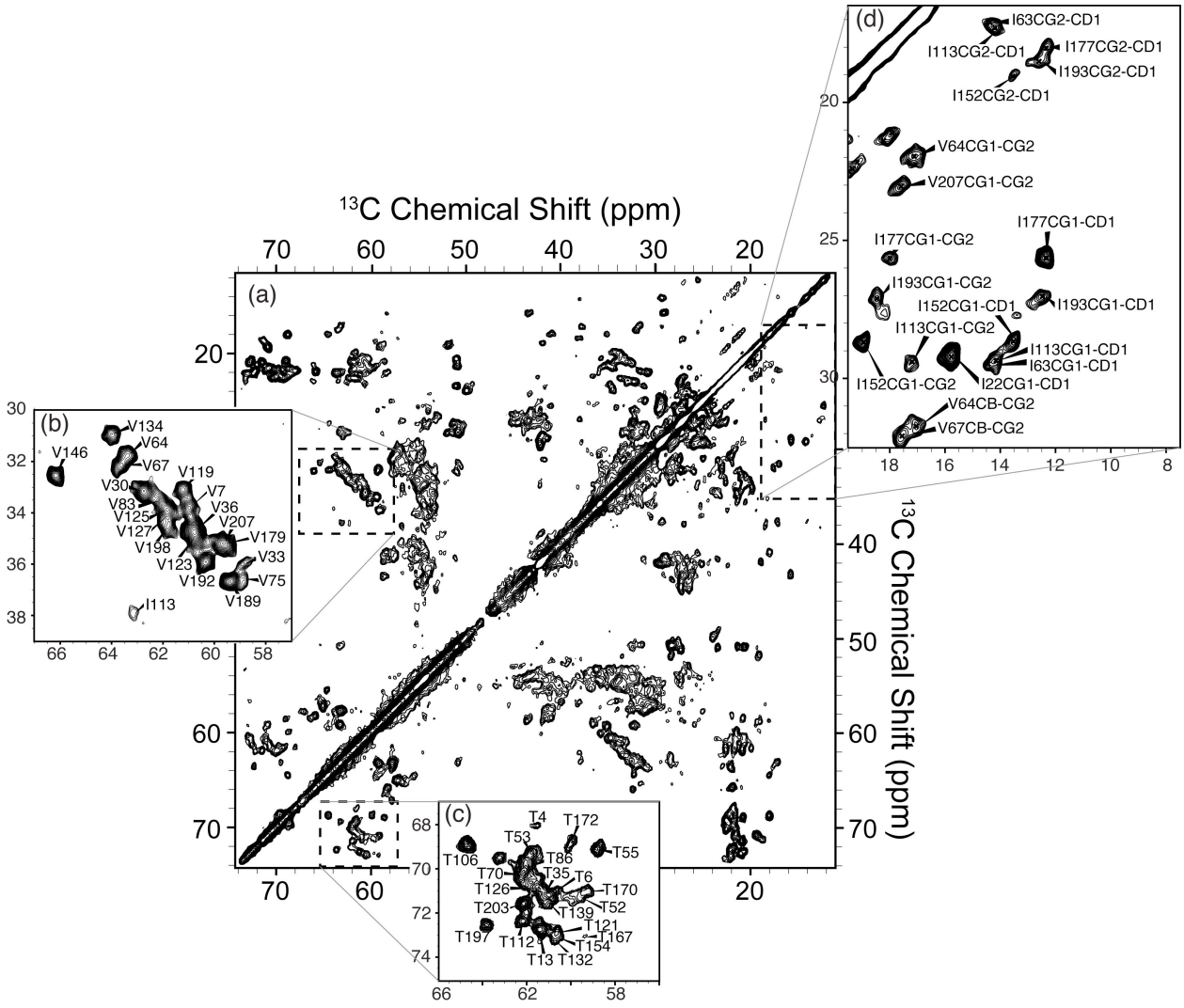

Figure 8.1 ^{13}C-^{13}C 2D spectra of nanocrystalline sTF.

(a) 13C-13C 2D spectrum of PEG-precipitated U-13C, ^{15}N-sTF (12 hrs, 750 MHz, 25 ms DARR mixing). Expansions of the (b) valine Cα-Cβ region, (c) threonine Cα-Cβ region, and (d) isoleucine Cγ-Cδ region are shown with assignments.

SSNMR assignments were carried out using a recently published strategy (*30*) and involved several 2D and 3D data sets collected on three nanocrystalline samples; a uniform ^{13}C, ^{15}N-sTF;

a 1,3-^{13}C glycerol, ^{15}N-sTF; and a 2-^{13}C glycerol, ^{15}N-sTF (see experimental section). The nanocrystalline sTF preparation produces highly resolved spectra with ^{13}C line widths of ~0.3 to 0.5 ppm. Initial SSNMR investigation of sTF began with a ^{13}C-^{13}C 2D DARR (*31, 32*) spectrum (Figure 8.1). This spectrum is similar to the HSQC "fingerprint" spectra in solution NMR and gives insight into the secondary structure of the protein. In the ^{13}C-^{13}C 2D spectrum (Figure 8.1) we are able to assign amino acid types to valine, threonine, serine, isoleucine, and alanine spin systems. Integrated intensities and peak counts of the resolved spin systems are consistent with properly folded sTF as compared to crystal structures (*5-9*). Backbone N, Cα, CO as well as Cβ side-chain assignments were previously published (BMRB XXXX) for sTF (manuscript in prep; see chapter 7) and were used to assist assignment of SSNMR data. However, all ^{13}C, ^{15}N assignments made in SSNMR spectra were confirmed through intermolecular correlations using 2D and 3D spectra. Using these strategies allowed for ~80% of the sTF residues to be assigned in the SSNMR data. Correlation assignments for the valine and threonine Cα-Cβ's and isoleucine Cγ-Cδ's are labeled in Figure 8.1, demonstrating the completeness of assignments. The full extent of the SSNMR assignments are mapped onto the crystal structure (pdb: 2HFT) (*9*) in Figure 8.2. Residues lacking assignments (black) are predominantly found in the first fibronectin type III domain at the end of β-sheets (i.e. 76-78) and in unstructured loops and turns (i.e. 82-85, 88-91). Secondary structural prediction using TALOS (*33*) were performed and are consistent with the X-ray crystal structures (*5-9*).

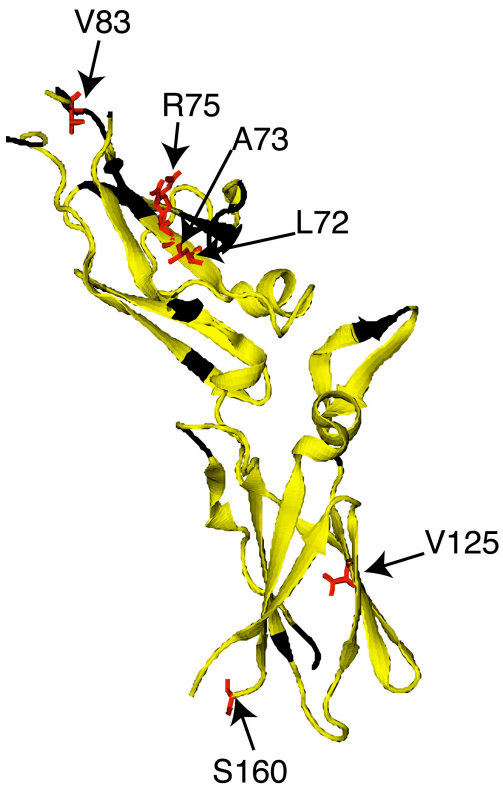

Figure 8.2 Structure of sTF.

X-ray crystal structure of sTF (pdb: 2HFT; (*9*)) color-coded according to assignment completion. Residues assigned in the SSNMR spectra are colored yellow; residues lacking assignments are in black. Residues that differ in chemical shifts significantly (>1.0 ppm) between solution and solids data are rendered in red with the side-chains drawn and labeled.

8.5.2 Comparing solution and SSNMR data.

Previous studies have shown little variation (<0.5 ppm in ^{13}C) in solution state and solid-state NMR chemical shifts of proteins (*30, 34-39*). Perturbations are usually attributable to sample preparation, crystal packing interactions or the solvent accessibility of the residue. In both the solution and nanocrystlline sTF samples the chemical shifts were consistent with properly folded sTF, though; there were slight differences in the sample preps. The solution sample was prepared in a 50 mM phosphate buffer, pH 6.5 with 50 mM NaCl (manuscript in prep; see chapter 7). The SSNMR nanocrystalline sample contained 25 mM phosphate buffer, pH 7.5 and precipitated with PEG with no additional salt added (see experimental section). To investigate the variation

between solution and SSNMR assignments we plotted the SSNMR assignments verses the solution NMR assignments for the Cα, Cβ, N and CO atoms (Figure 8.3). Regression analysis of the plots resulted in R^2 values between 0.956-0.999, indicating an overall agreement between the solution and SSNMR data. There is very little change in the Cα and Cβ assignments (Figure 8.3a, b) whose chemical shifts are highly sensitive to changes in secondary structure, indicating no measurable change in conformation between the two samples. The N and the CO are more dependent on hydrogen bonding and electrostatic effects and showed slightly more variation, with a few residues whose chemical shifts differed by more than 1.0 ppm (Figure 8.3c, d). These residues are highlighted on the sTF crystal structure (Figure 8.2) and are most likely due to electrostatic and crystal packing interactions.

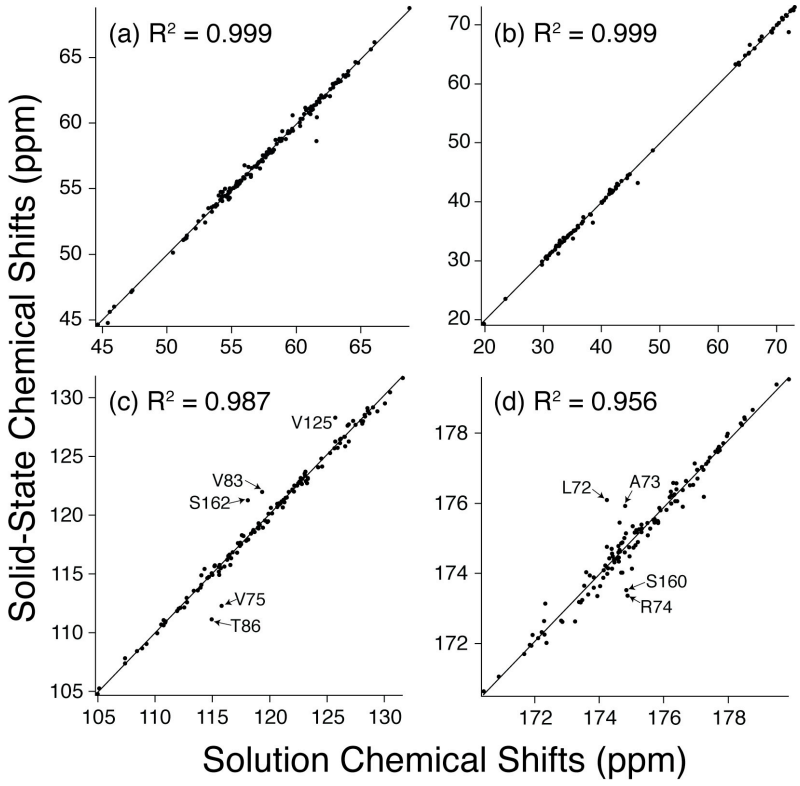

Figure 8.3 Solid-state versus solution state chemical shift assignments of sTF.

(a) Cα, (b) Cβ, (c) N, and (d) CO solid-state versus solution state chemical shift assignments of sTF. Labeled residues are for those that differ by greater than 1.0 ppm.

8.5.3 Membrane TF in bilayers.

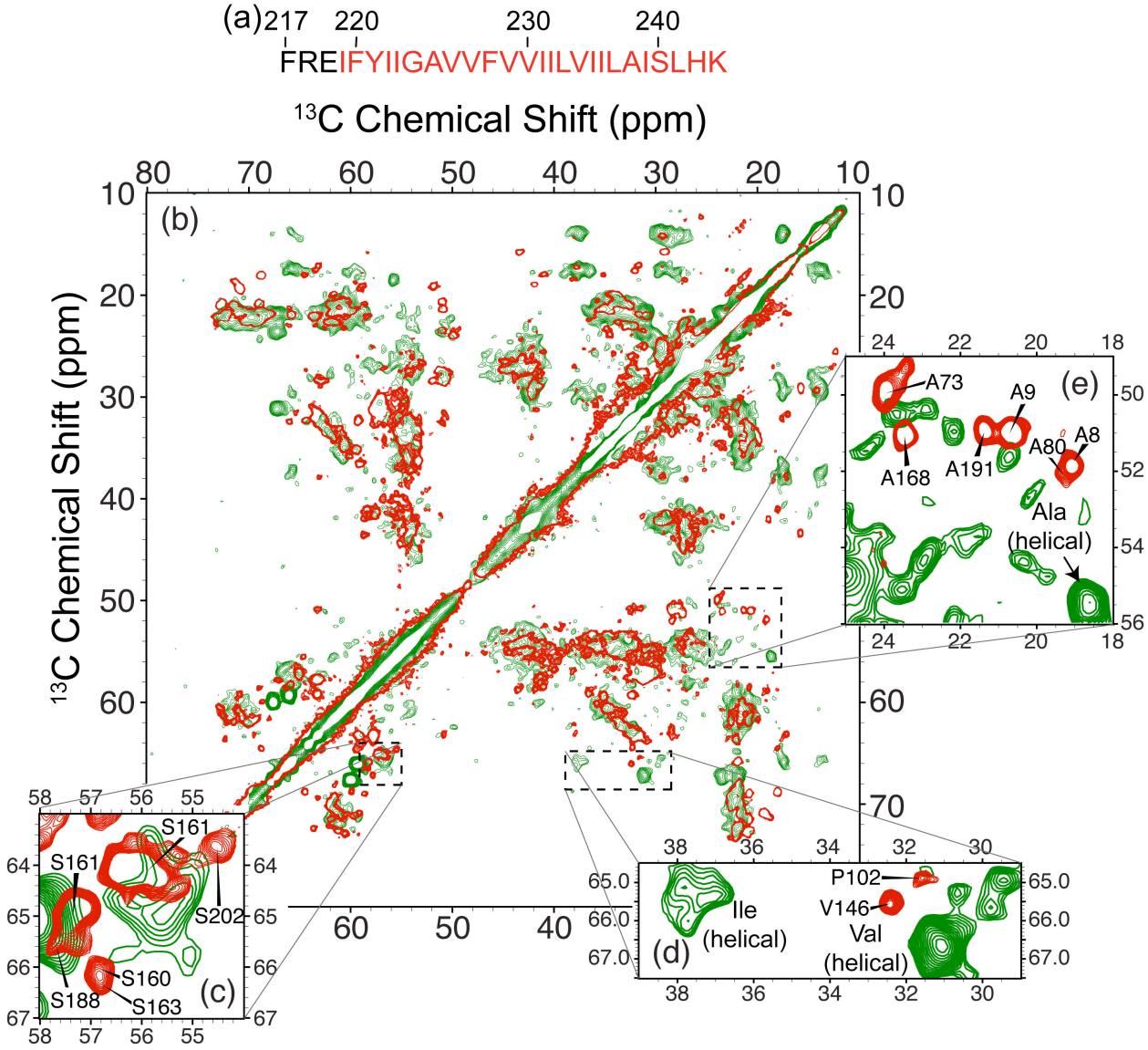

Figure 8.4 ^{13}C-^{13}C 2D spectrum of Nanodisc-embedded U-^{13}C,^{15}N-membTF.

(a) Residues 217 to 243 of membTF are shown with the residues in the transmembrane helix in red. (b) 13C-13C 2D spectrum U-13C, ^{15}N-membrane bound TF (green; 36 hrs, 600 MHz, 50 ms DARR mixing) overlaid with 13C-13C 2D spectrum of PEG-precipitated U-13C, ^{15}N-sTF (red). Expansions of the (c) serine Cα-Cβ region, (d) helical valine and isoleucine Cα-Cβ region, and (e) alanine Cα-Cβ region with assignments for the some sTF resonances shown. * Note: the intense peaks at 60.18, 67.91 ppm and 59.55, 66.26 ppm are from the Cα-Cβ correlations from isotopically labeled ^{13}C, ^{15}N-phosphatidylserine headgroups.

To investigate conformation changes in the extracellular domain of TF due to interactions with the membrane we prepared a U-^{13}C, ^{15}N membTF sample that contained the transmembrane helix (residues 219-243) (Figure 8.4a) and embedded it into Nanodiscs, a membrane mimetic, to study by SSNMR. Traditional methods used to investigate atomic resolution structural information, such as solution NMR and X-ray crystallography, have had limited success with large membrane bound proteins. SSNMR has a unique advantage over these traditional techniques in that it does not require single crystals and has no size limitations as found for X-ray crystallography and solution NMR, respectively. An initial ^{13}C-^{13}C 2D spectrum was acquired for the membTF sample (Figure 8.4). The overall resolution of the spectrum is comparable to the nanocrystalline sTF ^{13}C-^{13}C 2D spectra (Figure 8.1) and a large number of resolved resonances are visible. Further comparison with the ^{13}C-^{13}C 2D spectrum of sTF shows that many of the chemical shift patterns—especially among the beta-sheet conformation signals—are unchanged or only slightly changed in the membTF relative to sTF. This is expected since most of the protein does not directly interact with the membrane surface. Several new resonances are observed in the spectrum which can be attributed to residues 219-243 of the transmembrane helix (Figure9.4d, e). This portion of the sequence (Figure 8.4a) includes several new Ile and Val residues, as well as two Ala residues. All of these signals appear in the 2D spectrum at positions indicating helical secondary structure (Figure 8.4d, e), which are not observed in the sTF spectrum.

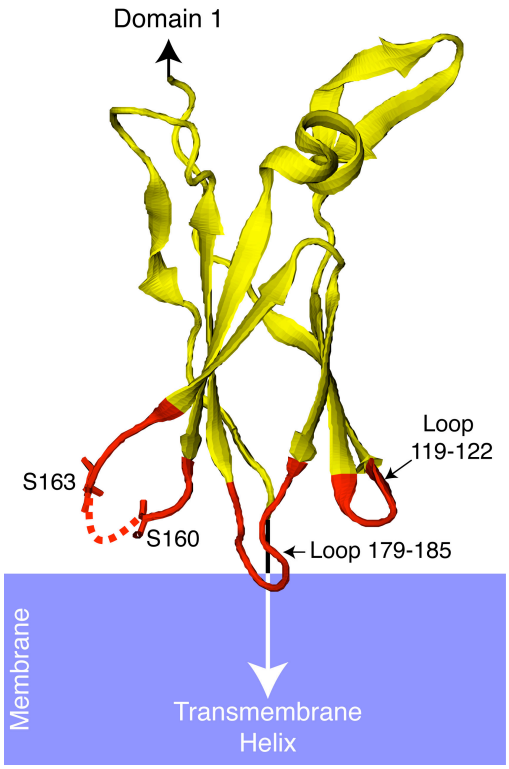

Figure 8.5 Membrane interactions with the 2nd fibronectin type III domain of sTF.

C-terminal fibronectin type III domain of sTF is shown (pdb: 2HFT (*9*)) with loops (residues 159-165, 179-185, 119-122) likely to interact with the membrane surface in red. S161 and S162 are missing from the crystal structure and are indicated with a dotted line. The blue box represents the membrane surface.

Interactions of the extracellular domain of membTF with the membrane surface and the formation of TF dimers in the membrane will likely cause conformational changes that are observable as changes in sTF backbone chemical shift values. Formation of TF dimers in the membrane is the consequence of an interaction between neighboring transmembrane helices (*40*). The formation of TF dimers and membrane interactions with the extracellular domain of TF likely play a key role in activation of the TF:FVIIa complex (*41*) and are lacking information in current X-ray structures (*5-9*). Figure 8.5 shows the C-terminal fibronectin type III domain of sTF and indicates three loops that are likely to interact with the membrane surface. One loop contains S160, S161, S162 and S163 whose Cα-Cβ chemical shift values show large

perturbations (Figure 8.4c) in the membTF sample consistent with a change in conformation due to interaction with the membrane surface. Changes in the alanine Cα-Cβ chemical shifts (Figure 8.4e) could be due to a combination of the membrane interactions and the formation of TF dimers. The alanine resonance count in the Cα-Cβ region is consistent with expectations for both the membTF and sTF sample but display different chemical shifts indicating changes in the conformation of these residues. Alanine 168 and 191 are in the C-terminal fibronectin type III domain, with A168 in the β-sheet following loop 159-165. Interactions with the membrane surface could cause small perturbations in conformation of these residues. The rest of the alanine residues (2, 8, 9, 73, 80 and 89) are in the first fibronectin type III domain of sTF and changes due to direct interaction with the membrane are unlikely. Changes in these resonances are reasonably attributed to interactions due to the dimerization of TF in the membrane. More data is required and currently being performed to complete a full atomic resolution structure of membrane bound TF.

8.5.4 Conclusion.

We have presented ^{13}C and ^{15}N SSNMR chemical shift assignments for nanocrystalline sTF. Comparison of these chemical shifts shows an overall agreement to previously determined solution NMR assignments (manuscript in preparation, see chapter 7). A few residues contain major differences (>1 ppm) in the N and CO chemical shifts between the solution and SSNMR, which we attribute to slight changes in the electrostatics of the sample preps and possible crystal contacts. The chemical shift assignments include residues important in key interactions with FVIIa, the membrane surface and TF:FVIIa substrates. These include residues in a dynamic loop (72-92) that are key in allosteric activation of FVIIa (*42, 43*), residues 159 to 184 involved in the reputed substrate binding site (*16, 18*) and several residues likely to be involved in TF-membrane

interactions (Figure 8.5). Conformational changes and interactions of these residues can be analyzed by investigating perturbations to the chemical shifts upon formation of the various complexes (i.e. membrane bound TF, TF:FVIIa and TF:FVIIa:FX). SSNMR is uniquely capable to carry out these investigations since the complexes are too large for analysis by solution NMR and X-ray crystallography requires single crystals.

A ^{13}C-^{13}C 2D spectrum of membTF was compared with sTF spectra. This analysis has given insights into membrane interactions with the extracellular domain of TF and the formation of TF dimers. Initial comparisons of the membTF and sTF ^{13}C-^{13}C 2D spectra revealed the expected resonances arising from the helical valine, isoleucine and alanine residues present in the transmembrane helix. Using chemical shift perturbation we report, for the first time, a loop in the extracellular domain of TF involved in membrane interactions in membTF. Loop 159-165 is contained in the C-terminal fibronectin type III domain of sTF and is near the membrane surface in membTF. Perturbation to the chemical shifts for S160 to S163 in the membTF ^{13}C-^{13}C 2D is strong evidence that loop 159-165 is interacting with the membrane surface. Interactions of both the C-terminal fibronectin type III domain with the membrane surface and formation of TF dimers in membranes are likely responsible for changes in the alanine chemical shifts reported for membTF. Changes for two alanines in the C-terminal fibronectin type III domain (A168, A191) could be due to membrane interactions. The other six alanines are all in the first fibronectin type III domain of sTF and changes in the chemical shift are more likely due to interactions involved in TF dimerization. Further studies are underway to determine all residues involved in membrane interactions and ultimately, to determine an atomic resolution membTF structure.

8.6 Acknowledgements

The authors would like to thank Dr. Steven Sligar and Dr. Aleksandra Kijac for assistance with the Nanodisc system; Drs. Emad Tajkhorshid and Y. Zenmei Ohkubo for many useful discussions; Lindsay J. Sperling and Andrew J. Nieuwkoop for assisting in acquisition of experiments.

8.7 References

1. Morrissey, J. H. (2004) Tissue factor: A key molecule in hemostatic and nonhemostatic systems. *Int J Hematol 79*, 103-108.
2. Drake, T. A., Morrissey, J. H., and Edgington, T. S. (1989) Selective Cellular Expression of Tissue Factor in Human-Tissues - Implications for Disorders of Hemostasis and Thrombosis. *Am J Pathol 134*, 1087-1097.
3. Morrissey, J. H., Macik, B. G., Neuenschwander, P. F., and Comp, P. C. (1993) Quantitation of Activated Factor-VII Levels in Plasma Using a Tissue Factor Mutant Selectively Deficient in Promoting Factor-VII Activation. *Blood 81*, 734-744.
4. Morrissey, J. H., and Mutch, N. J. (2006) Hemostasis and Thrombosis: Basic Principles and Clinical Practice, in *Hemostasis and Thrombosis: Basic Principles and Clinical Practice* (Colman, R. W., Marder, V. J., Clowes, A. W., George, J. N., and Goldhaber, S. Z., Eds.) pp 91-106, Lippincott Williams and Wilkins, Philadelphia.
5. Harlos, K., Martin, D. M. A., Obrien, D. P., Jones, E. Y., Stuart, D. I., Polikarpov, I., Miller, A., Tuddenham, E. G. D., and Boys, C. W. G. (1994) Crystal-structure of the extracellular region of human tissue factor (Vol 370, Pg 662, 1994). *Nature 371*, 720-720.

6. Muller, Y. A., Ultsch, M. H., Kelley, R. F., and Devos, A. M. (1994) Structure of the Extracellular Domain of Human Tissue Factor - Location of the Factor Viia Binding-Site. *Biochemistry 33*, 10864-10870.

7. Huang, M. D., Syed, R., Stura, E. A., Stone, M. J., Stefanko, R. S., Ruf, W., Edgington, T. S., and Wilson, I. A. (1998) The mechanism of an inhibitory antibody on TF-initiated blood coagulation revealed by the crystal structures of human tissue factor, Fab5G9 and TF center dot 5G9 complex. *J. Mol. Biol. 275*, 873-894.

8. Muller, Y. A., Kelley, R. F., and De Vos, A. M. (1998) Hinge bending within the cytokine receptor superfamily revealed by the 2.4 angstrom crystal structure of the extracellular domain of rabbit tissue factor. *Protein Sci. 7*, 1106-1115.

9. Muller, Y. A., Ultsch, M. H., and deVos, A. M. (1996) The crystal structure of the extracellular domain of human tissue factor refined to 1.7 angstrom resolution. *J. Mol. Biol. 256*, 144-159.

10. Banner, D. W., DArcy, A., Chene, C., Winkler, F. K., Guha, A., Konigsberg, W. H., Nemerson, Y., and Kirchhofer, D. (1996) The crystal structure of the complex of blood coagulation factor VIIa with soluble tissue factor. *Nature 380*, 41-46.

11. Bajaj, S. P., Schmidt, A. E., Agah, S., Bajaj, M. S., and Padmanabhan, K. (2006) High resolution structures of p-aminobenzamidine- and benzamidine-VIIa soluble tissue factor - Unpredicted conformation of the 192-193 peptide bond and mapping of Ca^{2+}, Mg^{2+}, Na^{+}, and Zn^{2+} sites in factor VIIa. *J. Biol. Chem. 281*, 24873-24888.

12. Ruf, W., Schullek, J. R., Stone, M. J., and Edgington, T. S. (1994) Mutational Mapping of Functional Residues in Tissue Factor - Identification of Factor-Vii Recognition

Determinants in Both Structural Modules of the Predicted Cytokine Receptor Homology Domain. *Biochemistry 33*, 1565-1572.

13. Eigenbrot, C., and Kirchhofer, D. (2002) New insight into how tissue factor allosterically regulates Factor VIIa. *Trends Cardiovas Med 12*, 19-26.

14. Paborsky, L. R., Caras, I. W., Fisher, K. L., and Gorman, C. M. (1991) Lipid Association, but Not the Transmembrane Domain, Is Required for Tissue Factor Activity - Substitution of the Transmembrane Domain with a Phosphatidylinositol Anchor. *J. Biol. Chem. 266*, 21911-21916.

15. Huang, Q. L., Neuenschwander, P. F., Rezaie, A. R., and Morrissey, J. H. (1996) Substrate recognition by tissue factor-factor VIIa - Evidence for interaction of residues Lys(165) and Lys(166) of tissue factor with the 4-carboxyglutamate-rich domain of factor X. *J. Biol. Chem. 271*, 21752-21757.

16. Kirchhofer, D., Lipari, M. T., Moran, P., Eigenbrot, C., and Kelley, R. F. (2000) The tissue factor region that interacts with substrates factor IX and factor X. *Biochemistry 39*, 7380-7387.

17. Ruf, W., Shobe, J., Rao, S. M., Dickinson, C. D., Olson, A., and Edgington, T. S. (1999) Importance of factor VIIa Gla-domain residue Arg-36 for recognition of the macromolecular substrate factor X Gla-domain. *Biochemistry 38*, 1957-1966.

18. Kirchhofer, D., Eigenbrot, C., Lipari, M. T., Moran, P., Peek, M., and Kelley, R. F. (2001) The tissue factor region that interacts with factor Xa in the activation of factor VII. *Biochemistry 40*, 675-682.

19. Wishart, D. S., Bigam, C. G., Yao, J., Abildgaard, F., Dyson, H. J., Oldfield, E., Markley, J. L., and Sykes, B. D. (1995) H-1, C-13 and N-15 Chemical-Shift Referencing in Biomolecular NMR. *J. Biomol. NMR 6*, 135-140.

20. Bayburt, T. H., Grinkova, Y. V., and Sligar, S. G. (2002) Self-assembly of discoidal phospholipid bilayer nanoparticles with membrane scaffold proteins. *Nano Lett. 2*, 853-856.

21. Studier, F. W. (2005) Protein production by auto-induction in high density shaking cultures. *Protein Expr Purif 41*, 207-34.

22. Shaw, A. W., Pureza, V. S., Sligar, S. G., and Morrissey, J. H. (2007) The local phospholipid environment modulates the activation of blood clotting. *J. Biol. Chem. 282*, 6556-6563.

23. Van Geet, A. L. (1968) *Anal. Chem. 42*, 2227.

24. Hediger, S., Meier, B. H., Kurur, N. D., Bodenhausen, G., and Ernst, R. R. (1994) NMR cross-polarization by adiabatic passage through the Hartmann-Hahn condition (APHH). *Chem. Phys. Lett. 223*, 283-288.

25. Bennett, A. E., Rienstra, C. M., Auger, M., Lakshmi, K. V., and Griffin, R. G. (1995) Heteronuclear decoupling in rotating solids. *J. Chem. Phys. 103*, 6951-6958.

26. Baldus, M., Petkova, A. T., Herzfeld, J. H., and Griffin, R. G. (1998) Cross polarization in the tilted frame: assignment and spectral simplification in heteronuclear spin systems. *Mol. Phys. 95*, 1197-1207.

27. Delaglio, F., Grzesiek, S., Vuister, G. W., Zhu, G., Pfeifer, J., and Bax, A. (1995) NMRpipe: a Multidimensional Spectral Processing System Based On Unix Pipes. *J. Biomol. NMR 6*, 277-293.

28. Morcombe, C. R., and Zilm, K. W. (2003) Chemical shift referencing in MAS solid state NMR. *J. Magn. Reson. 162*, 479-486.

29. Goddard, T. D., and Kneller, D. G., University of California, San Francisco.

30. Sperling, L. J., Berthold, D. A., Sasser, T. L., Jeisy-Scott, V., and Rienstra, C. M. (2010) Assignment for large proteins by magic-angle spinning NMR: the 21-kDa disulfide bond forming enzyme DsbA. *J. Biol. Chem. in press*.

31. Morcombe, C. R., Gaponenko, V., Byrd, R. A., and Zilm, K. W. (2004) Diluting abundant spins by isotope edited radio frequency field assisted diffusion. *J. Am. Chem. Soc. 126*, 7196-7197.

32. Takegoshi, K., Nakamura, S., and Terao, T. (2001) ^{13}C-^{1}H dipolar-assisted rotational resonance in magic-angle spinning NMR. *Chem. Phys. Lett. 344*, 631-637.

33. Cornilescu, G., Delaglio, F., and Bax, A. (1999) Protein backbone angle restraints from searching a database for chemical shift and sequence homology. *J. Biomol. NMR 13*, 289-302.

34. Franks, W. T., Zhou, D. H., Wylie, B. J., Money, B. G., Graesser, D. T., Frericks, H. L., Sahota, G., and Rienstra, C. M. (2005) Magic-angle spinning solid-state NMR spectroscopy of the beta-1 immunoglobulin binding domain of protein G (GB1): ^{15}N and ^{13}C chemical shift assignments and conformational analysis. *J. Am. Chem. Soc. 127*, 12291-12305.

35. Igumenova, T. I., McDermott, A. E., Zilm, K. W., Martin, R. W., Paulson, E. K., and Wand, A. J. (2004) Assignments of carbon NMR resonances for microcrystalline ubiquitin. *J. Am. Chem. Soc. 126*, 6720-6727.

36. Wylie, B. J., Franks, W. T., and Rienstra, C. M. (2006) Determinations of ^{15}N chemical shift anisotropy magnitudes in a uniformly ^{15}N,^{13}C-labeled microcrystalline protein by three-dimensional magic-angle spinning nuclear magnetic resonance spectroscopy. *J. Phys. Chem. A 110*, 10926-10936.

37. Wylie, B. J., Sperling, L. J., Frericks, H. L., Shah, G. J., Franks, W. T., and Rienstra, C. M. (2007) Chemical-shift anisotropy measurements of amide and carbonyl resonances in a microcrystalline protein with slow magic-angle spinning NMR spectroscopy. *J. Am. Chem. Soc. 129*, 5318.

38. Frericks Schmidt, H. L., Sperling, L. J., Gao, Y. G., Wylie, B. J., Boettcher, J. M., Wilson, S. R., and Rienstra, C. M. (2007) Crystal polymorphism of protein GB1 examined by solid-state NMR spectroscopy and x-ray diffraction. *J. Phys. Chem. B 111*, 14362-14369.

39. Wylie, B. J., Schwieters, C. D., Oldfield, E., and Rienstra, C. M. (2009) Protein Structure Refinement Using $^{13}C\alpha$ Chemical Shift Tensors. *J. Am. Chem. Soc. 131*, 985-992.

40. Bach, R. R., and Moldow, C. F. (1997) Mechanism of tissue factor activation on HL-60 cells. *Blood 89*, 3270-3276.

41. Bach, R. R. (2006) Tissue factor encryption. *Arterioscl Throm Vas 26*, 456-461.

42. Eigenbrot, C., Kirchhofer, D., Dennis, M. S., Santell, L., Lazarus, R. A., Stamos, J., and Ultsch, M. H. (2001) The factor VII zymogen structure reveals reregistration of beta strands during activation. *Structure 9*, 627-636.

43. Minazzo, A. S., Darlington, R. C., and Ross, J. B. A. (2009) Loop Dynamics of the Extracellular Domain of Human Tissue Factor and Activation of Factor VIIa. *Biophys. J. 96*, 681-692.